2017

Thermomechanical Modeling of Polymerica Actuators

Qianxi Yang
Louisiana State University and Agricultural and Mechanical College

THERMOMECHANICAL MODELING OF POLYMERIC ACTUATORS

A Dissertation

Submitted to the Graduate Faculty of the
Louisiana State University and
Agricultural and Mechanical College
in partial fulfillment of the
requirements for the degree of
Doctor of Philosophy

in

The Department of Mechanical and Industrial Engineering

by
Qianxi Yang
B.S., University of Science and Technology of China, 2010
May 2017

To my parents

my dear husband

and my friends

ACKNOWLEDGMENTS

First and foremost, I wish to express my most sincere gratitude and appreciation to my advisor, Dr. Guoqiang Li, for his guidance, patience and encouragement leading me through the whole journey. He always put forth challenges and shines me with brilliant ideas which kept me moving forward on my research pathway. Every time when I met obstacles, he is kind and patient enough so that I could focus on preparing myself without worrying about short term outcomes. He is the one that can always give me invaluable advices and encouragement when I was confused and helpless. As an advisor for my research and a mentor for my life, his dedication and integrity have set up a standard for me to pursue every single goal in my future.

I would also like to extend my appreciation to my committee members, Dr. Dorel Moldovan, Dr. Ying Wang and Dr. Steve Cai for the valuable advices on my research and my career path.

I feel fortunate to have Dr. Pengfei Zhang, Dr. Lu Lu, Jizhou Fan and Siavash Sarrafan as my research colleagues and my friends. I have learned a lot from them and I have had an enjoyable time working with them.

I save my final thanks for my beloved families. My parents, Dr. Jianbo Yang and Yayun Ji watched me from a distance while I worked towards my degree. The completion of this thesis will mean a lot to them. My husband, Dr. Chen Chen who always supports me unconditionally and shares the joys and sorrows with me, is the reason that I do anything for. So I dedicate this project to my loving families, without whose love, affection and encouragement this work would not have been possible.

TABLE OF CONTENTS

LIST OF TABLES

LIST OF FIGURES

ABSTRACT

In this dissertation, the application of smart polymers as actuators was investigated, with focuses on shape memory polymers and twisted-then-coiled artificial muscles. Thermomechanical models have been developed for various polymeric actuators, so as to facilitate interpretation of the underlying mechanisms and to provide guidance for future design.

The classical one-way shape memory effect in amorphous shape memory polymers was first reproduced. The amorphous shape memory polymer was treated as a frozen-phase matrix with active-phase inclusions embedded in it. A phase evolution law was proposed from the physics perspective and the Mori-Tanaka approach was used to predict the effective mechanical properties. Then, a phenomenological constitutive model was developed based on the multiple natural configurations framework for the semi-crystalline two-way shape memory effect. The model elucidated how the programming procedure affect the crystallization behavior and eventually determine the two-way shape memory effect via storage of internal stress.

Artificial muscles with hierarchical chiral structure that can offer a hundredfold increase in power over natural muscles of equivalent lengths have recently been demonstrated experimentally. To investigate the physical origin behind the remarkable tensile actuation behavior and, therefore, the correlation between the actuation performance and the intrinsic material parameters, a multi-scale modeling framework from macro-scale helical spring structure top-down to the molecular chain interaction has been developed Then, based on the prediction results of the multi-scale model, a new type of hierarchical chiral structured artificial muscle was fabricated using two-way shape memory polymer fiber. The usual improvement in the axial actuation of the twisted-then-coiled muscles were demonstrated both experimentally and theoretically.

CHAPTER 1 INTRODUCTION

This dissertation consists of six chapters. The chapters from the second to the fifth are based on papers that have been published, or are under review. In this introduction chapter, a literature review on the research topic has been conducted. This is followed by the motivation and objectives of the studies that have been carried out. Finally, the dissertation structure has been outlined. The work in each chapter is solely independent, but proceeding in an orderly way and step by step with the aim of achieving final objective of this study. All chapters, except this introductory one, document the research results of the Ph.D. candidate under the direction of the candidate's advisor as well as her committee members.

1.1 General Aspects of Polymeric Actuators

Actuators are materials and devices that are able to change their shape in response to changes in environmental conditions and thus perform mechanical work on the nano- micro-, and macro-scales [1-5]. Among the huge variety of different actuators, polymer-based ones are highly attractive because of a number of properties such as sensitivity to a broad range of stimuli and outstanding mechanical properties [2, 6-9]. The polymers can be soft (viscoelastic state) and hard (glassy state) depending on their chemical and physical structure that allows the design of soft actuators for handling soft living tissues and hard actuators for handling metals [10]. There are many polymers sensitive to different stimuli that allows the design of actuators that can be controlled by temperature, pH, bio signals, or light [11]. Many polymers are biocompatible and biodegradable, which allows the integration of polymeric actuators in living systems and their resorption there.

The polymeric actuators can be classified based on the actuation stimuli, working mechanisms or their applications. From the actuation stimuli point of view, the actuators can be driven by voltage, current, magnetic, temperature and light, etc. Based on the working mechanisms, the polymeric actuators can be artificially divided into several groups. The first group of actuators comprises those based on the elastic relaxation of shape after deformation, such as dielectric elastomeric actuators with elastomers between two electrodes [12] and amorphous shape memory polymers [13]. The second group of actuators are based on the reversible transitions between different states, such as transitions between different ordered states in liquid-crystalline actuators [14], melting transitions in semicrystalline polymers [15] and order-disorder ionic phase transition in ionomer [16]. The third group is actuators where the driving force is surface tension. Typically, such actuators are small because they are able to function when the surface tension is considerable. Surface-tension actuators are irreversible [17, 18]. From the application perspective, some of the applications such as artificial muscles, swimmers or walkers, and microsurgical devices are based mostly on the generation of force during actuation. Other applications such as sensors [19], switchable optical devices [20], and smart textiles [21], etc. are based on the change in shape during actuation.

In this study, we mainly focus on two types of polymeric actuators, shape memory polymers and polymeric artificial muscles.

1.1.1 Shape memory polymers (SMPs)

Shape memory polymer (SMP) is a class of polymeric actuators that can be deformed and fixed in a temporary shape at a certain condition and recovers the original shape when exposed to a suitable stimulus[13, 22-30], such as temperature[15, 31-34], light [35, 36], magnetic field[37, 38] or humidity [39, 40]. The term "shape-memory" was first proposed by Vernon in 1941 [41]. Although most polymers can exhibit some degrees of shape memory behavior, the importance of SMPs was not recognized until the 1960s, when cross-linked polyethylene (PE) were used as shrinkage tape to apply pressure [42]. SMPs have many advantages over shape memory alloys and ceramics, such as low manufacturing cost, easy processing and most significantly, high shape recovery strain (maximum recovery strain can be over 800% [30]). Based on these unique features, SMPs have emerged as one of the key functional materials in both academia and industry in recent years.

Generally, SMPs are elastic polymer networks that are equipped with stable netpoints and suitable stimuli-sensitive switching domains [31]. The netpoints determine the permanent shape of the polymer network and can be of a chemical (covalent bonds) or physical (intermolecular interactions) nature. Conventional SMPs have two shapes, permanent shape and temporary shape, which is defined by the so-called "programming" procedure. Take the thermally triggered SMP as an example. Typically, the programming process starts with a deformation of the SMP at a temperature above the transition temperature, for example, glass transition T_g for amorphous SMPs or melting transition T_m for crystalline or semi-crystalline SMPs. For ease of discussion, however, we hereafter refer only to glass transition T_g. While maintaining the shape (strain) or stress, the temperature is lowered to below T_g. With the subsequent removal of the applied load, a temporary shape is created and fixed. This completes the programming process. It is noted that programming does not necessarily need the temperature event. Programming can also be conducted at glassy state (it is termed as cold-programming), as long as the SMP can be stressed to beyond yielding [43-46]. The recovery process, depending on the application where the recovery strain or stress is important, can be either under free or constrained boundary conditions, respectively. During the free recovery, SMP is heated to a temperature above T_g under zero stress and the change in strain is measured. On the other hand, during the stress recovery, deformation is not allowed while the polymer is heated to above T_g and the stress is measured. Partially constrained shape recovery by applying a certain stress to the SMP during shape recovery is also frequently used [47]. The shape memory performance of thermally triggered SMPs depends on their complex interactions in polymer structures and morphologies (e.g., the crosslink density, molecular length), the programming conditions (e.g., programming temperature, cooling rate, pre-strain) and recovery conditions (e.g., recovery temperature, heating rate, boundary condition). This offers substantial potentials and considerable opportunities for designing SMPs. An extension of this classical "dual-SMPs" is the "multi-SMPs", which is defined as a shape memory polymer that can be programmed to exhibit more than one distinctive shape change in the recovery event [48-52].

The actuation of the aforementioned SMPs are irreversible and are thus defined as "one-way SMPs (1W-SMPs)". The applicability of the classical 1W-SMPs is restricted by their one-way feature, i.e., 1W-SMPs do not autonomously return to their temporary shapes upon cooling. Recently developed two-way shape memory polymers (2W-SMPs) featuring a reversible shape

memory effect are capable of switching back and forth between two different shapes without the need of subsequent mechanical (deformation) work [30, 53]. The reversible bidirectional actuation enabled many applications such as self-sufficient grippers, fixators, fastening devices, cell encapsulations, swimmers, optical gratings, soft robots, morphing structures, smart textiles, self-healing materials, sealants, artificial muscles, etc. [16, 46, 54-57].

Two-way shape memory effect (2W-SME) has been demonstrated in several polymer systems [15, 58-64]. Regardless of composition, architecture and design, the necessary condition for two-way shape memory effect (2W-SME) is a special designed network consists of stable net-points and switching domains that responds to external stimuli. Same as one-way shape memory polymer (1W-SMP), stable net-points can endure the load, retain the permanent shape upon heating and can be constructed using chemical cross-links [15, 59] [61] [60, 62, 63, 65], crystals with high melting temperature [54, 55] and even ionic clusters [16, 66]. The switching domains that have been demonstrated to exhibit 2W-SME are driven by melt/crystallization transition in semi-crystalline polymers, anisotropic/isotropic transition in liquid crystalline polymers, or order disorder transition in ionomer.

Take chemically cross-linked semicrystalline system as an example. As can be seen from Fig. 1-1(a), without the strong chemical cross-links, most of the molecules are floating in the system and tend to have coordinated segmental motion or even slide against each other when subjected to external load, which leads to irreversible shape changing. The chemically cross-linked system (Fig. 1-1(b)), however, can endure the load, form a stable network and retain the permanent shape upon heating. As a matter of fact, it has been demonstrated that many polymers can exhibit both one-way and two-way shape memory effect. In these polymer systems, what makes 2W-SMP different from 1W-SMP is essentially the anisotropy of the network, which is introduced via a series of programming steps. Afterwards, the reversible actuation behavior can be guided by the anisotropic network, and is driven by the temperature-sensitive response of the switching domains (crystal/melt transition in this semicrystalline system). A straightforward strategy to introduce anisotropy into the network is by applying an external tensile load. As can be seen in Fig. 1-1(c), the 2W-SME is realized by applying an external load at high temperature, followed by cooling (Fig. 1-1(d)) and heating (back to Fig. 1-1(c)) under the constant load. It has been confirmed both experimentally [67] and theoretically [68, 69] that the formation of switching (crystalline) domains is preferentially aligned in the loading direction, which is the main reason for the anomalous elongation upon cooling. This type of 2W-SME is designated as *quasi* 2W-SME, that is, 2W-SME with a constant external load [15, 58-63]. An alternative way to introduce anisotropy is by storing internal tensile stress into the network. This method was first realized in the cross-linked semicrystalline system by building up oriented skeletons via a series of thermomechanical procedures [54, 55, 70], which includes stretching the sample at a high temperature θ_{prog} (Fig. 1-1(c)), cooling down the sample while maintaining the stress $\boldsymbol{T}$ to θ_{low} (Fig. 1-1(d)), unloading, and finally heating the sample to θ_{work} without loading (Fig. 1-1(e)). Normally, the high temperature in the working cycle θ_{work} is lower than the programming high temperature θ_{prog} to ensure partial melting condition. At this moment, internal stress is stored within the partially melt crystalline lamellae, most likely via the amorphous molecular chains tightened by unmelt oriented crystals (Fig. 1-1(e)). In the following working cycle, the sample is ready to serve as a *true* 2W-SMP, which is referred to the 2W-SMP in the absence of external load and can generate reversible actuation during working cycles between θ_{low} and θ_{work} (Fig. 1-1(e)-(f)). In order to be consistent

with classical SMPs, we hereafter define that programming procedure is completed with the unloading step and the working cycle starts with heating the sample to θ_{work}. The temperatures and the programming stress should be elegantly selected to ensure that the stored internal stress is large enough to guide the oriented crystallization and eventually lead to overall elongation upon cooling.

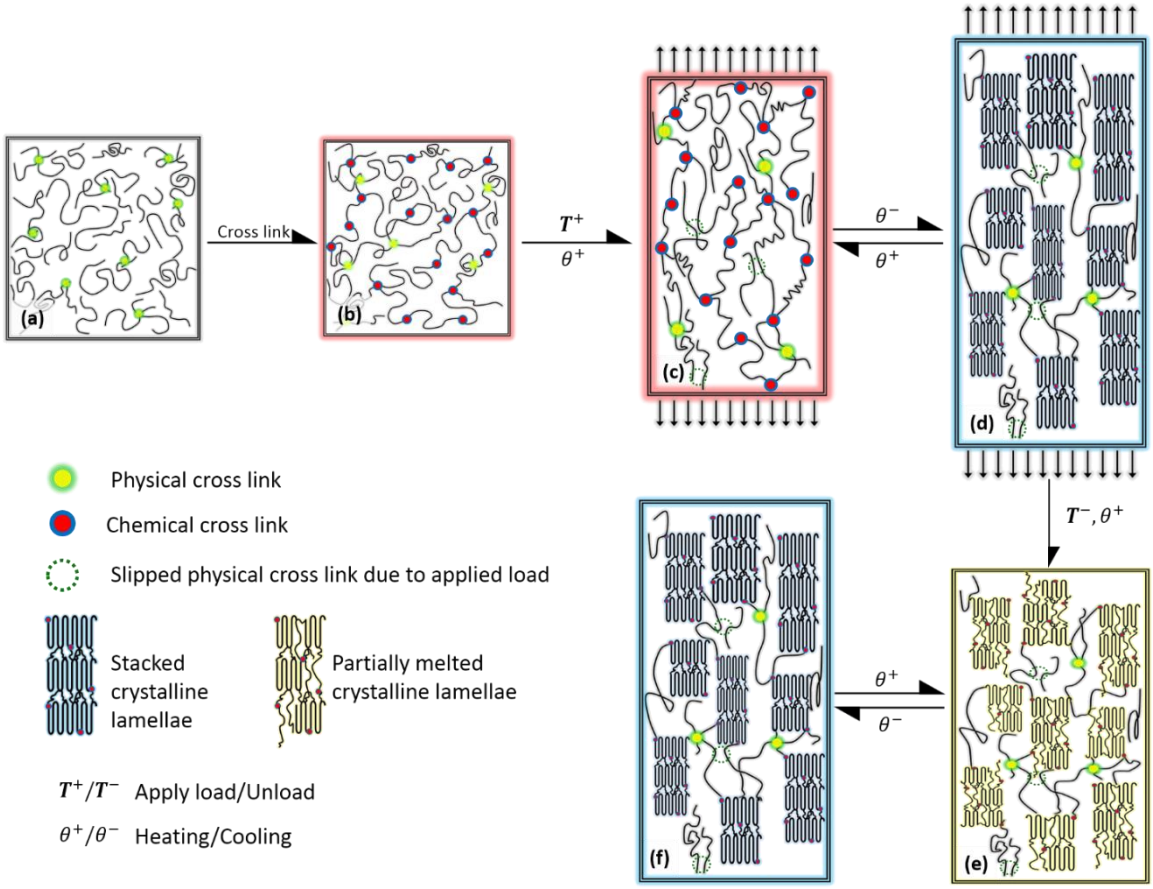

Figure 1-1 Illustration for the working mechanism of the chemically cross-linked 2W-SMP at molecular level. (a) Polymer system without strong chemical cross-links. (b) Chemically cross-linked polymer system. (c) Chemically cross-linked polymer under load at high programming temperature θ_{prog}. (d) Cooling down the sample under load to the low temperature θ_{low}, elongation upon cooling can be observed. (e) Remove the load and heat the sample to high working temperature θ_{work}, and the oriented crystalline lamellae are partially melt. (f) Cooling the sample to the low temperature θ_{low}, elongation upon cooling can be observed. (c) and (d) represent *quasi* 2W-SME (with external tensile load) and (e) and (f) represent *true* 2W-SME (without external tensile load).

In the recent work by Lu and Li [66], the authors have first demonstrated an integrated shape memory effect that includes one-way, *quasi* two-way, and *true* two-way in an ionomer system (Surlyn 8940), in which ionic clusters act as the stable net-points and crystallizable polyethylene segments serve as the switching domain. In their work, *quasi* 2W-SME can be realized with or without a programming procedure. Nevertheless, a tensile programming procedure can enhance the 2W-SME, and as such, smaller external load is required to trigger the *quasi* 2W-SME during

the working cycle (Fig. 9 and Fig. 10 in [66]). A critical value of programming stress is required to achieve *true* 2W-SME (See Fig. 7 in [66]). These phenomena further confirm the fact that both external applied load and programming procedure contribute to the anisotropy of the network that leads to 2W-SME.

1.1.2 Twisted-then-coiled polymeric artificial muscles

Artificial muscles are a class of biologically inspired materials or devices that can reversibly contract, expand, or rotate by external stimuli, such as voltage [71-73], pressure [74, 75], current [76-78], or temperature [27, 79]. Recently, artificial muscles have become a popular topic in both academic and industrial areas: innovative actuation devices based on various mechanisms have been invented and advanced materials with performances surpassing those of natural muscles in many aspects have been developed.

The widely used dielectric elastomer actuator (DEA) is constructed based on the simple mechanism, that is, electrostatic attraction between conductive layers [72]. Albeit a simple design principle with wide operating temperatures and large actuation strains, the high driven voltages (~1 kV) can be a concern, particularly in biomedical and toy applications. Actuators based on ferroelectric materials are realized by the application of an electric field, which results in permanently aligned and polarized domains until the Curie point is reached [71]. The high driven voltage, substantial hysteresis and difficulty in synthesis have become its key limitations. Liquid crystal elastomers (LCEs) exhibit good response times, and moderate to large strains under significantly lower voltage than that in ferroelectrics and dielectric elastomers [73]. However, since investigation of LCEs is still at a very early stage, lack of material information, low stiffness and high cost have become their main limitations. Actuators based on current, or movement of ions, such as conducting polymers [76], ionic polymer metal composites [77], and hybrid carbon nanotube yarns [78] have demonstrated outstanding mechanical properties, but have limited reversibility and cycle rate. Other actuators, for instance, pneumatic artificial muscle [74], electro-thermally driven shape memory alloy [79], and shape memory polymer [27], etc., all suffer from low scalability, high cost and limited cycle-ability. A comprehensive review of the emerging artificial muscle actuators can be found in the work by Madden et al. [80] and Mirvakili et al. [81]. In summary, artificial muscles are of practical interest, but few types have been commercially exploited due to the various limitations discussed above. Therefore, an inexpensive, fast, non-hysteretic and scalable actuator, which can deliver high force with minimal weight and long cycle life, is highly desired to fulfil the requirement for various fields.

Recently, in a surprising breakthrough in the world of material science, Haines et al. [82] have created new artificial muscles that can offer a hundredfold increase in power over natural muscles of equivalent lengths. They have demonstrated that the low cost fishing lines or sewing threads can actively contract and expand after being twisted then coiled into helical spring. The highest tensile stroke achieved was 34% for a temperature variation of ~220 ℃, compared with 4% strain for the untwisted fiber. Its giant tensile stroke, record energy density, quick response, and easy tuning procedure are some notable advantages of this novel class of artificial muscles. Subsequently, a series of experimental characterizations on the twisted fishing line fibers and coiled artificial muscles have been conducted by a number of researchers [83-85], aiming at providing information and useful data for future engineering applications. A custom experimental

test-bench and procedure have been developed and employed by Moretti et al. [85] to systematically run isothermal and isometric tensile tests on nylon-made coiled actuators [84]. The results revealed some important issues related to the response of these actuators, such as hysteresis, repeatability, predictability and stored elastic energy. Aziz et al. [83] standardized the methods for characterizing both the torsional stroke and torque generated, and various testing modes were studied, which replicated possible application conditions: free stroke in a one-end tethered fiber, torsional actuation against an externally applied torque, blocked rotation to determine the generated toque, and torsional actuation against a return spring fiber. Because the muscles can be indefinitely long, they could find uses in both miniaturized and macroscopic actuators. The robustness, commercial availability, and low cost of the polymeric muscles further confirm the significance of this innovative discovery and has opened new horizons toward the development of effective devices, for instance, morphing airplanes and vehicles [86], self-healing composite [87, 88], robotics [89], etc.

It is worth mentioning that the concept of twisting then coiling a fiber for the purpose of actuation is not limited to the polymer fiber. It has also been conducted previously on carbon nanotube yarns [78, 90] and niobium nanowires [81]. However, they exhibited much lower performance than fishing lines did. In their work, the authors explained the torsional actuation behavior from purely kinematic point of view, where the rotation angle was expressed simply by geometrical parameters, i.e., yarn diameter, length, and volume.

1.2 Research Motivation and Objectives

Polymer actuators are becoming more prevalent within the scientific and industrial communities by virtue of their versatility, bio-degradation, scalability and low cost, etc. Because of the inherent complexity of the polymer-based material responses, theoretical and computational models are highly desired. The models not only facilitate interpretation of the underlying mechanisms of the materials, but also provide an investigative platform to evaluate the importance of various factors to the material properties. Therefore, the purpose of this study is to develop usable, high-fidelity constitutive models for various polymeric actuators and seek high performance polymeric actuators.

1.3 Dissertation Outline

The dissertation deals with fourth types of polymeric actuators. In Chapter 2, a physics-based model for classical one-way amorphous shape memory polymers is established. In Chapter 3, a phenomenological model for two-way semicrystalline shape memory polymers is developed. In Chapter 4, a multi-scale modeling framework for the thermomechanical actuation responses of polymeric artificial muscles made of fishing lines is developed. In Chapter 5, artificial muscles made of two-way shape memory polymer fibers has been demonstrated both experimentally and theoretically. Chapter 6 summarizes the main achievements of the study, along with discussion on potential topics for future work.

CHAPTER 2 THERMOMECHANICAL MODELING OF AMORPHOUS ONE-WAY SHAPE MEMORY POLYMERS

In this work, the one-way shape memory effect in amorphous shape memory polymers was reproduced. The amorphous shape memory polymer was treated as a frozen-phase matrix with active-phase inclusions embedded in it. A phase evolution law was proposed from the physics perspective and the Mori-Tanaka approach was used to predict the effective mechanical properties. The theoretical predictions were compared with available experimental results and reasonable agreement was found. The influence of the intrinsic material structures and the thermomechanical conditions on the shape memory behavior were evaluated by parametric studies.

2.1 Introduction

In engineering applications of shape memory polymers, constitutive models are highly desired to provide a fundamental design tool. However, constitutive modeling is very involved because of the inherent complexity of the shape memory behavior. While considerable experimental investigations into SMPs have been reported in the literature, the number of published works dedicated to constitutive modeling constitutes only a small portion of the vast volume of published literatures. Earlier methods [91-94] used rheological models consisting of springs, dashpots, and frictional elements to interpret the thermomechanical behavior of SMPs. Such distinctly simple models have recently been expanded into three dimensional finite deformation model and reasonable results were obtained [95, 96]. Diani et al. [97] developed a three dimensional thermoviscoelastic constitutive model based on a physical understanding of the material behavior. This thermodynamically motivated model is able to capture some critical features of the shape memory behavior, however, it does not predict the details of the response in the thermomechanical cycle. To further capture the time- and temperature-dependent feature of amorphous SMPs, a thermoviscoelastic model that incorporated structural relaxation and stress activated viscoplastic flow in the glassy region was proposed from a microscopic point of view [98]. The model was able to predict key features of the stress hysteresis of the constrained recovery response, including the peak stress and associated temperature. Subsequently, Chen and Nguyen [99] performed a parameteric study of Nguyen et al.'s model [98], and drew the conclusion that the recovery behavior was insensitive to the parameters for viscoplastic flow of materials programmed above T_g. However, Li and Xu [44] argued that the viscoplastic flow plays an important role in the transition between equilibrium and non-equilibrium configuration of SMPs when cold-programmed (program below T_g), and a thermoviscoelastic–thermoviscoplastic constitutive model was then developed on top of that to predict the nonlinear shape memory behavior of the SMP trained below T_g. To further improve the model prediction of time-dependent shape memory behavior, more sophisticated models that contained multiple relaxation times [34, 91, 99-103] were used to describe the broad distribution of stress and structural relaxation times typically displayed by thermoset polymer. Recently, the established 3D multi-branch model [100] has been applied successfully to predict various time-and temperature- dependent shape memory behavior [104-106]. In addition to this dominated thermoviscoelastic approach, in recent years, SMP modeling methods have even incorporated molecular dynamic simulation [107], quantum mechanics [108], multi-scale modeling [109], and statistical mechanics [110], etc. Of all these methods, the phase evolution approach, first proposed by Liu et al. [111] and further developed by other researchers

[112-127] has become another widely used modeling approach due to its easy of application in design.

The phase evolution approach was originally developed for shape memory alloys (SMAs) to describe their pseudo-elastic thermo-mechanical response, stress induced phase transformation phenomena, and hence the shape memory behavior [128-139]. Unlike in SMAs, however, the concept of "phase" in SMPs may not necessarily be physically based, but rather phenomenologically based. In other words, in amorphous SMPs, the physical regions with different material properties and the boundaries between them may not be measurable. In the first SMP phase evolution model [111], a one-dimensional, small strain and rate independent constitutive model were developed by considering the SMP system as a two-phase composite consitsting of an active and a frozen phase. In the active state, the deformation mainly causes a change in entropy and the resulting stress can be determined by the entropic rubber theory. In the frozen phase, the entropic changes are "locked" owing to a decreased mobility of individual polymer chains and the resulting stress is primarily due to changes in the internal energy. Therefore, the entropic stress generated in the active state is frozen, or stored, and can only be released by heating above the transition temperature to reactivate the entropic changes. Based on the work by Liu et al. [111], Chen and Lagoudas [113, 114] extended the model to a three-dimensional framework and this model was used by Volk et al. [125] to examine the free and constraint recovery behavior of shape memory polyurethane (SMPU). Kim et al. [119] developed a three-phase phenomenological model (one hard segment phase and two (active and frozen) soft segment phases) to provide more proper prediction for the deformation behavior of SMPUs. In Wang et al.'s work [126], parameters related to heating rate and hysteresis were introduced. Qi et al. [122] developed a three dimensional finite deformation model for thermomechanical behavior of SMPs, based on the evolution of the deformation energy from an entropy- to an enthalpy-based state. Reese et al. [123] formulated the model in both macromechanical and micromechanical formats and the the thermomechanial coupling was taken into account. Baghani et al. [112] presented a three-dimensional phenomenological model under time-dependent multiaxial thermo-mechanical loadings in the small strain regime. In the work by Gilormini and Diani [115], one point that was left open by Chen and Lagoudas [113, 114] about combining the model of Liu et al. [111] with homogenization models that would be more accurate than the uniform stress assumption was addressed. Most recently, a constituve model for SMP with more physically based phase evolution law has been proposed by Guo et al. [116]. Once the SMP system is considered as a two-phase composite, its effective elastic properties can be determined by various well developed composite material theories [140-146].

The concept of phase transition approach is not only very straightforward, it can also be applied to a wide variety of SMP materials with different transition mechanisms: It can find solid physical base in semicrystalline SMPs [124]: Westbrook et al. [147] successfully applied the phase-based modeling approach to the one-way and two-way shape memory effect in semicrystalline poly(cyclooctene) (PCO) SMP; Long et al. [148] recently has developed a model for photo-activated shape memory elastomers that treats the material as a mixture of two evolving networks, the original network and the photo-stimulated reformed network.

In the framework of phase transition modeling, the formulation of a suitable phase evolution law, in other words, the frozen phase volume fraction, $\phi(T)$ is essential. A variety of frozen phase volume fraction functions have been proposed by researchers and some typical functions are listed

in Table 2-1. As can be seen from Table 2-1, although these evolution laws possess simple form, the parameters in the equations cannot be explicitly related to the inherent material properties and structures (cross-linking density, molecular length, etc.), nor the thermomechanical conditions (heating rate, pre-strain, etc.). Up to now, the lack of physical explanation has become the main limitation of the phase transition approach.

Table 2-1 Frozen phase volume fraction functions proposed in existing literatures.

Frozen phase volume fraction $\phi(T)$	Reference
$\phi(T) = 1 - \frac{1}{1+c_f(T_h-T)^n}$	[111]
$\phi(T) = \frac{1}{1+\exp(-\frac{(T-T_t)}{a})}$	[122]
$\phi(T) = \alpha\exp(-\left(\frac{T_t}{T}\right)^m \beta^{-n})$	[126]
$\phi(T) = \frac{1}{1+\exp(\frac{2w}{T-T_t})}$	[123]
$\phi(T) = \frac{b-\tanh((T-A)/B)}{b-a}$	[125]
$\phi(T) = \left(1 - \left(\frac{T-T_{min}}{T_{max}-T_{min}}\right)^m\right)^n$	[115]
$\phi(T) = \int_{T_s}^{T} \frac{1}{S\sqrt{2\pi}}\exp(-\frac{(T-T_g)}{2S^2})\,dT$	[116]

This present work aims at developing a physics-based phase evolution law so that the phase transition approach can be used more widely with confidence in the future. In the second section of this paper, a brief review on the theory of glass transition is given, which is important to phase evolution for amorphous polymers. Then, a general phase evolution law for amorphous SMPs is elucidated and the frozen phase volume fraction function is formulated, based on the existing theories. In the section that follows, the constitutive relations for the amorphous SMPs are developed using the established evolution law, together with the classical composite materials theories. Our model is then applied to the SMP system used by Liu et al. [111] and the modeling results are verified with the experimental data. Finally, a parametric study is performed to evaluate the influence of several key parameters on the phase evolution law.

2.2 Phase evolution law

2.2.1 Perspectives on glass transition

For amorphous SMPs, shape recovery takes place near the glass transition region. Typically, there are two explanations for the driving force in the shape recovery. One is entropy driven [31] and the other is structural relaxation driven [44, 98] when SMPs evolve through the glass transition region. In the entropy driven theory, the driving force for shape recovery is the conformational entropy of the molecular chains in terms of micro-Brownian thermal motion. Thermodynamically, the molecular chains experience a change from an ordered but temporary configuration to its original random and coiled configuration during the shape recovery process. Since this process is accompanied by an increase in entropy, it is thermodynamically an autonomous process. In the structural relaxation driven theory, it is suggested that the dramatic change in the temperature dependence of the molecular chain mobility underpins the thermally activated shape memory

phenomena of SMPs. The fact that the structure relaxes instantaneously to equilibrium at temperature above T_g but responds sluggishly at temperature below T_g suggests that, reheating programmed SMPs to above T_g reduces the viscosity, restores the mobility and allows the structure to relax to its equilibrium configuration, which leads to shape recovery.

Because of this, understanding the glass transition is the key to elucidating the shape recovery behavior of amorphous SMPs. Despite many decades of intensive research, the glass transition phenomenon is still one of the most challenging topics in polymer science. The glass transition was first explained from the thermodynamic aspect due to the development of calorimetric measurement techniques [149, 150]. In order to explain the questions and paradox identified by Kauzmann [151], glass transition studies were deviated into kinetic direction, where the kinetic properties, such as shear viscosity, mean shear-stress and thermal relaxation time, and the self-diffusion constant were discussed. Among the numerous approaches successfully accounting for the steep increase in the relaxation time of the glass transition with decreasing temperature, the most employed is the so-called Vogel-Fulcher-Tammann (VFT) equation [152-154] and the subsequent GD (Gibbs and DiMarzio)-AG (Adam and Gibbs) theory [155, 156]. In the last decades, the research in glass transition has seen an explosive growth, thanks to the remarkable development in computation power and experimental techniques. New conceptual tools have been introduced (such as energy landscape [157]), new theoretical directions have been pioneered (for example, the random energy models [158]), and new experimental results have been established (for instance, the spatially heterogeneous dynamics [150, 159-161]. These developments provide a solid physical background for our phase evolution law.

2.2.2 Formulation of phase evolution law

- **Facts and assumptions**

One of the recent developed theories on glass transition, the dynamic heterogeneity suggested the co-existence of spatially separated regions of various sizes in amorphous polymer system, whose relaxation dynamics can differ from each other by a factor of up to five orders of magnitude [160]. Therefore, when observed at an intermediate time scale, the whole system can then be classified into immobile and mobile domains, which correspond to frozen and active phases, respectively, in shape memory polymer studies. In particular, in the immobile domains, or the frozen phase, the molecular chains are restricted by the secondary interaction and cannot move cooperatively; while in the mobile domains, or the active phase, the molecular chains can move freely because the interactions between chains have been broken by the external work. The active phase thus has higher energy compared to the frozen phase and work must be done to overcome this barrier when the frozen phase transforms into the active phase. As such, the transformation from the frozen phase to the active phase bears strong resemblance to the energy level transition. Having noticed this, two requirements must be satisfied to ensure the accomplishment of the transition for each domain: first, the size of the domain must reach the critical value so that the transition is thermodynamically stable upon perturbation [162]; second, based on the energy landscape theory [157], sufficient observation time should be given, so that the transition can take place with high probability [163].

In the following, we will formulate the evolution law based on the above facts and the following assumptions for the sake of simplicity: (1) the dynamic heterogeneous domains are spheres with radius r that obey the quasi-Gaussian spatial distribution; (2) the hysteresis in glass transition is neglected here, such that the frozen phase volume fraction functions are the same upon heating and cooling when other conditions are maintained.

- **Evolution law formulation**

As stated above, when a frozen domain is transformed into an active domain, work must be done to overcome the energy barrier. This energy barrier has two resources, one is the bulk free energy difference between the frozen and active domains, and the other is the interfacial energy introduced by the interface between the frozen and active domains. During transformation, a spherical frozen domain with radius r evolves into an active domain (see Fig. 2-1(a)) and the total free energy change caused by the replacement of the active phase is:

$$\Delta G(r) = \frac{4}{3}\pi r^3 G_a + \Gamma - W - \frac{4}{3}\pi r^3 G_f = \frac{4}{3}\pi r^3(\Delta G_B - \Delta G_W) + 4\pi r^2\gamma \qquad (2\text{-}1)$$

where G_a and G_f are the free energy per unit volume for the active and frozen phase at a certain temperature, respectively; Γ is the surface energy between the two phases; W is the external driving energy (due to heat, stress, light, humidity, etc.); ΔG_B is the difference of the bulk free energy between a unit frozen and active domain, *i.e.*, $\Delta G_B = G_a - G_f$; ΔG_W is the free energy change per unit volume by the external work; and γ is the surface energy density which is assumed to be constant. The total free energy change as a function of radius r is sketched in Fig. 2-1(b). As can be seen from the figure, there exists a critical radius r_c (when ΔG reaches the maximum value ΔG_c). Only when the domain is large enough (larger than r_c) can the as-formed active phase survives from fluctuation and stays stable. Let us now formulate each component in Eq. (2-1).

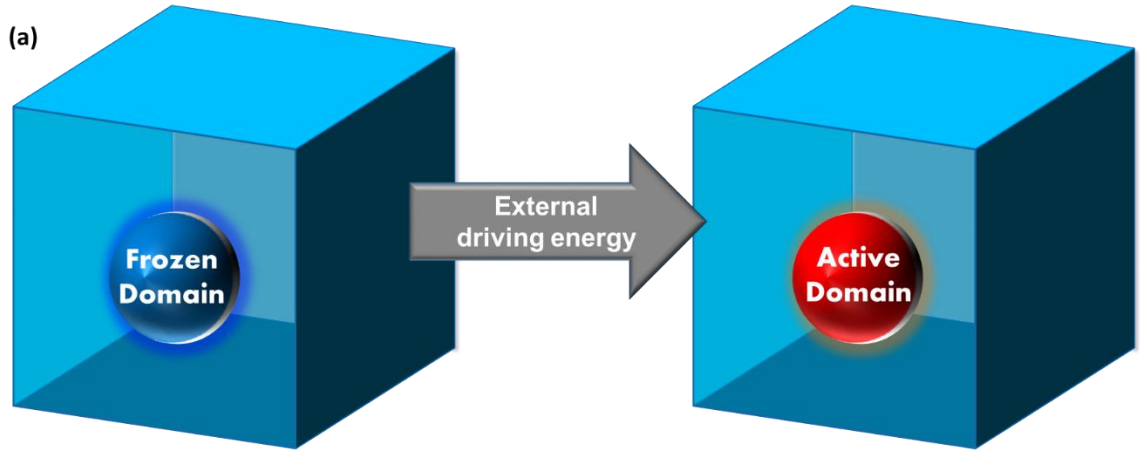

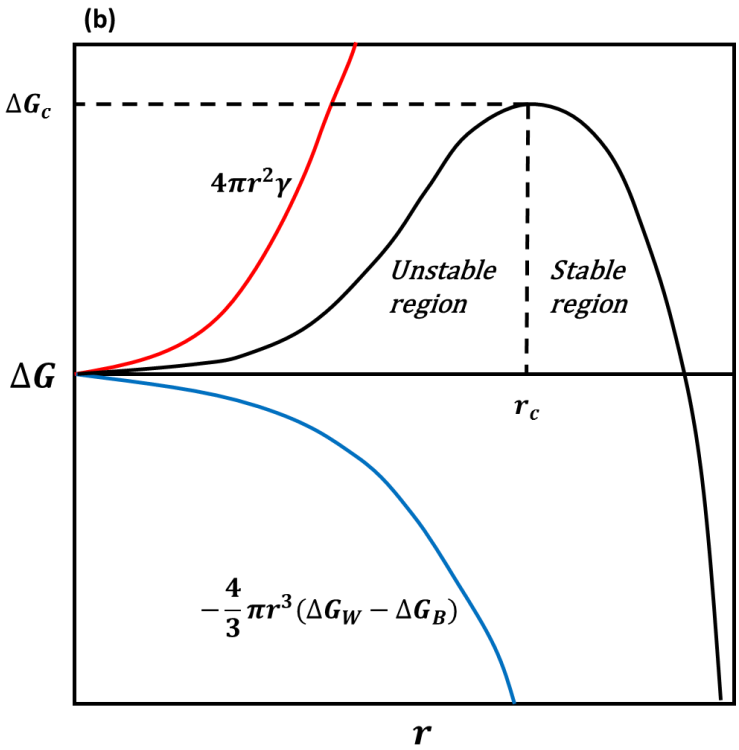

Figure 2-1 Schematic illustration of how a frozen domain (blue sphere) in the frozen phase matrix (blue cube) evolves into an active domain (red sphere). (b) The free energy change caused by the appearance of the active domain as a function of domain radius r. ΔG_c is the energy change when the domain size reaches the critical value r_c. The domains with $r > r_c$, will be stabilized in the active phase (and may grow infinitely upon perturbation); while the domains with $r < r_c$ will revert back to the frozen phase upon fluctuations.

As we know, the Gibbs free energy change (unit volume) is defined as:

$$\Delta G_B = \Delta H_B - T\Delta S_B \tag{2-2}$$

where ΔH_B is the enthalpy change and ΔS_B is the entropy change. In the frozen phase, the molecular chains can hardly move; they can only vibrate near their equilibrium positions. In the active phase, on the contrary, the molecular chains are able to move cooperatively. To trigger this motion, activation energy with the amount of ΔH_a for each structural unit (*i.e.* polymer segments) is needed. Studies have shown that the activation energy ΔH_a is temperature dependent [164] and the enthalpy change thus has the simple form:

$$\Delta H_B(T) = nN\Delta H_a = nN\frac{Ak_B}{(1-T_r/T)^2} \tag{2-3}$$

where n is the molecular chain density (number of molecular chains in unit volume), N is the number of unit segments (Kuhn segments) in one molecular chain and k_B is the Boltzmann constant. A and T_r are constants and can be determined by linear dielectric spectroscopy [165-167].

To detail the entropy contribution to the free energy change, we make the following assumptions: firstly, we neglect the vibrational entropy change and only consider the

configurational entropy change; secondly, suppose that, in the frozen state, the configurational entropy component can be ignored, in other words, the polymer chains cannot form various configurations; finally, in the active state, the polymer chains act as idea chains and the probability density has the form of Gaussian distribution. We can take the value of the end-to-end distance L to calculate the entropy. Bearing these in mind, the average entropy contribution ΔG_S to the free energy change of n molecular chains with N segments of equal length l is:

$$\Delta G_S = -T\Delta S_B = < \frac{3}{2} n k_B T \lambda^2 > \approx \frac{3}{2} n k_B T \tag{2-4}$$

where the stretch $\lambda = \mathrm{L}/L_0$, and $L_0 = \sqrt{N}l$ is the random-walk root-mean-square distance of a chain. We simply take the average value of $\bar{\lambda} = 1$ into Eq. (2-4) to estimate the average entropy contribution.

In summary, the difference in bulk free energy between a unit frozen domain and an active domain is:

$$\Delta G_B = n k_B \left(\frac{NA}{(1-T_r/T)^2} + \frac{3}{2}T\right) \tag{2-5}$$

As pointed previously, the source of external work can be heat, force, light and humidity, etc. For the external thermal work density g_{tw}, suppose that in the frozen phase, the polymer segments only vibrate more drastically upon heating without change the configuration before the phase transformation, this portion of work is thus considered to be proportional to the temperature, *i.e.*, $g_{tw} = c_{tw}T$. Regarding the external mechanical work g_{mw}, it has been observed before that stress can also induce glass transition and this phenomena was explained by the generalized Eyring's ideas of stress-dependent rearrangement activation energies [168-171]. Therefore, this term cannot be ignored, especially in cold programming procedure where the pre-stress is high. When consider the non-thermal triggered SMPs, such as photo-activated or water-activated SMPs, work done by light g_{lw} or humidity g_{hw} should be taken into consideration. Then, the change in free energy by the external work takes the form:

$$\Delta G_W = g_{tw} + g_{mw} + g_{lw} + g_{hw} + \cdots \tag{2-6}$$

Plug Eqs. (2-5) and (2-6) back into Eq. (2-1), we could obtain the expression for the total free energy change ΔG, and hence the equation for the critical size r_c in terms of T:

$$r_c = r_c(T) = \frac{2\gamma}{\Delta G_W(T) - \Delta G_B(T)} \tag{2-7}$$

Also, as mentioned before, the whole system consists of domains with different sizes, and we assume their sizes obey quasi-Gaussian distribution, which is commonly used in polymer science [110, 172-174]:

$$p(r) = \begin{cases} p_0 \exp\left(-\frac{(r-\bar{r})^2}{2\Sigma^2}\right) & r \geq 0 \\ 0 & r < 0 \end{cases} \tag{2-8}$$

where $\bar{r}$ is the average radius, Σ is the standard deviation and p_0 is the normalization factor. The fraction of stable active phase at a certain temperature can thus be expressed as:

$$f_1(T) = \int_{r_c(T)}^{\infty} p(r)dr \tag{2-9}$$

In addition to the size requirement, the observation time scale $\Delta t = \Delta T/\dot{T}$ should be large enough so that the transition between different energy levels can be finished. More specifically, larger Δt indicates slower heating/cooling process, while smaller Δt means the heating/cooling rate is higher. According to the transition state theory [163, 175], the probability f_2 of the transition from frozen to active phase at temperature T and in observation time Δt is:

$$f_2(T, \Delta t) = 1 - [1 - \exp(-\frac{\Delta H_a(T)}{k_B T})]^{\frac{\Delta t}{\tau_0}} \tag{2-10}$$

Here, τ_0 is the internal time scale for the transition with energy barrier $\Delta H_a(T)$.

The two requirements have to be satisfied simultaneously. Therefore, the active phase fraction at a temperature T with heating rate $\dot{T}$ can be expressed as:

$$\phi_a(T, \dot{T}) = f_1 f_2 = \int_{r_c(T)}^{\infty} p(r)dr \times \{1 - [1 - \exp(-\frac{\Delta H_a(T)}{k_B T})]^{\frac{\Delta t}{\tau_0}}\} \tag{2-11a}$$

Accordingly, the frozen phase fraction is:

$$\phi_f(T, \dot{T}) = 1 - \phi_a = 1 - \int_{r_c(T)}^{\infty} p(r)dr \times \{1 - [1 - \exp(-\frac{\Delta H_a(T)}{k_B T})]^{\frac{\Delta t}{\tau_0}}\} \tag{2-11b}$$

2.3 Constitutive relations

As stated previously, the whole material is regarded as a two-phase composite whose volume fractions are temperature and rate dependent and obey the evolution law described in the last section. The evolution law plays a central role in the model: the overall elastic behavior, thermal expansion and most importantly, the shape memory effect are highly related to the frozen volume fraction and are detailed in the following three sections.

2.3.1 Effective elastic stiffness

When heating the SMPs, more and more frozen domains evolve into active domains. It is then reasonable to consider the system as a two-phase composite with random distributions of active (rubbery-like) inclusions in a frozen (glassy-like) matrix. Therefore, the Mori-Tanaka approach can be used to predict the effective elastic properties of SMPs. By assuming isotropic spherical inclusion and isotropic matrix, the formulae for the effective properties take the simple form derived by Weng [176]:

$$\overline{K} = K_f(1 + \frac{\phi_a(K_a/K_f - 1)}{1 + \alpha_1 \phi_f(K_a/K_f - 1)}) \tag{2-12a}$$

$$\bar{G} = G_f\left(1 + \frac{\phi_a(G_a/G_f - 1)}{1+\alpha_1\phi_f(G_a/G_f - 1)}\right) \quad (2\text{-}12b)$$

where,

$$\alpha_1 = \frac{1+\nu_f}{3(1-\nu_f)} \quad (2\text{-}13a)$$

$$\alpha_2 = \frac{2(4-5\nu_f)}{15(1-\nu_f)} \quad (2\text{-}13b)$$

in which K_f,K_a and $\bar{K}$ are the bulk modulus of the frozen matrix, rubbery inclusion and composite, respectively. G_f, G_a and $\bar{G}$ are the elastic shear moduli of the matrix, inclusion, and composite, respectively; and ν_f is the Poisson's ratio of the frozen matrix.

2.3.2 Overall thermal expansion

The thermal expansion of the isotropic two-phase composite has been derived by Levin [177] and generalized by Rosen and Hashin [178]:

$$\bar{\alpha} = \phi_f\alpha_f + \phi_a\alpha_a + \frac{\frac{1}{\bar{K}} - (\phi_f/K_f + \phi_a/K_a)}{1/K_f - 1/K_a}(\alpha_f - \alpha_a) \quad (2\text{-}14)$$

Notice that, unlike the model developed by Liu et al., in which $\bar{\alpha}$ was fitted empirically to experimental results, in the present work, $\bar{\alpha}$ is closely related to both the volume fraction and the elastic properties of the two phases. Therefore, it can be determined directly once the evolution law and the elastic properties for each phase are determined.

2.3.3 Shape memory effect

Shape memory effect also depends largely on the phase evolution law: during the programming or cooling step, the polymer changes from active to frozen phase upon negative temperature increment. In this process, part of the strain that is already reached in the active phase shifts to stress-free strain, namely, storage strain. From a microscopic point of view, the equilibrium molecular configurations received in active state cannot be changed drastically when they transform into frozen state due to the decrease in molecular mobility. To satisfy the boundary condition, stress is then re-distributed throughout the whole system. In the recovery or heating step, the stored strain is released when the frozen phase transforms into an active phase. Depending on the boundary condition, either zero load or zero deformation, shape recovery or stress recovery can be observed. The constitutive relations in the thermomechanical cycle can be formulated based on the above understanding of the shape memory mechanism.

- **Programming/Cooling step**

According to the above analysis, during cooling the behavior of the polymer takes the form:

$$\boldsymbol{\sigma} = \bar{\boldsymbol{L}}: (\boldsymbol{\varepsilon} - \boldsymbol{\varepsilon}_{th} - \boldsymbol{\varepsilon}_s) \tag{2-15}$$

with the effective stiffness tensor $\bar{\boldsymbol{L}}$, total strain $\boldsymbol{\varepsilon}$, thermal strain $\boldsymbol{\varepsilon}_{th} = \int_{T_0}^{T} \bar{\alpha}(T)dT$ and storage strain $\boldsymbol{\varepsilon}_s = \int_{T_0}^{T} d\boldsymbol{\varepsilon}_s$.

The stress increment $d\boldsymbol{\sigma}$ and storage strain development $d\boldsymbol{\varepsilon}_s$ is coupled together during the programming step and has been derived by Gilormini and Diani [115]:

$$d\boldsymbol{\sigma} = \bar{\boldsymbol{L}}: (d\boldsymbol{\varepsilon} - d\boldsymbol{\varepsilon}_{th} - d\boldsymbol{\varepsilon}_s) + \left(\frac{\partial \bar{\boldsymbol{L}}}{\partial \phi_f}\bigg|_T \phi_f{}' + \frac{\partial \bar{\boldsymbol{L}}}{\partial T}\bigg|_{\phi_f} \right) : \bar{\boldsymbol{L}}^{-1} : \boldsymbol{\sigma} dT \tag{2-16a}$$

and

$$d\boldsymbol{\varepsilon}_s = -\frac{\partial \bar{\boldsymbol{L}}^{-1}}{\partial \phi_f}\bigg|_T : \boldsymbol{\sigma} \phi_f{}' dT \tag{2-17a}$$

in which $\phi_f{}'$ is the partial derivative of ϕ_f with respect to temperature.

For the simple case of uniaxial load, the equations become:

$$d\sigma = \bar{E}(d\varepsilon - \bar{\alpha}(T)dT - d\varepsilon_s + \left(\frac{1}{9\bar{K}^2}\frac{\partial \bar{K}}{\partial \phi_f}\bigg|_T + \frac{1}{3\bar{G}^2}\frac{\partial \bar{G}}{\partial \phi_f}\bigg|_T \right) \sigma \phi_f{}' dT + (\frac{1}{9\bar{K}^2}\frac{\partial \bar{K}}{\partial T}\bigg|_{\phi_f} + \frac{1}{3\bar{G}^2}\frac{\partial \bar{G}}{\partial T}\bigg|_{\phi_f})\sigma dT) \tag{2-16b}$$

and

$$d\varepsilon_s = \left(\frac{1}{9\bar{K}^2}\frac{\partial \bar{K}}{\partial \phi_f}\bigg|_T + \frac{1}{3\bar{G}^2}\frac{\partial \bar{G}}{\partial \phi_f}\bigg|_T \right) \sigma \phi_f{}' dT \tag{2-17b}$$

During the programming step, the development of the storage strain $d\boldsymbol{\varepsilon}_s$ is recorded and will be recalled in the following recovery step.

- **Recovery/Heating step**

In the work by Gilormini and Diani [115], the recovery behavior was reproduced by simply 'unrolling the history' of the recorded storage strain. In other words, Eq. (2-16) can still be applied when $d\boldsymbol{\varepsilon}_s$ is not given by Eq. (2-17), but read from the recorded programming history. Reasonable agreement was obtained using this method. Nevertheless, the real situation is more sophisticated mainly due to the following two reasons.

Firstly, the glass transition, or the phase evolution behavior depends not only on the intrinsic material properties, but also on the experimental conditions, such as, heating rate, applied force, etc. As we have mentioned in Section 2.2.2, the external factors, or the source of input energy, which is used to overcome the energy barrier, can be heat, force, light and humidity, etc. When the

boundaries are free (in free recovery tests), only thermal work contributes to the phase transformation process. However, when the boundaries of a test specimen are fixed while the temperature is changing (in programming procedure and fully constraint stress recovery tests), stress and hence mechanical work will be applied to the sample which will serve as part of the input energy source. To this end, in Eq. (2-6), in addition to the thermal energy component g_{tw}, the mechanical energy component g_{mw} should also be included when the boundaries of the specimen are fixed. This will lead to different temperature dependence of the frozen phase volume fraction in the free recovery tests, and in the fully constraint recovery test. Therefore, instead of simply using $d\boldsymbol{\varepsilon}_s$ recorded in the programming step, the storage strain that is released in each step of temperature increment in the free and fully constraint recovery tests are $-\boldsymbol{\varepsilon}_s d\phi_a^t$ and $-\boldsymbol{\varepsilon}_s d\phi_a^{tm}$, respectively. Here, we use $\phi_f^{tm}(\phi_a^{tm})$ and ϕ_f^t (ϕ_a^t) to represent the frozen (active) phase volume fraction functions for the case when both thermal and mechanical work are considered (fixed boundary) and for the case when only thermal work is included (free boundaries), respectively.

The second issue appears in the constraint stress recovery process. Unlike the free strain recovery test, where the recovery strain normally shows a plateau at the end of the test, the stress recovery test is more complicated. In some cases, the recovery stress follows a similar pattern to strain recovery, *i.e.*, gradually approaches to a plateau [179, 180]. In some other cases, however, "stress undershoot" [94, 111, 181, 182] and "stress overshoot" [47, 122, 183, 184] are observed. Considering the fact that in a two-phase composite SMP, when the composite is subjected to stress, active phase can make self-adjustment instantly, in other words, it behaves elastically; at temperature well below glass transition, the frozen phase does not have enough time to make adjustment, thus also has elastic behavior. However, when temperature is within the transition region, the relaxation time of the frozen phase is comparable to the observation time. Therefore, in addition to thermal expansion and shape recovery, stress relaxation must be taken into consideration when modeling the stress recovery process.

It is emphasized here that, as a constitutive equation, it should be independent of the boundary conditions. This is the case for the free shape recovery. However, for constrained shape recovery, the constitutive equation (recovery stress-recovery strain relation) seems depending on the boundary condition of the specimens. The reason is that different boundary conditions add different levels of stress on top of the recovery stress. As a result, the constitutive equation seems depending on the boundary conditions. In other words, in free shape recovery, we are testing "materials" (no boundary conditions are involved); in constrained shape recovery, we are testing "structures" (boundary conditions are involved).

The relaxed stress σ_{relx} normally takes the form of multiple relaxation procedures [100, 185-188]:

$$\boldsymbol{\sigma}_{relx} = \sum_{i=1}^{n} \boldsymbol{\sigma}_{relx}^{i} = \sum_{i=1}^{n} \boldsymbol{\sigma}_i (1 - \exp(-\frac{t}{\tau_i})) \tag{2-18}$$

In our model, the relaxation processes caused by thermal deformation (corresponds to structural relaxation) and mechanical deformation, or releasing of the storage strain (corresponds to stress relaxation) are considered separately, as suggested by preliminary studies [44, 98, 186]. Then, we use $n = 2$ to represent the relaxation mechanisms caused by thermal and mechanical deformation, respectively. The relaxed stress component corresponds to thermal deformation or

structural relaxation is named as $\boldsymbol{\sigma}_{relx}^{th}$; similarly, the relaxed stress component related to mechanical deformation or releasing of the storage strain is defined as $\boldsymbol{\sigma}_{relx}^{rel}$.

For σ_{relx}^{th}, the simplest model is applied [100]:

$$\boldsymbol{\sigma}_{relx}^{th} = \phi_f^{tm}\boldsymbol{\sigma}_{th}^{eff}(1 - \exp(-\frac{t}{\tau_{th}})) \tag{2-19}$$

here we use an effective stress $\boldsymbol{\sigma}_{th}^{eff}$ to represents the stress by thermal expansion only, since it is almost independent of the programming methods; the temperature dependent relaxation time is $\tau_{th} = \tau_{th_0} b(T)$, with the shift factor $b(T) = \exp(-\theta(T - T_g))$.

Regarding $\boldsymbol{\sigma}_{relx}^{rel}$, a similar method is applied [100]:

$$\boldsymbol{\sigma}_{relx}^{rel} = \phi_f^{tm}\boldsymbol{\sigma}_{rel}\,(1 - \exp(-\frac{t}{\tau_{rel}})) \tag{2-20}$$

instead of an effective stress, the current releasing stress $\boldsymbol{\sigma}_{rel}$ (stress caused by releasing of storage strain only, as will be detailed in Table 2-2) is used, since $\boldsymbol{\sigma}_{rel}$ depends largely on programming method; the temperature dependent relaxation time is $\tau_{rel} = \tau_{rel_0} a(T)$ and the shift factor $a(T)$ obeys the Williams-Landel-Ferry (WLF) equation: $\log a(T) = \frac{C_1(T-T_g)}{C_2+(T-T_g)}$.

2.3.4 Summary of the model

Up to this point, the thermomechanical behavior of the amorphous SMP has been analyzed and formulated from a physical perspective. For completeness, the important features of the model are summarized in Table 2-2.

Table 2-2 Summary of the model.

Energy components in Phase evolution law	$\phi_f(T,\dot{T}) = 1 - \phi_a = 1 - (\int_{r_c(T)}^{\infty} p(r)dr) \times (1 - (1 - \exp(-\frac{\Delta H_a(T)}{k_B T}))^{\frac{\Delta t}{\tau_0}})$ $r_c = \frac{2\gamma}{\Delta G_W(T) - \Delta G_B(T)}$ $\Delta G_B = nk_B(\frac{NA}{(1-T_r/T)^2} + \frac{3}{2}T)$ $\Delta G_W = g_{tw} + g_{mw} + g_{hw} + g_{lw} + \cdots$ $\Delta H_a(T) = \frac{Ak_B}{(1-T_r/T)^2}$
Thermomechanical properties	$\bar{K} = K_f(1 + \frac{\phi_a(K_a/K_f - 1)}{1+\alpha_1\phi_f(K_a/K_f-1)})$ $\bar{G} = G_f(1 + \frac{\phi_a(G_a/G_f - 1)}{1+\alpha_1\phi_f(G_a/G_f-1)})$ $\alpha_1 = \frac{1+\nu_f}{3(1-\nu_f)}$ $\alpha_2 = \frac{2(4-5\nu_f)}{15(1-\nu_f)}$

	$\bar{\alpha} = \phi_f \alpha_f + \phi_a \alpha_a + \frac{\frac{1}{\bar{K}} - (\phi_f/K_f + \phi_a/K_a)}{1/K_f - 1/K_a}(\alpha_f - \alpha_a)$
Programming/Cooling Step	$d\boldsymbol{\sigma} = \bar{\boldsymbol{L}} : (d\boldsymbol{\varepsilon} - d\boldsymbol{\varepsilon}_{th} - d\boldsymbol{\varepsilon}_s) + \left(\left.\frac{\partial \bar{\boldsymbol{L}}}{\partial \phi_f}\right|_T \phi_f^{tm\prime} + \left.\frac{\partial \bar{\boldsymbol{L}}}{\partial T}\right|_{\phi_f^{tm}} \right) : \bar{\boldsymbol{L}}^{-1} : \boldsymbol{\sigma} dT$ $d\boldsymbol{\varepsilon}_s = -\left.\frac{\partial \bar{\boldsymbol{L}}^{-1}}{\partial \phi_f}\right|_T : \boldsymbol{\sigma} \phi_f^{tm\prime} dT$
Free Recovery Step	$d\boldsymbol{\varepsilon} = d\boldsymbol{\varepsilon}_{th} + d\boldsymbol{\varepsilon}_{rel}$ $d\boldsymbol{\varepsilon}_{rel} = -\boldsymbol{\varepsilon}_s d\phi_a^t$ $d\boldsymbol{\varepsilon}_{th} = \bar{\alpha} dT$
Constraint Recovery Step	$\boldsymbol{\sigma} = \boldsymbol{\sigma}_{rec} - \boldsymbol{\sigma}_{relx}$ $d\boldsymbol{\sigma}_{rec} = \bar{\boldsymbol{L}} : (d\boldsymbol{\varepsilon} - d\boldsymbol{\varepsilon}_{th} - d\boldsymbol{\varepsilon}_{rel}) + \left(\left.\frac{\partial \bar{\boldsymbol{L}}}{\partial \phi_f}\right|_T \phi_f{}' + \left.\frac{\partial \bar{\boldsymbol{L}}}{\partial T}\right|_{\phi_f} \right) : \bar{\boldsymbol{L}}^{-1} : \boldsymbol{\sigma}_{rec} dT$ $\boldsymbol{\sigma}_{relx}^{th} = \boldsymbol{\sigma}_{eff}^{th} (1 - \exp(-\frac{\Delta t}{\tau_{th}})) \phi_f^{tm}$ $\boldsymbol{\sigma}_{relx}^{rel} = \boldsymbol{\sigma}_{rel} \, (1 - \exp(-\frac{\Delta t}{\tau_{rel}})) \, \phi_f^{tm}$ $d\boldsymbol{\sigma}_{rel} = \bar{\boldsymbol{L}} : (d\boldsymbol{\varepsilon} - d\boldsymbol{\varepsilon}_{rel}) + \left.\frac{\partial \bar{\boldsymbol{L}}}{\partial \phi_f}\right|_T : \bar{\boldsymbol{L}}^{-1} : \boldsymbol{\sigma}_{rec} \phi_f{}' dT$

2.4 Numerical framework and parameter identification

The phase evolution law and the constitutive relations were coded and implemented into the numerical programs to obtain the optimized values for each parameter. The flowchart for the numerical treatment is illustrated in section 2.4.1. Detailed parameter identification procedures are described in section 2.4.2.

2.4.1 Matlab flowchart

Our numerical treatment contains two parts: First, we used the "FindFit" function in Mathematica to identify the optimized values for each parameter. Second, our model, together with Liu's model were coded and implemented into Matlab program to calculate and plot the simulation results.

- **Programming/Cooling step**

In this step, the experimental results of the stress response during cooling with a pre-strain of $\varepsilon_{pre} = -9.1\%$ were used to optimize the parameters in ϕ_f^{tm}, which corresponds to frozen phase volume fraction with both external mechanical and thermal work ($\Delta G_W = g_{tw} + g_{mw}$). The flowchart of the curve fitting procedures is outlined below:

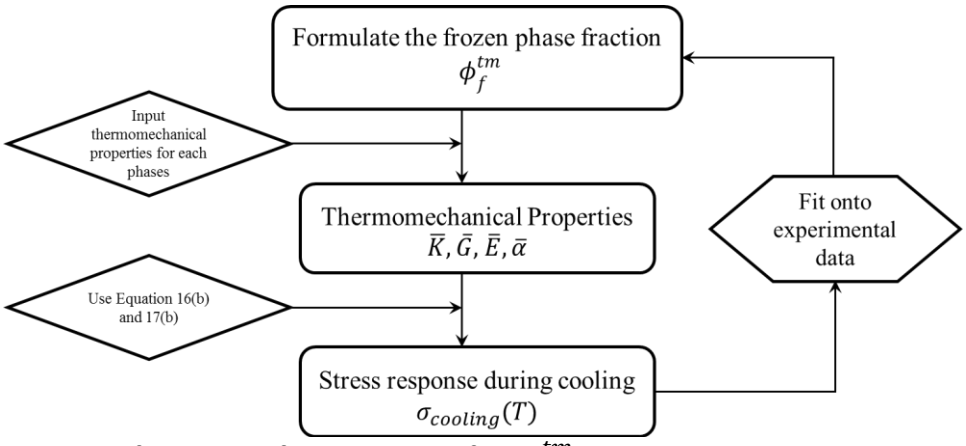

Figure 2-2 Flowchart of the curve fitting process for ϕ_f^{tm} using Mathematica program.

In the following simulation part, this $\phi_f^{tm}$was used as the input frozen phase volume fraction for all the programming and fully constraint recovery tests. Also, notice that, in the programming procedure, the storage strain at each temperature increment $\varepsilon_s(T)$ was recorded for the future use.

- **Free recovery step**

In this step, the experimental data of the free strain recovery test with a pre-strain of $\varepsilon_{pre} = -9.1\%$ was used to obtain ϕ_f^t, which corresponds to the frozen phase volume fraction with only external thermal work $\Delta G_W = g_{tw}$. The curve fitting process are outlined as follows:

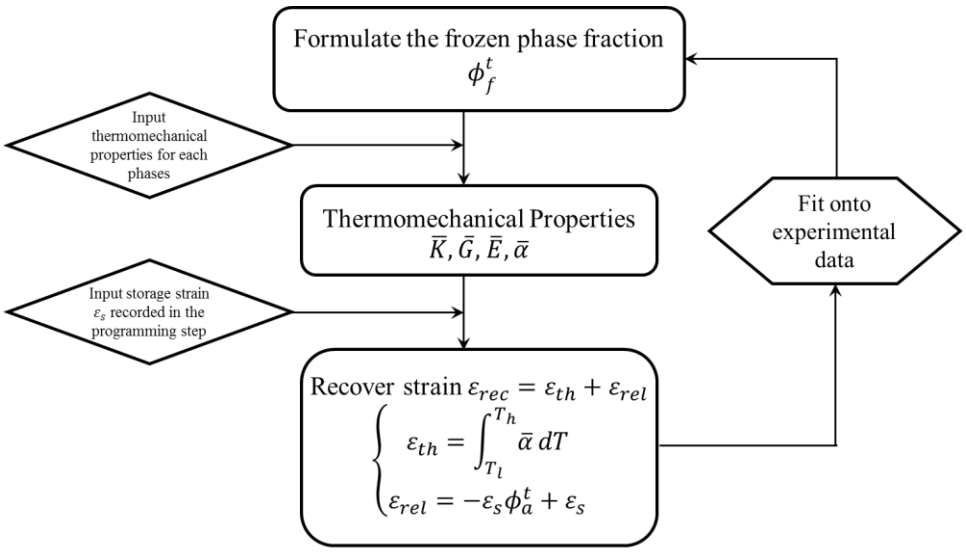

Figure 2-3 Flowchart of the curve fitting process for ϕ_f^t using Mathematica program.

In the following simulation part, the optimized ϕ_f^t was used to reproduce all the free strain recovery tests.

- **Fully constraint stress recovery step**

In this step, the parameters related to the stress relaxation were determined from the stress recovery test result of the $\varepsilon_{pre} = -9.1\%$ pre-strain specimen and curve fitting process are illustrated below:

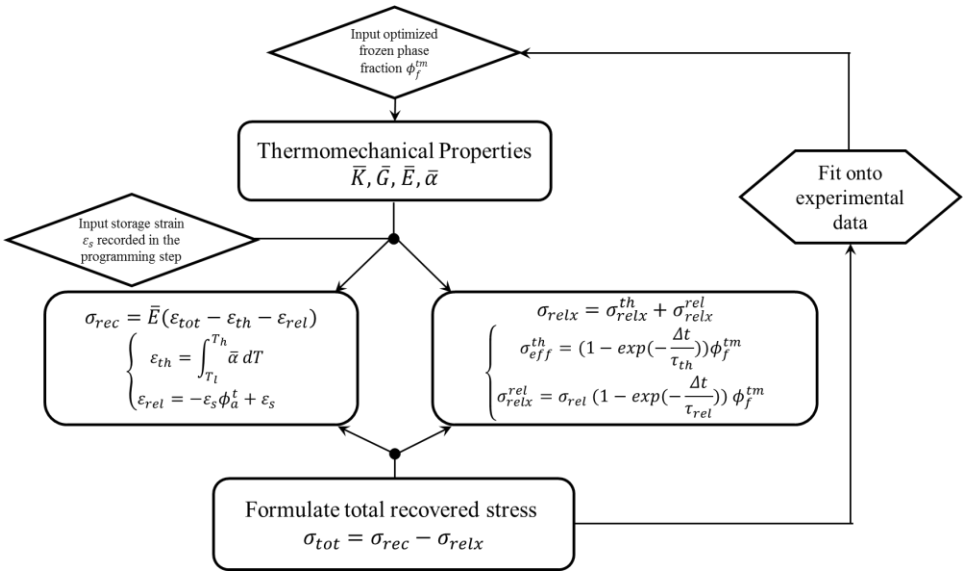

Figure 2-4 Flowchart of the curve fitting process for the parameters related to the stress relaxation using Mathematica program.

The optimized parameters related to the stress relaxation $(\tau_{th_0}, \theta, \tau_{rel_0}, C_1, C_2)$ were used to reproduce other stress recovery test.

2.4.2 Parameter determination

The test specimens were a commercial thermoset epoxy system, DP5.1 supplied by Composite Technology Development (CTD), Inc. Some material parameters can be determined directly from the standard thermomechanical measurements in [111]: the coefficient of thermal expansion for the pure active and frozen phase is respectively $\alpha_a = 1.8 \times 10^{-4}/K$ and $\alpha_g = 0.9 \times 10^{-4}/K$; the Young's modulus is $E_a = (0.025T)MPa$ for non-programmed active phase and $E_f = 750MPa$ for non-programmed frozen phase. As has been observed before [180, 189], the programming step can change the elastic properties to some extents due to the volume change. We found that variation values of $\pm 7\%$ in Young's modulus for compressioned and tensioned samples are reasonable. In the present work, both bulk and shear moduli are required. As suggested by Gilormini and Diani [115], $\nu_a = 0.498$ and $\nu_f = 0.4$ are appropriate values for Poison's ratio of the active and frozen phases, respectively. The parameters related to the stress relaxation were determined from the stress recovery test result of the $\varepsilon_{pre} = -9.1\%$ pre-strain specimen [111].

The procedure to determine the parameters in the frozen phase volume fraction function is more complicated, since these parameters are all related to the intrinsic material properties. However, we have rather limited knowledge about the Epoxy system used in Liu's work. In order to prove the prediction ability of our model and retain the physical meaning of each parameter, we

followed two steps to determine the parameter values: first, set up a rough initial guess based on our knowledge for similar materials, and second, fit the model into the experimental results by Liu et al. Both the initial guess and the allowable variation range are within the test results for the similar material in the existing literature. For example, the surface energy for thermoset epoxy is approximately $\gamma = 0.05N/m$ [190, 191]; the molecular chain density n is roughly equal to the cross-link density (number of cross-link points per unit volume) with a value of $5.9 \times 10^{26} m^{-3}$ used in Liu et al.'s model [111]; the reference temperature T_r was taken as $200K$, which is an average of the theoretical and experimental values [192, 193]; according to the recent experimental results [160, 194, 195], the average size of the dynamic heterogeneous domains is of the order of several nanometer and the initial value is taken to be $2nm$; the product of Kuhn segments N an constant A is estimated by the activation energy associated with the glass transition for the Epoxy system and is set as $1000K$ [182, 196]. The volume fraction ϕ_f^t was fitted onto the strain recovery test result with a pre-strain of $\varepsilon_{pre} = -9.1\%$ and the volume fraction ϕ_f^{tm} with both external mechanical and thermal work was fitted onto the stress response curve during cooling with a pre-strain of $\varepsilon_{pre} = -9.1\%$. The final values of these parameters are listed in Table 2-3.

Table 2-3 Parameters used for the present model.

Description	Parameters	Values
Frozen phase volume fraction		
Average size of the domains	$\bar{r}(nm)$	2.5
Size deviation of the domains when both external thermal and mechanical work are considered	$\Sigma_{tm}(nm)$	0.08
Size deviation of the domains when only external thermal work is considered	$\Sigma_t(nm)$	0.05
Surface tension	$\gamma(N/m)$	0.05
Constant related to external thermal work density	$c_{tm}(J/(mm^3K))$	1.2×10^{-4}
External mechanical work density	$g_{mw}(J/mm^3)$	3.6×10^{-3}
Cross-link density	$n(m^{-3})$	1.5×10^{25}
Number of Kuhn segments between two crosslinks	N	250
Constant related to the linear dielectric spectroscopy of the material	A	4
Reference temperature related to the linear dielectric spectroscopy of the material	$T_r(K)$	200
Heating rate term	$\Delta t/\tau_0$	1
Thermomechanical properties		

Young's modulus for active phase	$E_a(MPa)$	$(0.025T)$
Young's modulus for frozen phase	$E_f(MPa)$	750
Poison's ratio for active phase	ν_a	0.498
Poison's ratio for frozen phase	ν_f	0.4
Coefficient of thermal expansion for active phase	$\alpha_a(K^{-1})$	1.8×10^{-4}
Coefficient of thermal expansion for frozen phase	$\alpha_f(K^{-1})$	0.9×10^{-4}
Glass transition	$T_g(K)$	343
Stress relaxation components		
Relaxation time for thermal expansion	$\tau_{th_0}(s)$	0.1
Material temperature parameter for thermal expansion	$\theta(K^{-1})$	0.1
Relaxation time for shape recovery	$\tau_{rel_0}(s)$	1
WLF constant	C_1	15
WLT constant	$C_2(K)$	350

2.5 Results and discussions

In the work by Liu et al. [111], the SMP samples were programmed in uniaxial tension and compression and were then recovered in unconstraint and fully constraint conditions. These experimental results are frequently used for validation of the models established by other researchers [113-115, 126], which have exhibit similar prediction abilities compared with the model by Liu et al. Here, we also compare our modeling results with the experimental results carried out by Liu et al. [111].

2.5.1 Comparison with experimental results

To have a general idea on the evolution law we discussed above, we first illustrate in Fig. 2-5 the frozen phase volume fraction functions ϕ_f in both cases with the external mechanical work ϕ_f^{tm} and without the external mechanical work ϕ_f^t, together with the results obtained by Liu et al. [111] as a comparison. Notice that the temperature has been normalized by the glass transition temperature (343K) tested by Liu et al. (2006). As can be seen from Fig. 2-5, since both Liu's result and ϕ_f^t in this study were obtained from the free recovery test, they have very similar behavior. With the external mechanical work, the transition starts earlier and is smoother. Although Liu et al.'s phase evolution law possesses a simpler form, it is unable to account for the different conditions due to the phenomenological nature of their model. Our phase evolution law, on the contrary, instead of fitting directly onto the experimental results, starts from the fundamental

physical law, uses the intrinsic parameters of the material, considers the influence of different situations, and can accurately reproduce the frozen phase volume fraction in various cases.

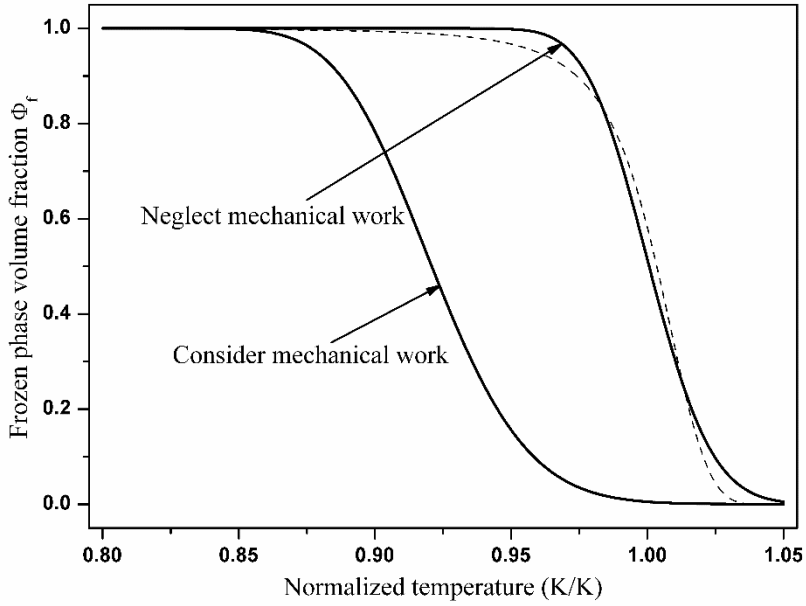

Figure 2-5 Frozen phase volume fraction in both cases with and without the external mechanical work (solid lines), together with the modeling result by Liu et al. [111] (dashed line).

Using the frozen phase volume fraction which considered the mechanical work ϕ_f^{tm}, the stress response during cooling can be reproduced. Fig. 2-6 shows modeling results of the stress responses of the SMPs under different pre-strain conditions. The experiment carried out by Liu et al. and their modeling results are also provided as a comparison. Clearly, our model shows a better agreement with the experimental results as compared to their model. We believe that the more obvious deviation of the model by Liu et al. from the experimental results is mainly due to the fact that the mechanical work was not considered in their model.

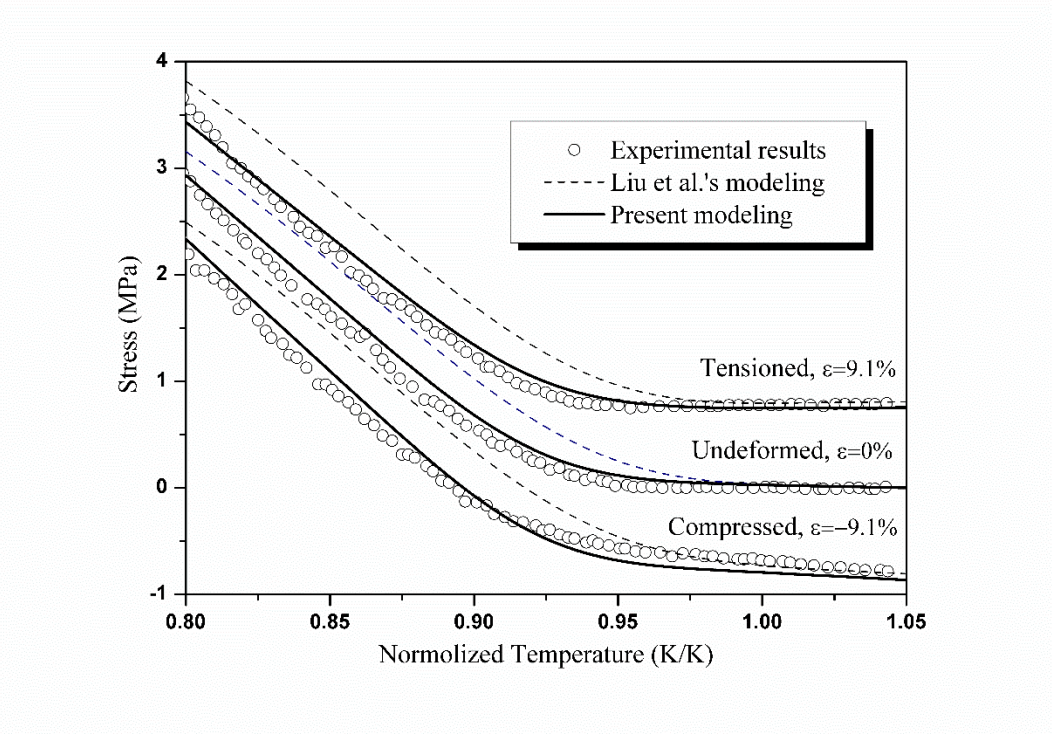

Figure 2-6 Modeling results for the stress responses of SMPs during cooling under different pre-strain conditions.

It is noted that a slightly stiffer behavior at the lower temperatures can be observed for our model as compared to the test results. The reason for this phenomenon is likely attributed the stiff response of the Mori-Tanaka model used to predict the elastic properties of the polymer [109, 197]. At lower temperatures, the frozen phase and active phase is stiffer, leading to even stiffer response by the model. Over estimation of the stiffness leads to consistent over estimation of stress at lower temperatures.

Fig. 2-7 shows the modeling results for the free strain recovery tests of SMPs programmed by different pre-strains. Both our model and Liu's model exhibit good agreement with the experimental results. However, a slightly stiffer behavior at the beginning of the transformation can be observed for our model. One of the many reasons behind this phenomenon may be attributed to our choice of spatial distribution of the frozen domains, that is, quasi-Gaussian distribution. Integration of this quasi-Gaussian distribution (Eq. (2-8)) then leads to the error function which determines mostly the behavior of the phase evolution law. Development of a more accurate, non-Gaussian spatial distribution should be used in the future for a better description.

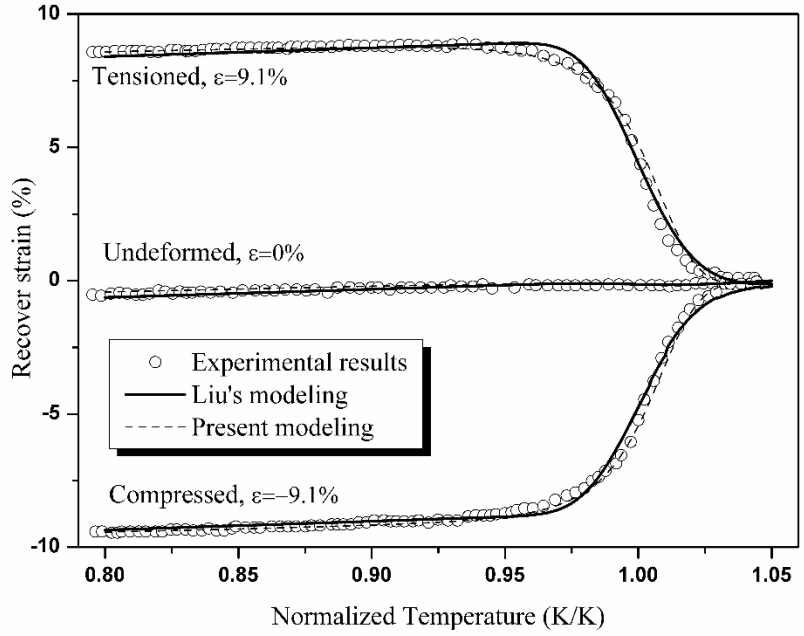

Figure 2-7 Modeling results for the free strain recovery tests of SMPs programmed by different pre-strains.

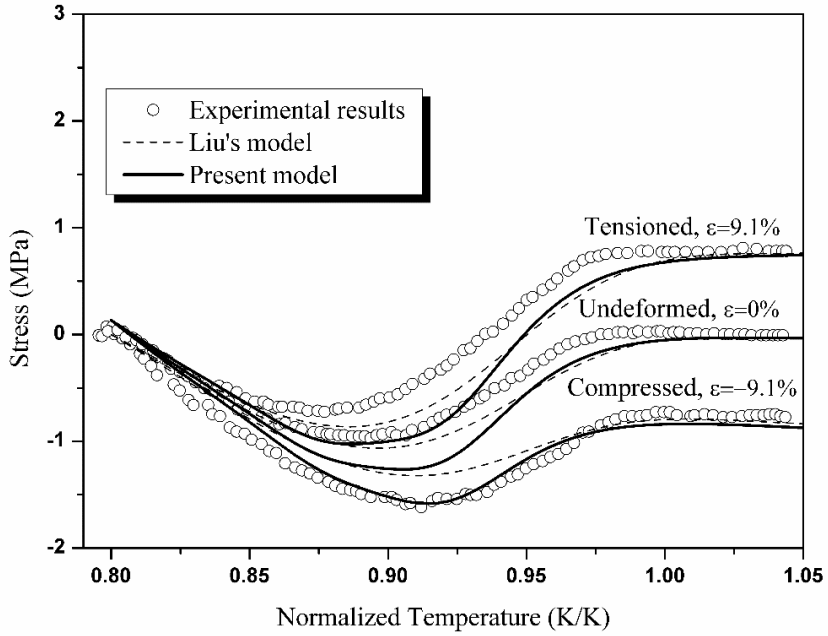

Figure 2-8 Modeling results for the constraint stress recovery tests of SMPs programmed by different pre-strains.

For the fully constraint stress recovery tests, the experimental and modeling results are presented in Fig. 2-8. Both the present and Liu's models show the ability to reproduce the trend of the stress response in fully constrained condition. Notice that, by taking the stress relaxation into consideration in our model, the stress response during fully constraint recovery of the compression sample can be reproduced more accurately. Nevertheless, the relaxation mechanism may be affected by the thermomechanical history. Therefore, when we use the relaxation parameters obtained from the compression programmed sample to predict the stress recovery behaviors of the un-deformed and tensioned samples, a certain deviation is observed (See Fig. 2-8).

2.5.2 Parametric study

As has been proved before [155, 198], the glass transition behavior of amorphous polymers depends largely on their morphologies. In Fig. 2-9(a) and (b), the influence of the average domain size $\bar{r}$ and standard deviation of the domain size Σ defined in Eq. (2-8) are presented. The results in Fig. 2-9(a) indicate that the larger the average domain size is, the earlier the transition starts. This is because when the total dynamic heterogeneous domain volume is constant, the system that consists of smaller domains has higher surface energy that need to be overcome. Therefore, smaller sized domains need higher temperature to trigger the transition.

Fig. 2-9(b) shows that the larger standard deviation of the dynamic heterogeneous domain sizes leads to smoother transition. This is because the larger standard deviation suggests wider distribution of the domain sizes, from very small to very large. Consequently, the transition starts at lower temperature (for larger domain size) and ends at higher temperature (for smaller domain size). In other words, it leads to wider or smoother transition. Hence, a suitable morphology of the polymer is a prerequisite for the proper glass transition behavior.

Another important aspect that affects the phase evolution is the external mechanical work. Although a more accurate method is needed to quantify this portion of work, its necessity has been demonstrated in the above section. As a matter of fact, the stress induced glass transition phenomena has been observed before [169, 171] which provides a solid foundation for our model. As can be seen from Fig. 2-9(c), when the external mechanical work is large enough, the frozen-active phase transition can be triggered at a temperature well below the glass transition temperature. Therefore, by taking the external mechanical work into consideration, the cold programming (program the sample at a temperature lower than the glass transition temperature) shape memory effect can also be explained from the point of view of the phase transition. In other words, owing to the large mechanical work during cold-programming [44], the glass transition temperature has been significantly reduced. Hence, the actual programming temperature is not as cold as it seems.

As has been pointed out in Liu et al.'s work, the heating rate is also a significant factor that determines the phase evolution behavior. In Liu's work, the observation time is comparable with the internal transition time; as a result, the heating was not reflected in their case. However, as shown in Fig. 2-9(d), if the heating rate is too high, the phase transition may not have enough time to complete. In other words, the shape memory effect cannot be fully displayed in the short observation time.

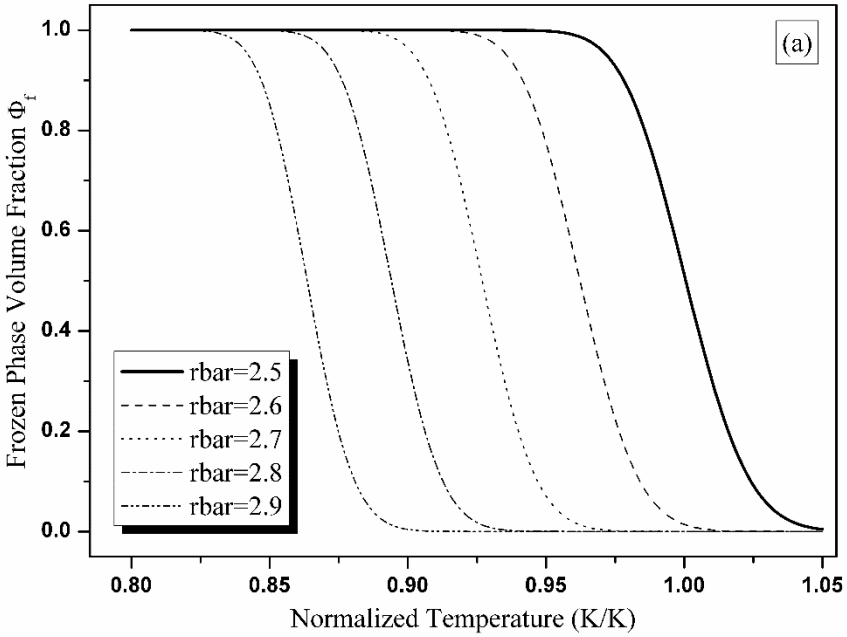
(a)
Frozen Phase Volume Fraction Φ_f
Normalized Temperature (K/K)
rbar=2.5
rbar=2.6
rbar=2.7
rbar=2.8
rbar=2.9
1.0
0.8
0.6
0.4
0.2
0.0
0.80
0.85
0.90
0.95
1.00
1.05

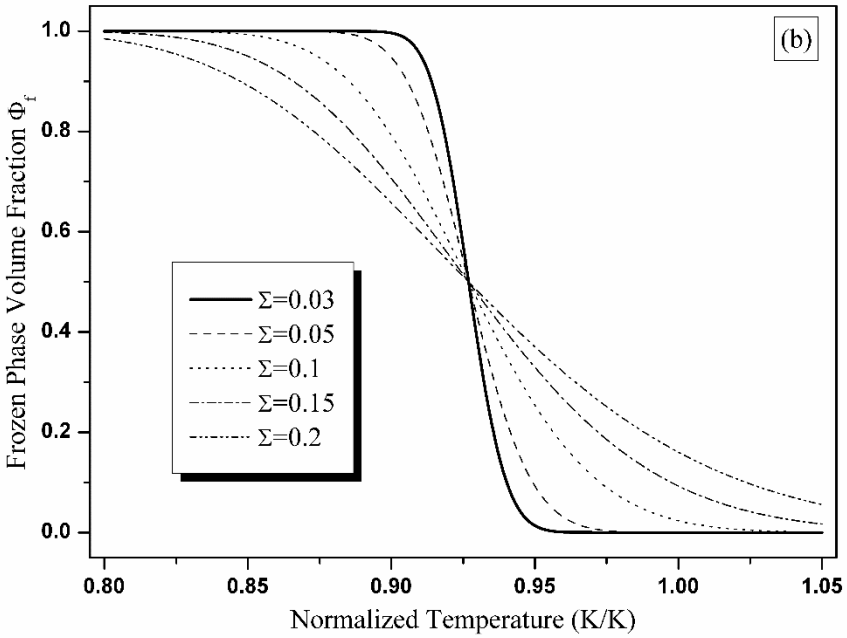
(b)
Frozen Phase Volume Fraction Φ_f
Normalized Temperature (K/K)
Σ=0.03
Σ=0.05
Σ=0.1
Σ=0.15
Σ=0.2
1.0
0.8
0.6
0.4
0.2
0.0
0.80
0.85
0.90
0.95
1.00
1.05

(Figure 2-9 continued)

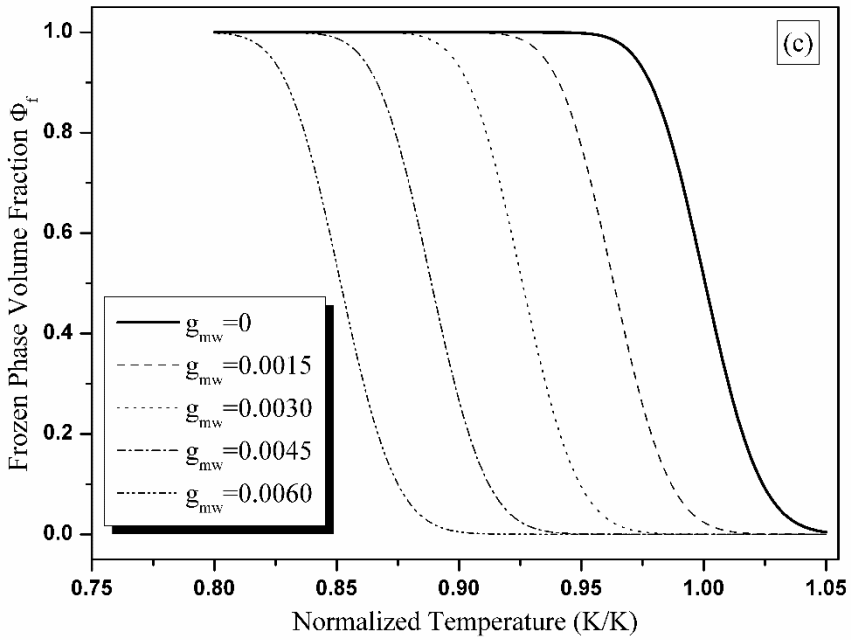

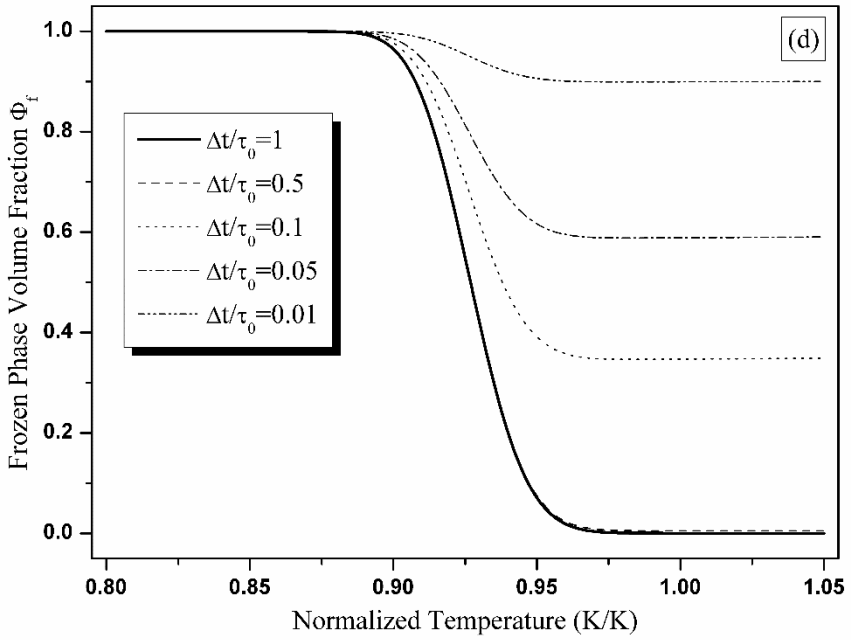

Figure 2-9 Prediction of frozen phase fraction with (a) average domain size $\bar{r}$; (b) standard deviation of the domain size Σ; (c) external mechanical work density g_{mw}; (d) heating rate $\Delta t/\tau_0$.

2.6 Conclusions

The phase transition model is one of the most widely used constitutive models for designing amorphous SMPs due to its ease of application. However, a major concern is the lack of physical basis for the curve-fitted phase evaluation law. In this paper, a new physics based phase evaluation law is formulated. The formulation is based on the concept that amorphous SMPs are a two-phase composite material. The free energy change during the programming and recovery governs the shape fixity and shape recovery. The different boundary conditions during free shape recovery and constrained stress recovery are modeled separately. The modeling results are compared with the test and modeling results found in the literature. Parametric studies are also conducted based on the validated model. The following conclusions are obtained:

(1) The model reasonably captured the shape fixity and shape recovery process, governed by clear physics.
(2) It is found that the dynamic heterogeneous domain size distribution has a significant effect on the memory effect.
(3) External mechanical work, which is not considered in previous models, also has a significant effect on the phase evolution, hence, the shape memory behavior. It also provides new insight into the cold programming principles.
(4) The shape recovery depends on the heating rate. The observation time must be sufficient in order to fully demonstrate the shape memory capability.

While this work focused on amorphous SMPs, the principle and procedure can be easily used in modeling semi-crystalline SMPs, and even polymeric artificial muscles with similar phase transitions.

CHAPTER 3 THERMOMECHANICAL MODELING OF SEMICRYSTALLINE TWO-WAY SHAPE MEMORY POLYMERS

This phenomenological model facilitated the interpretation of 2W-SME and provided some insights into the future design of SMPs with *true* or *advanced* 2W-SME. SMPs with *true* or *advanced* 2W-SME would enhance the scope of applications of SMPs in engineering structures and devices.

3.1 Introduction

A constitutive model is of great benefit to facilitate interpretation and design of 2W-SMP. Although 2W-SME has been realized in polymer systems for almost a decade, the number of published works dedicated to constitutive modeling, especially for *true* 2W-SME, is still rare. The main mechanism of 2W-SME in semicrystalline polymers, or more specifically, elongation upon crystallization and contraction upon melting, is due to the stress-induced crystallization (SIC), which is referred to the fact that the tendency for a polymer to crystallize may be greatly enhanced by deformation. This stress induced crystallization phenomenon has been discovered in polymer system for decades. On the basis of stress-induced crystallization, a phenomenological one-dimensional constitutive model was first developed by Westbrook et al. [147] for the *quasi* 2W-SME, where the semicrystalline switching domain is idealized as an aggregate of rubbery (R) and crystalline (C) phases acting in parallel. Then, a generalized three-dimensional thermodynamic framework was proposed by Hall et al. [199]. A novel theoretical approach based on three element thermomechanical model has been proposed recently by Dolynchuk, et al. [68]. The model took in consideration the viscoelastic deformation of entangled slipping macromolecules using a Kelvin-Voigt element and the effect of cross-link density, by calculating the free energy change of a molecule chain between two neighboring cross-links upon crystallization/melting transformation. Although the *quasi* 2W-SME in some semicrystalline polymers can be reproduced using these models, the *true* 2W-SME has not been accounted for. Because of the scientific and technological importance of *true* 2W-SME, it is highly desired to establish a constitutive framework to guide future design and synthesis of 2W-SMPs, particularly *true* 2W-SMEs achieved through mechanical manipulating or programming.

This present work aims at developing a 3D constitutive model that is able to reproduce the *true* 2W-SME. The paper is organized as follows. Section 3.1 introduces the background and motivations for this study. In Section 3.2, the basic kinematics and balance relations are given. This is followed by the constitutive model development in Section 3.3. The model is then validated by applying to the poly(ethylene-co-vinyl acetate) (PEVA) based 2W-SMP in Section 3.4 and some discussions on the mechanism of *true* 2W-SME are given per the validated model. Finally, in Section 3.5, the important results and findings are summarized.

3.2 Kinematics

Consider a body $\mathcal{B}$ in a reference configuration $\mathcal{K}_0$. Let $\boldsymbol{X}$ denote a typical position of a material point in $\mathcal{K}_0$. Let $\mathcal{K}_t$ be the configuration of the body at a time t. Then the motion

$\mathcal{X}_{\mathcal{K}_0}$ maps each particle $\boldsymbol{X}$ in the configuration $\mathcal{K}_0$ to a position $\boldsymbol{x}$ in the configuration $\mathcal{K}_t$ at time t, *i.e.*,

$$\boldsymbol{x} = \mathcal{X}_{\mathcal{K}_0}(\boldsymbol{X}, t) \tag{3-1}$$

This motion can be attributed to external thermal treatment, mechanical loading or configuration relaxation. The deformation gradient $\boldsymbol{F}_{\mathcal{K}_0}$ is defined through:

$$\boldsymbol{F}_{\mathcal{K}_0} = \frac{\partial \mathcal{X}_{\mathcal{K}_0}}{\partial \boldsymbol{X}} \tag{3-2}$$

The left and right Cauchy-Green stretch tensors are defined through:

$$\boldsymbol{B}_{\mathcal{K}_0} = \boldsymbol{F}_{\mathcal{K}_0}\boldsymbol{F}_{\mathcal{K}_0}^T \tag{3-3a}$$

$$\boldsymbol{C}_{\mathcal{K}_0} = \boldsymbol{F}_{\mathcal{K}_0}^T\boldsymbol{F}_{\mathcal{K}_0} \tag{3-3b}$$

Any acceptable process has to satisfy the appropriate conservation laws. The conservation equations appropriate for studying a mechanical process are the conservation of mass, and linear and angular momentum. We assume that the material is incompressible and consequently the conservation of mass reduces to:

$$\mathrm{div}(\boldsymbol{v}) = 0 \tag{3-4a}$$

where $\boldsymbol{v}$ is the velocity. The conversation of linear momentum leads to:

$$\rho\left[\frac{\partial \boldsymbol{v}}{\partial t} + \boldsymbol{L}\boldsymbol{v}\right] = \mathrm{div}(\boldsymbol{\sigma}) + \rho\boldsymbol{b} \tag{3-4b}$$

where ρ is the density, $\boldsymbol{L} = \mathrm{grad}(\boldsymbol{v}) = \dot{\boldsymbol{F}}\boldsymbol{F}^{-1}$ is the velocity gradient, $\boldsymbol{T}$ is the stress tensor, and $\boldsymbol{b}$ is the body force. The conservation of angular momentum requires that the stress tensor be symmetric. For an incompressible material, the stress tensor $\boldsymbol{T}$ reduces to:

$$\boldsymbol{\sigma} = -p\boldsymbol{I} + \boldsymbol{\sigma}^{\varepsilon} \tag{3-5}$$

where p is the indeterminate part of the stress due to the constraint of incompressibility, and $\boldsymbol{T}^{\varepsilon}$ is constitutively determined extra stress.

3.3 Constitutive Model

As is customary in dealing with thermomechanical deformation, the overall deformation gradient $\boldsymbol{F}$ can be decomposed through a multiplicative decomposition scheme:

$$\boldsymbol{F} = \boldsymbol{F}_m\boldsymbol{F}_t \tag{3-6}$$

where $\boldsymbol{F}_t$ is the thermal deformation and $\boldsymbol{F}_m$ is the mechanical deformation. As has described above, in a chemically cross-linked semicrystalline polymer system, which is the focus in this

study, the reversible actuation is attributed to the switching domains in the cross-linked stable network. In addition to that, some of the molecular chains may not be cross linked and thus may lead to irreversible deformation upon loading. Therefore, the mechanical deformation $\boldsymbol{F}_m$ can be further decomposed into two parts: reversible component $\boldsymbol{F}_r$ and irreversible component $\boldsymbol{F}_{ir}$. With the assumption of uniform stress field distribution throughout the body, we thus have:

$$\boldsymbol{F}_m = \boldsymbol{F}_r \boldsymbol{F}_{ir} \tag{3-7a}$$

$$\boldsymbol{\sigma} = \boldsymbol{\sigma}_r = \boldsymbol{\sigma}_{ir} \tag{3-7b}$$

In what follows, these components are addressed individually.

3.3.1 Thermal component

For an orthotropic material with the principal axes of orthotropy parallel to unit vectors$\boldsymbol{m}$, $\boldsymbol{n}$ and $\boldsymbol{m} \times \boldsymbol{n}$, the thermal deformation gradient $\boldsymbol{F}_t$ is specified by:

$$\boldsymbol{F}_t = \vartheta \boldsymbol{I} + (\beta - \vartheta)\boldsymbol{m} \times \boldsymbol{m} + (\gamma - \vartheta)\boldsymbol{n} \times \boldsymbol{n} \tag{3-8}$$

here, the stretch ratios due to thermal expansion in the orthogonal principle directions $\boldsymbol{m}$, $\boldsymbol{n}$ and $\boldsymbol{m} \times \boldsymbol{n}$ are β, γ and ϑ, respectively. $\boldsymbol{I}$ is the second order unit tensor.

3.3.2 Reversible component

The reversible component for 2W-SMP is attributed to the thermomechanical responses of the switching phase. For switching phase consists of semi-crystalline switching domains, as in our case, this component is typically decomposed into amorphous phase and crystalline phase. The volume fraction of each phase varies with temperature, i.e., crystallization upon cooling and melting upon heating. As stated above, the main mechanism of 2W-SME is due to the stress-induced crystallization (SIC). Specifically, SIC contributes to 2W-SME from two aspects. First, anisotropy can be introduced to crystalline phases formed during crystallization process via (external or internal) stress, and hence to the final solid. This anisotropy is determined by the deformation in the amorphous phase at the instant of crystallization. On the basis of this fact, a phenomenological modeling framework named "multiple natural configurations" has been developed using a continuum theory. This approach has been applied to a large class of materials: twinning [200], traditional plasticity [201], solid to solid phase transformation [202], and most recently semi-crystalline one-way shape memory polymers [203-205]. In Fig. 3-1, we illustrate how the natural configurations evolve along the thermomechanical path. The other contribution from SIC is that crystallization kinetics in polymer can be greatly enhanced by deformation [206]. The reason for this effect is fairly obvious. When the polymer having a network structure is stretched, chains between network junctions are deformed to their most probable configurations, most of them being oriented. The configurational entropies of these chains consequently are decreased. Less entropy remains to be sacrificed in passing to the crystalline state. According to thermodynamic theory, crystallization will occur when $\theta \Delta S_f < \Delta H_f$, where ΔS_f is the change in entropy, ΔH_f is the change in enthalpy, and θ is the absolute temperature. As a result,

crystallization may develop at a higher temperature with smaller ΔS_f. Accordingly, by the end of the crystallization process, more crystallites will be formed to "memorize" the shape. It is worth mentioning that the increase in melting temperature is noticeable only when the stress is large enough and this stress can be either in the form of external stress, or internal stress introduced by programming procedure. This becomes one of the important reasons that a critical programming stress must be reached to realize *true* 2W-SME. In the following, both of these contributions from SIC to the constitutive relationship of the reversible component will be elaborated in detail.

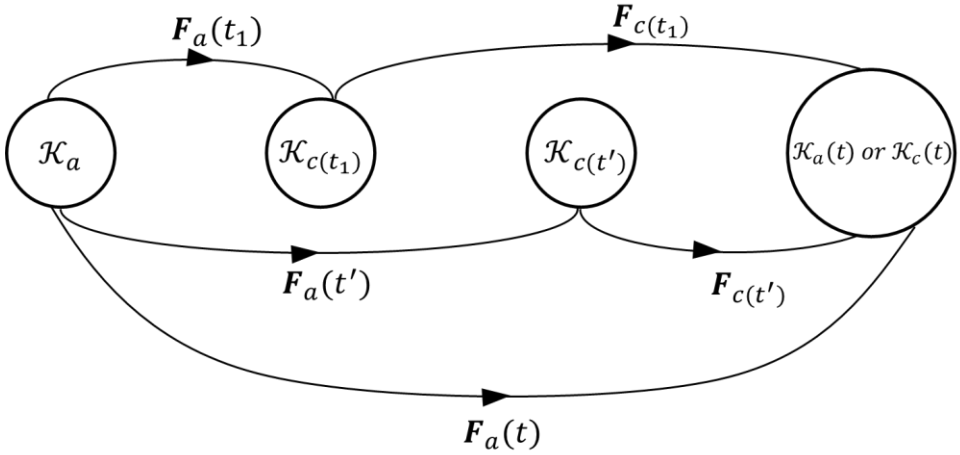

Figure 3-1 Illustration of configuration evolution for a material body that is initially in the amorphous state $\mathcal{K}_\mathrm{a}$. The final observation was taken at time t, when the material can be in either amorphous or crystalline state. Various thermomechanical paths can lead the initial configuration to the final configuration: $\mathcal{K}_\mathrm{a}$ can be deformed $\boldsymbol{F}_a(t)$ and remains in the amorphous state $\mathcal{K}_\mathrm{a}(t)$, or it can be deformed first (e.g. $\boldsymbol{F}_a(t_1)$ or $\boldsymbol{F}_a(t')$), then subjected to crystallization and forms new natural configuration (e.g. $\mathcal{K}_{\mathrm{c}(\mathrm{t}_1)}$ or $\mathcal{K}_{\mathrm{c}(\mathrm{t}')}$), and finally, from this new configuration, it can be further deformed (e.g. $\boldsymbol{F}_{c(t_1)}$ or $\boldsymbol{F}_{c(t')}$) to the final crystalline state $\mathcal{K}_\mathrm{c}(t)$. Notice the deformation gradient designation: $\boldsymbol{F}_a(t)$ indicates the deformation is measured at time t, while $\boldsymbol{F}_{c(t')}$ means the deformation is measured from the crystalline natural configuration that was formed at time t'. Crystallization process starts from time $t_1$and goes through an intermediate time t'. Subscript "a" means amorphous and "c" stands for crystal.

- **Amorphous phase with single natural configuration**

In our work, the amorphous phase is considered to possess a single natural configuration, regardless of the thermomechanical history. Polymers exhibiting rubber-like elasticity are usually modeled as incompressible hyper-elastic materials. In general, the Cauchy stress for an incompressible hyper-elastic materials can be written in:

$$\boldsymbol{\sigma} = -p\boldsymbol{I} + 2\boldsymbol{F}_a \frac{\partial \psi_a}{\partial \boldsymbol{C}_a} \boldsymbol{F}_a^T \tag{3-9}$$

where $\boldsymbol{F}_a$ is the deformation gradient measured from the fixed reference configuration to the current configuration (See Fig. 3-1). ψ_a is the Helmholtz potential function which specifies the particular material model. Many such models are available in the literature, such as Neo-Hookean

model, the Mooney-Rivilin model, and so on. More details on the constitutive relationships for rubber-like materials can be found in [207, 208]. In this work, we assume that the rubbery amorphous component is isotropic, and based on Neo-Hookean model, the constitutive relationship reduces to:

$$\boldsymbol{\sigma} = -p\boldsymbol{I} + \mu_a \boldsymbol{B}_a \tag{3-10}$$

where μ_a is a constant for the amorphous phase modulus.

- **Semi-crystalline phases with multiple natural configurations**

Once the crystallization process starts from time t_1, a fraction of the deformed amorphous domains will evolve into crystallites. For these newly born crystallites, it is believed that they are formed in a stress-free state [209] and can be treated as elastic solid thereafter. The stress for an elastic solid depends on the deformation gradient from the stress-free reference configuration to the current configuration (e.g. $\boldsymbol{F}_{c(t_1)}$ or $\boldsymbol{F}_{c(t')}$ in Fig. 3-1). The stress-free configuration, along with the anisotropy of a crystalline phase is determined by the deformation in the amorphous phase at the instant of formation of this crystallite. It is worth mentioning that crystallization takes place in a gradual manner, instead of occurring instantly. As such, during the cooling process, individual amorphous phases are crystallized at different times, thus "freeze in" different deformation histories (such as $\mathcal{K}_{c(t_1)}$ and $\mathcal{K}_{c(t')}$ in Fig. 3-1) from the corresponding amorphous phases, and finally end up with different deformation responses and constitutive relationships in different phases. Hence, this modeling framework is named as "multiple natural configurations". In order to specify the constitutive relationships for this mixture, some assumptions have to be made for the sake of clarity. We allow co-occupancy of the phases in an averaged sense as is done in traditional mixture [205, 210]. In addition, we assume that the amorphous and crystalline constituents are constrained to move together. Finally, by assuming that the Helmholtz potential of different phases are additive, the general expression for the stress in the mixture at time t during the crystallization process is:

$$\boldsymbol{\sigma} = -p\boldsymbol{I} + (1-\alpha)\mu_a \boldsymbol{B}_a + \int_{t_1}^{t} \boldsymbol{g}_{c(t')}\left(\boldsymbol{F}_{c(t')}\right)\frac{d\alpha}{dt'}\,dt' \tag{3-11}$$

where $\boldsymbol{g}_{c(t')}\left(\boldsymbol{F}_{c(t')}\right)$ is the constitutive relationship function for the crystallite formed at time t', and can be of an anisotropic elastic solid; α is the volume fraction of the newly formed crystallites.

As stated above, the anisotropy of the newly formed crystallites is determined by the orientation of the amorphous phase at the time of crystallization. More specifically, suppose $\boldsymbol{B}_a(t')$ is the stretch tensor for an amorphous phase immediately before it is crystallized, we can use the three mutually perpendicular principal directions to determine the directions of anisotropy in the elastic solid. It seems appropriate that under the unequal stretch in three principal directions, the solid will have orthotropic form of anisotropy, of which directions can be quantified by two of the three eigenvectors of $\boldsymbol{B}_a(t')$, $\widehat{\boldsymbol{m}}_{c(t')}$ and $\widehat{\boldsymbol{n}}_{c(t')}$. In general, $\widehat{\boldsymbol{m}}_{c(t')}$ and $\widehat{\boldsymbol{n}}_{c(t')}$ varies with time.

Without going into further details, for incompressible orthotropic elastic solid, the functional form $\boldsymbol{g}_{c(t')}$ can take the following [204]:

$$\boldsymbol{g}_{\boldsymbol{c}(\boldsymbol{t}')}\left(\boldsymbol{F}_{c(t')}\right) = 2c_1\boldsymbol{B}_{c(t')} + 4\boldsymbol{F}_{c(t')}[c_2(J_1-1)\widehat{\boldsymbol{m}}_{c(t')}\times\widehat{\boldsymbol{m}}_{c(t')} + c_3(K_1-1)\widehat{\boldsymbol{n}}_{c(t')}\times\widehat{\boldsymbol{n}}_{c(t')}]\boldsymbol{F}^T_{c(t')} \quad (3\text{-}12)$$

here, J_1 and K_1 are invariants of the right Cauchy-Green stretch tensor given by:

$$J_1 = \widehat{\boldsymbol{m}}_{c(t')}\cdot\boldsymbol{C}_{c(t')}\widehat{\boldsymbol{m}}_{c(t')} \quad (3\text{-}13a)$$

$$K_1 = \widehat{\boldsymbol{n}}_{c(t')}\cdot\boldsymbol{C}_{c(t')}\widehat{\boldsymbol{n}}_{c(t')} \quad (3\text{-}13b)$$

$c_i's$ are material constants for the elastic solid that depend on the eigenvalues of $\boldsymbol{B}_a(t')$. If all three eigenvalues are distinct, then the solid born at this instant is orthotropic and all three $c_i's$ are non-zero. If two of the eigenvalues are the same and different from the third, then the formed solid is transversely isotropic. Suppose $\widehat{\boldsymbol{m}}_{c(t')}$ is the eigenvector associated with the eigenvalue that is different from the two others, then c_1 and c_2 are non-zero and c_3 vanishes. If all three eigenvalues are the same, then the new born solid becomes isotropic and the only non-zero material constant is c_1.

Another process that involves evolution of natural configurations is the melting process. As temperature increases, a fraction of the crystalline phase jumps back to amorphous phase. At this moment, this phase recalls its original natural configuration in the amorphous state. This results in stress re-distribution throughout the material and overall deformation due to boundary constraints. Since different crystalline phases have different natural configurations and deformation responses after crystallization process, melting of different phases will thus end up with different overall responses. It is therefore necessary to track which fraction of the solid is melting at a given time. A straightforward strategy is to assume that the solids formed last melt first. That is to say, at a certain time t during the melting process, if the crystallinity is the same with that during the crystallization process at time t^*, then, the natural configuration distributions at both instants can be considered equivalent. Accordingly, the constitutive relationship for the melting process at time t can be expressed by changing the upper limit of the integral in Eq. (3-11) into the corresponding time t^*.

- **Phase evolution law**

From a physics perspective, polymer begins to crystallize when the activation criterion is met and the rate of crystallization is determined by the thermomechanical conditions. A plethora of models have been developed to describe this process. Here in our work, for the sake of simplicity, we directly prescribe the phase evolution law using a phenomenological equation:

$$\frac{d\alpha_c(t)}{dt} = R(\Delta\theta)(\alpha_\infty - \alpha_c(t)) \quad (3\text{-}14a)$$

$$R(\Delta\theta) = A_1\Delta\theta^{A_2} \quad (3\text{-}14b)$$

$$\Delta\theta = \theta_m - \theta \tag{3-14c}$$

where α_∞ is the ultimate crystallinity, A_1 and A_2 are constants, and θ_m is the melting temperature. As stated in the introduction, SIC affects the crystallization kinetics by shifting the equilibrium melting temperature θ_m^0 to a higher value θ_m. The effect of stress on the crystallization process becomes prominent only when the stress exceeds a critical value. However, in the extremely high stress range, when the molecules are fully extended, any further increase in the stress will not cause further orientation of the polymer molecules. The effect of stress on the crystallization process in the high stress range should thus tend to a constant value.

To describe the non-isothermal stress induced crystallization kinetics, a simplified model proposed by Guo et al. [211] has been adopted. In their work, the phenomenological relationship between the equilibrium crystallization temperature shift θ_{shift} and the shear stress $\bar{\tau}$ can take the simple form:

$$\theta_{shift} = A_3 \exp\left(-\frac{A_4}{\bar{\tau}_a}\right) \tag{3-15}$$

where A_3 and A_4 are fitting parameters. Notice that, in our work, the shear stress $\bar{\tau}_a(t)$ is taken as the effective shear stress acting on the amorphous phase, which is determined by $\boldsymbol{B}_a(t)$.

3.3.3 Irreversible component

A large strain imposed during the programming procedure will render a plastic irreversible deformation. Since the programming stress is applied at an elevated temperature and the stress is much lower than the tensile strength of the material, we believe that the irreversible deformation is mostly caused by the local re-arrangement of the amorphous molecules above melting temperature, such as rotation, sliding and un-entanglement. Upon cooling, the mobility of the molecules, and hence their ability to re-arrange are diminished. Therefore, the plastic flow slows down as temperature decreases. In this work, a plastic shear strain rate $\dot{\gamma_{ir}}$ is given to help constitutively prescribe the plastic stretch rate $\boldsymbol{D}_{ir}$, which is the symmetric part of the velocity gradient $\boldsymbol{L}_{ir}$:

$$\boldsymbol{D}_{ir} = \dot{\gamma_{ir}}\hat{\boldsymbol{n}} \tag{3-16}$$

where $\hat{\boldsymbol{n}}$ is the unit vector along the deviatoric portion of the driving stress $\mathrm{dev}(\boldsymbol{T}_{ir}^*)$ and this relationship indicates that the plastic stretch rate scales with the plastic shear strain rate and evolves in the direction of the driving stress. The driving force is defined as $\boldsymbol{\sigma_{ir}^*} = \boldsymbol{\sigma_{ir}} - \boldsymbol{\sigma_b}$, where $\boldsymbol{\sigma}_b$ is the back stress to account for the strain hardening effect. In particular, we assume that the back stress is proportional to the plastic deformation γ_{ir} and decreases with temperature. For the flow rule, a strain rate insensitive power law for the effective shear stress $\bar{\tau}_p$ dependence [212] and an Arrhenius type expression for the temperature dependence are used:

$$\dot{\gamma_{ir}} = \dot{\gamma}_0 \left(\frac{\bar{\tau}_{ir}}{\tau_0}\right)^{n_{ir}} \exp\left(-\frac{U_{ir}}{k_B\theta}\right) \tag{3-17}$$

here, $\dot{\gamma}_0$ is the reference shear strain rate; $\bar{\tau}_{ir} = \|\mathrm{dev}(\boldsymbol{\sigma}^*_{ir})\|/\sqrt{2}$ is defined as the equivalent shear stress; n_{ir} is the rate exponent; τ_0 is the reference shear strength; U_{ir} is the flow activation energy and k_B is the Boltzmann constant.

3.4 Application to specific programming-working cycle

In this work, we used chemically cross-linked poly(ethylene-co-vinyl acetate) (cPEVA) based 2W-SMP to validate our model. The 2W-SMP was tension programmed (with $\theta_{prog} = 50℃$ and $\theta_{low} = 0℃$) using different programming stresses ($0.95MPa$, $1MPa$, $1.05MPa$), followed by the same working cycle condition ($\theta_{work} = 40℃$). We first derived the formulation for this specific thermomechanical condition.

3.4.1 General expressions for uniaxial extension

In our two-way shape memory effect experiment, the samples were subjected to uniaxial extension with constant load (or zero load) and this is also a commonly encountered condition in polymer processing. This loading condition leads to three results that can greatly simplify the formulation: first, the deformation can be considered homogeneous throughout the material body; second, the eigenvectors $\widehat{\boldsymbol{m}}_{c(t')}$ and $\widehat{\boldsymbol{n}}_{c(t')}$ remain constant through the process and $\widehat{\boldsymbol{m}}_{c(t')}$ is along the stretching direction; third, the solid formed is transversely isotropic, albeit in an averaged sense, thus c_3 vanishes in Eq. (3-12). In our work, we will focus on this simple extension case. We require incompressible condition to each component of the material (thermal, reversible and irreversible components) and the stress applied to the material is $\boldsymbol{\sigma} = \mathrm{diag}(\sigma, 0, 0)$.

- **Thermal Component**.

The coefficient of thermal extension in the axial direction is assumed to be linear temperature dependent and can be determined using DMA.

- **Reversible Component**.

Under uniaxial extension, the deformation gradients for a material at amorphous and crystalline state are, respectively:

$$\boldsymbol{F}_a(t) = \mathrm{diag}(\lambda_r(t), \lambda_r^{-\frac{1}{2}}(t), \lambda_r^{-\frac{1}{2}}(t)) \tag{3-18a}$$

$$\boldsymbol{F}_{c(t')}(t) = \mathrm{diag}(\frac{\lambda_r(t)}{\lambda_r(t')}, \sqrt{\frac{\lambda_r(t')}{\lambda_r(t)}}, \sqrt{\frac{\lambda_r(t')}{\lambda_r(t)}}) \tag{3-18b}$$

and

$$\boldsymbol{B}_a(t) = \boldsymbol{C}_a(t) = \mathrm{diag}(\lambda_r^2(t), 1/\lambda_r(t), 1/\lambda_r(t)) \tag{3-18c}$$

$$\boldsymbol{B}_{c(t')}(t) = \boldsymbol{C}_{c(t')}(t) = \mathrm{diag}((\frac{\lambda_r(t)}{\lambda_r(t')})^2, \frac{\lambda_r(t')}{\lambda_r(t)}, \frac{\lambda_r(t')}{\lambda_r(t)}) \tag{3-18d}$$

Thus, the invariant $J_1 = (\frac{\lambda_r(t)}{\lambda_r(t')})^2$.

The constitutive relationship function for the crystallite formed at time t' becomes:

$$\boldsymbol{g}_{c(t')} = 2c_1\boldsymbol{B}_{c(t')} + 4c_2\left(\frac{\lambda_s(t)}{\lambda_s(t')}\right)^2 \mathrm{diag}(\left(\frac{\lambda_s(t)}{\lambda_s(t')}\right)^2 - 1, 0, 0) \tag{3-19}$$

Take Eq. (3-19) back to Eq. (3-12), together with the stress free condition on the lateral surfaces, the stress-deformation relationship in the stretching direction is:

$$\sigma_{11} = \sigma = (1-\alpha_c)\mu_a\left(\lambda_r^2(t) - \frac{1}{\lambda_r(t)}\right) + 2c_1\int_{t_1}^{t}(\left(\frac{\lambda_r(t)}{\lambda_r(t')}\right)^2 - \frac{\lambda_r(t')}{\lambda_r(t)})\frac{d\alpha_c}{dt'}dt'$$
$$+4c_2\int_{t_1}^{t}(\left(\frac{\lambda_r(t)}{\lambda_r(t')}\right)^4 - \left(\frac{\lambda_r(t)}{\lambda_r(t')}\right)^2)\frac{d\alpha_c}{dt'}dt' \tag{3-20}$$

The phase evolution rule is determined by Eqs. (3-14) and (3-15), with the effective shear stress in amorphous phase $\bar{\tau}_a = \frac{\sqrt{2}}{3}\mu_a\left(\lambda_r^2(t) - \frac{1}{\lambda_r(t)}\right)$.

- **Irreversible component.**

Under uniaxial extension, the deformation gradient is in the form:

$$\boldsymbol{F}_{ir} = \mathrm{diag}(\lambda_{ir}, \lambda_{ir}^{-\frac{1}{2}}, \lambda_{ir}^{-\frac{1}{2}}) \tag{3-21a}$$

which leads to

$$\dot{\boldsymbol{F}}_{ir} = \mathrm{diag}(\dot{\lambda}_{ir}, -\frac{1}{2}\lambda_{ir}^{-\frac{3}{2}}\dot{\lambda}_{ir}, -\frac{1}{2}\lambda_{ir}^{-\frac{3}{2}}\dot{\lambda}_{ir}) \tag{3-21b}$$

$$\boldsymbol{D}_{ir} = \left[\dot{\boldsymbol{F}}_{ir}\boldsymbol{F}_{ir}^{-1}\right]_{sym} = \mathrm{diag}(\frac{\dot{\lambda}_{ir}}{\lambda_{ir}}, -\frac{1}{2}\frac{\dot{\lambda}_{ir}}{\lambda_{ir}}, -\frac{1}{2}\frac{\dot{\lambda}_{ir}}{\lambda_{ir}}) \tag{3-21c}$$

According to Eq. (3-16), the viscous deformation should satisfy:

$$\frac{\dot{\lambda}_{ir}}{\lambda_{ir}} = \frac{\sqrt{6}}{3}\dot{\gamma}_{ir} \tag{3-22a}$$

with initial condition $\lambda_p(0) = 1$ and $\dot{\gamma}_p$ satisfies the prescribed flow rule:

$$\dot{\gamma}_{ir} = \dot{\gamma}_0\left(\frac{\bar{\tau}_{ir}}{\tau_0}\right)^{n_{ir}}\exp\left(-\frac{U_{ir}}{k_B\theta}\right) \tag{3-22b}$$

here, $\bar{\tau}_{ir} = \frac{\sqrt{3}}{3}(\sigma - \sigma_b)$ and the back stress is assumed to have the form of $\sigma_b = C_{b1}\lambda_{ir} - C_{b2}\theta$.

The shape memory effect experiments generally include two procedures: programming and working procedures. Each procedure consists of different thermomechanical steps. In the following sections, we will derive the equations for different stages.

3.4.2 Step by step expressions for the programming-working cycle

- **Heating up to θ_{prog} (P1) then loading and holding at σ_{P2} (P2 → P3).**

At the beginning of the programming procedure, the sample is heated up to θ_{prog} at zero stress, thus only the thermal component deforms:

$$\lambda_t(t) = 1 + \int_0^t \alpha_t(\theta) \frac{d\theta}{dt'} dt' \tag{3-23}$$

where $\alpha_t(\theta)$ is the coefficient of thermal expansion. Afterwards, the applied stress is increased stepwise from zero to the designated programming stress σ_{P2} at θ_{prog}. In a general case, the sample is considered to have a crystallinity of α_{P1} that does not melt at θ_{prog} and we assume that the solids remain in the materials formed without different deformation histories, *i.e.*, $\lambda_r(t') \equiv 1$. In such a case, the stress σ in the mixture is given by:

$$\sigma(t) = (1-\alpha_{P1})\mu_a \left(\lambda_r^2(t) - \frac{1}{\lambda_r(t)}\right) + \alpha_{P1}[2c_1(\lambda_r^2(t) - \frac{1}{\lambda_r(t)}) + 4c_2(\lambda_r^4(t) - \lambda_r^2(t))] \tag{3-24}$$

This equation holds in step P2 and P3 until the crystallization starts at t_1 upon cooling in step P4. The same stress also applies to the irreversible component and the viscoplastic deformation is determined by Eqs. 3-22.

In our experiment where the stress σ is specified, the deformations for each component are therefore readily to be solved using the above equations.

- **Cooling down to θ_{low} with constant stress (P4).**

According to Eq. 3-20, the stress-stretch relation during the crystallization procedure in the reversible component is re-written as:

$$\sigma = (1-\alpha_c(t))\mu_a \left(\lambda_r^2(t) - \frac{1}{\lambda_r(t)}\right) + \alpha_{P1}\left[2c_1\left(\lambda_r^2(t) - \frac{1}{\lambda_r(t)}\right) + 4c_2\left(\lambda_r^4(t) - \lambda_r^2(t)\right)\right]$$
$$+2c_1(\lambda_r^2(t)L_1 - \frac{1}{\lambda_r(t)}L_2) + 4c_2(\lambda_r^4(t)L_3 - \lambda_r^2(t)L_1) \tag{3-25}$$

where L_1, L_2 and L_3 are integrals that contain information about the natural configuration evolution history and are defined by:

$$L_1(t) = \int_{t_1}^t \left(\frac{1}{\lambda_r(t')}\right)^2 \frac{d\alpha_c}{dt'} dt' \tag{3-26a}$$

$$L_2(t) = \int_{t_1}^{t} \lambda_r(t') \frac{d\alpha_c}{dt'} dt' \tag{3-26b}$$

$$L_3(t) = \int_{t_1}^{t} \left(\frac{1}{\lambda_r(t')}\right)^4 \frac{d\alpha_c}{dt'} dt' \tag{3-26c}$$

The phase evolution rule is described in Section 3.3.2, with initial value of α_0.

- **Unloading at $\boldsymbol{\theta_{low}}$ (P5).**

At this stage, the effective cross-linked network in the reversible component is a mixture of amorphous and crystalline phases with different natural configurations. We assume that during the unloading step, the crystalline phase does not evolve further. In the experiment, the stress is unloaded instantly. The expression for the stretch is then reduced to:

$$0 = (1-\alpha_{P4})\mu_a \left(\lambda_r^2(t) - \frac{1}{\lambda_r(t)}\right) + \alpha_{P1}\left[2c_1\left(\lambda_r^2(t) - \frac{1}{\lambda_r(t)}\right) + 4c_2\left(\lambda_r^4(t) - \lambda_r^2(t)\right)\right]$$
$$+2c_1(\lambda_r^2(t)L_1(t_2) - \frac{1}{\lambda_r(t)}L_2(t_2)) + 4c_2(\lambda_r^4(t)L_3(t_2) - \lambda_r^2(t)L_1(t_2)) \tag{3-27}$$

where α_{P4} is the crystalline fraction after step P4 before unloading at time t_2 and the upper limit for the integrals L_1, L_2 and L_3 change to t_2. The programming procedure is completed with the unloading process, and the crystallinity α_c and the natural configuration evolution history $L_{\#}$'s should be recorded, so that they could be recalled during the following working cycle.

- **Heating up to $\boldsymbol{\theta_{work}}$ (W1).**

As stated above, during the melting process, to track the configuration evolution of the phases, the first step is to identify the corresponding time t^* during crystallization process in step P4, at which the material has the same crystalline fraction with current time t in the melting process W1. Then, the expression for the stress-stretch relationship can be written as:

$$0 = (1-\alpha_c(t))\mu_a \left(\lambda_r^2(t) - \frac{1}{\lambda_r(t)}\right) + \alpha_{P1}\left[2c_1\left(\lambda_r^2(t) - \frac{1}{\lambda_r(t)}\right) + 4c_2\left(\lambda_r^4(t) - \lambda_r^2(t)\right)\right]$$
$$+2c_1(\lambda_r^2(t)L_1(t^*) - \frac{1}{\lambda_r(t)}L_2(t^*)) + 4c_2(\lambda_r^4(t)L_3(t^*) - \lambda_r^2(t)L_1(t^*)) \tag{3-28}$$

where $t^* \in [t_1, t_2]$. For the phase evolution rule in the melting process, the Eqs. (3-14) need to be altered accordingly:

$$\frac{d\alpha_m}{dt} = -R(\Delta\theta)\alpha_m(\theta) \tag{3-29}$$

with $\Delta\theta = \theta - \theta_m^0$.

- Cooling down to $\boldsymbol{\theta_{low}}$ (W2).

In this step, the stress-stretch relationship is the same as Eq. 3-25, except for that the applied stress is zero and the initial natural configuration distribution is taken the same as that at the end of the last melting process (W1), instead of zeros in step P4. Therefore, the crystalline kinetic, hence the natural configuration distribution evolution during this process is also different from that in the programming crystallization process. For the rest of the working cycle (W3→W4), the similar process applies.

3.4.3 Matlab flowchart

The model were then coded and implemented into the Matlab program to reproduce the programming-working cycle of the 2W-SME and the Matlab flowchart is presented in Fig. 3-2.

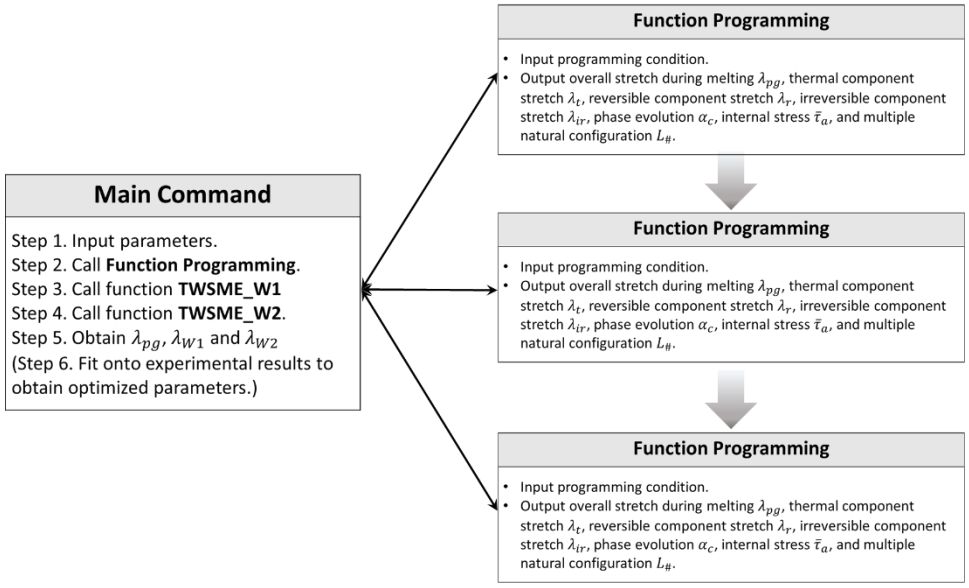

Figure 3-2 Matlab flowchart for complete programming-working cycle.

3.5 Results and Discussions

3.5.1 Parameter determination

The coefficient of thermal expansion (CTE) was measured via a temperature scan test under a force controlled mode using DMA. A linear temperature dependent CTE ($\alpha_t = a_1 T + a_2$), hence a quadratic temperature dependent displacement, was used to fit onto the experimental results to obtain the parameters in the thermal component (See Fig. 3-2(a)). For the rest of the parameters, the experimental results from the complete programming and first working cycle with $1MPa$ programming stress were used. The optimized parameters are listed in Table 3-1.

Table 3-1 Model parameters.

Description	Parameter	Value
Thermal Component α_t		
Constant for CTE	$a_1\ (K^{-2})$	8.2468×10^{-6}

Constant for CTE	$a_2\ (K^{-1})$	-2.4066×10^{-3}
Reversible Stretch Component λ_r (Eq.3-20)		
Constant for amorphous phase modulus	$\mu_a\ (MPa)$	0.63
Constant for crystalline phase axial modulus	$c_1\ (MPa)$	1.55
Constant for crystalline phase transverse modulus	$c_2\ (MPa)$	0.14
Phase evolution law α_c (Eqs. 3-14 and 3-15)		
Crystallinity before programming	α_0	0.75
Equilibrium melting temperature	$T_m^0\ (K)$	298
Ultimate crystallinity	α_f	0.85
Constant for phase evolution	A_1	1×10^{-4}
Constant for phase evolution	A_2	1.35
Constant for stress induced crystallization effect	$A_3\ (K)$	35
Constant for stress induced crystallization effect	$A_4\ (MPa)$	0.06
Irreversible Stretch Component λ_{ir} (Eq. A5)		
Reference shear strain rate	$\dot{\gamma}_0\ (s^{-1})$	7.5×10^{-7}
Reference shear strength	$\tau_0\ (MPa)$	6.5×10^{-3}
Strain rate exponent	n_{ir}	2.35
Flow activation energy	$U_{ir}\ (J)$	10
Constant for back stress	$C_{b1}(MPa)$	0.73
Constant for back stress	$C_{b2}\ (MPa/K)$	3×10^{-4}

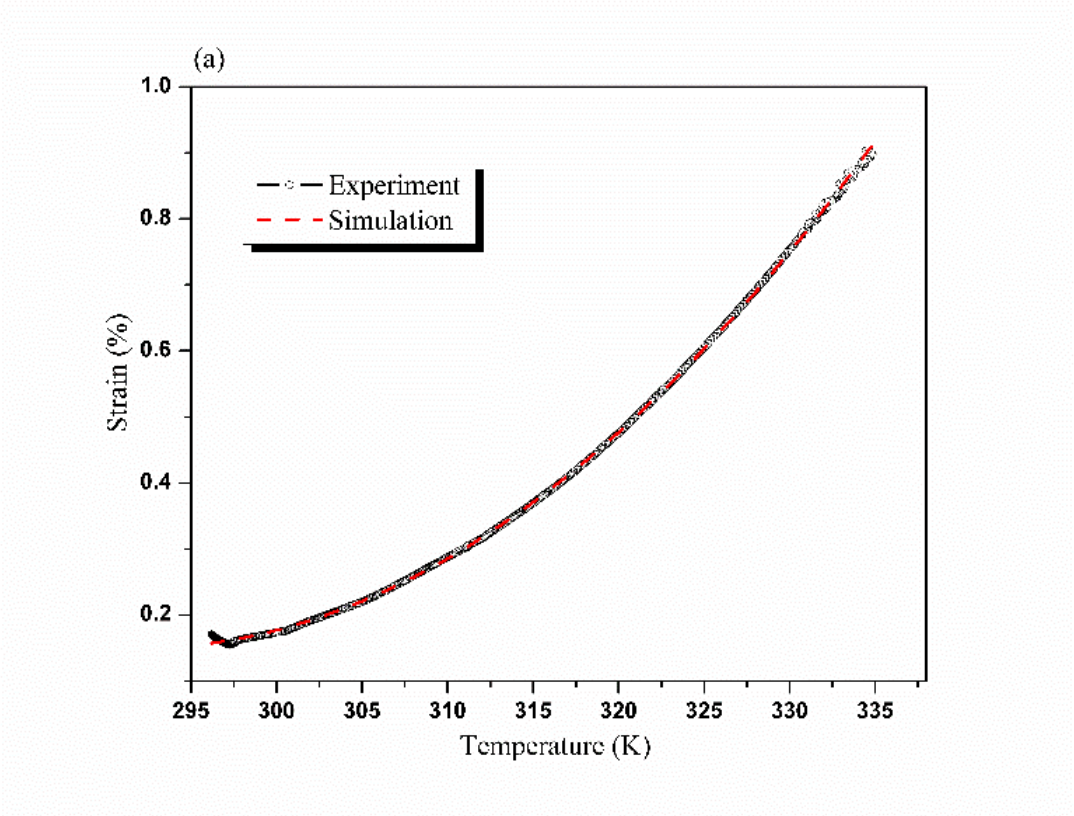

(Figure 3-2 continued)

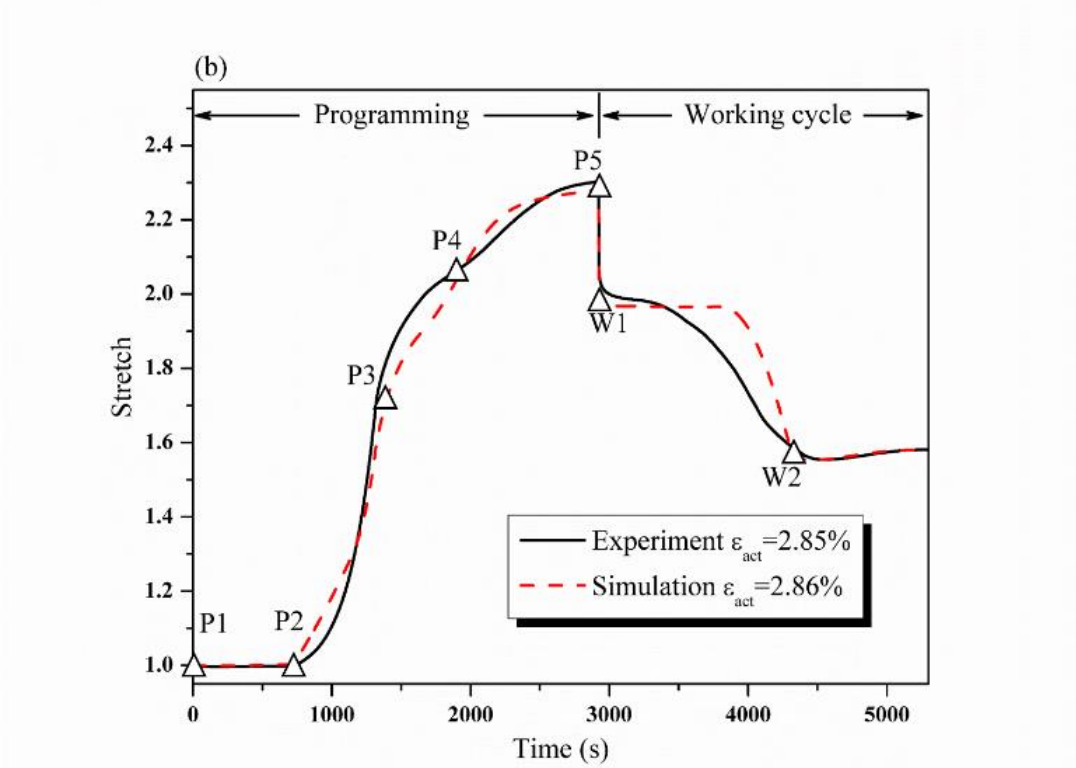

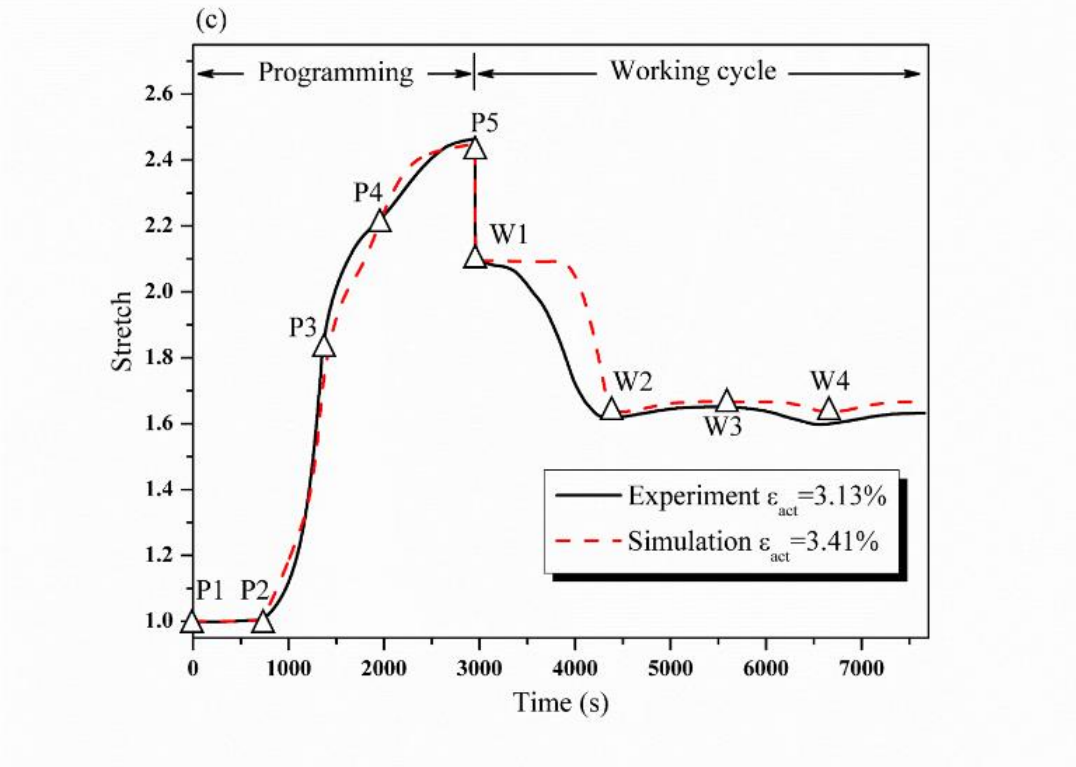

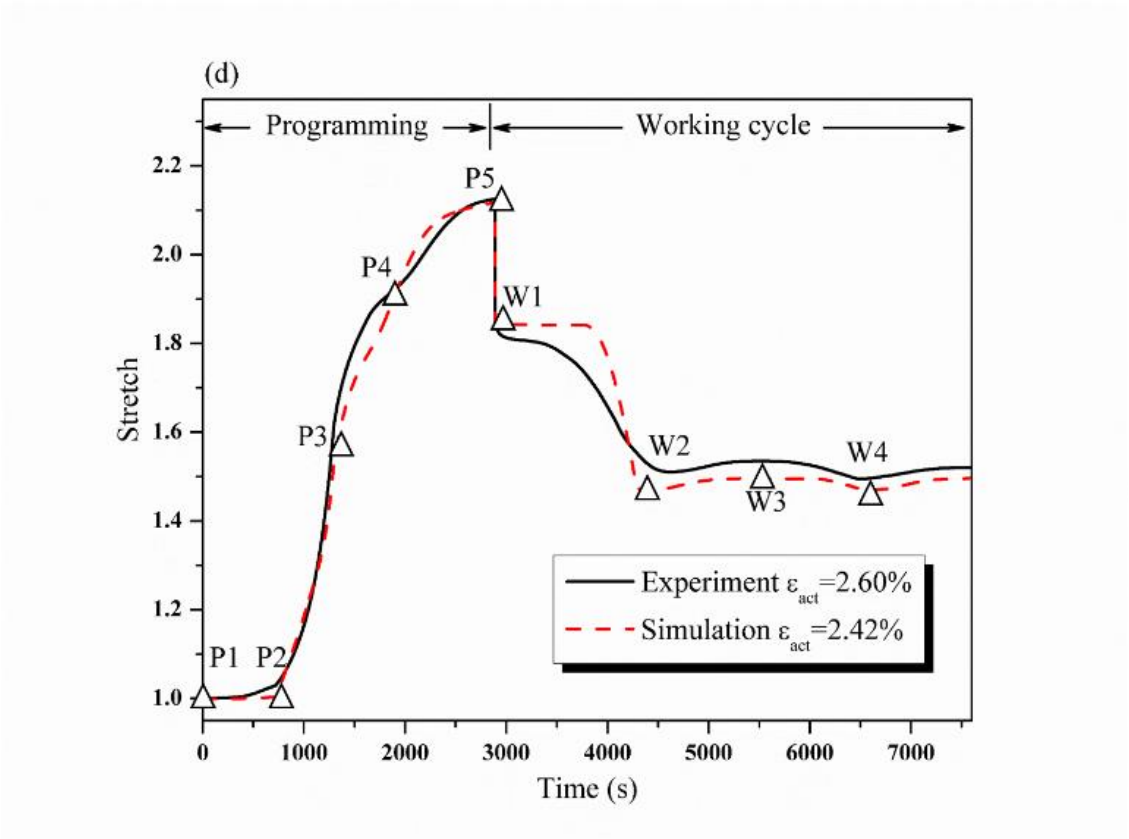

Figure 3-3 Model fits to the experimental results for (a) thermal strain in terms of temperature and (b) the complete programming-working cycle with $1MPa$ programming stress. Model validation for the complete programming-working cycle for the cases of (c) $1.05MPa$ programming stress, and (d) $0.95MPa$ programming stress. P1 to P5 and the triangle symbols indicate the starting points of 5 consecutive programming steps: heat up to 50℃; load to designated stress (1, 1.05 and $0.95MPa$ for (b), (c) and (d), respectively); hold the sample at the constant stress; cool down to 0℃; and finally remove the load. W1 to W4 and triangle symbols indicate the starting points of working cycle steps: heat up to 40℃ (W1 and W3 are the starts of the heating steps in the first and second working cycle, respectively) and cool down to 0℃ (W2 and W4 are the starts of the cooling steps in the first and second working cycle, respectively) at zero external load, i.e., *true* 2W-SME.

Figure 3-3(b) shows the model fit. The actuation strain ε_{act} is calculated by $(\lambda_f - \lambda_{min})$, where λ_f is the final stretch at the end of the cooling process in the first working cycle and λ_{min} is the minimum stretch within the first working cycle. The model is able to predict the 2.86% actuation strain in the first working cycle, compared with the 2.85% actuation strain demonstrated in the experiment. The reasonable agreement between model simulation and experiment validates that the model captures the essential features demonstrated in the 2W-SME. The model parameters identified by fitting the $1MPa$ programming stress curve were then used to predict the programming-working cycle for $1.05MPa$ and $0.95MPa$ programming stress cases. Figure 3-3(c) and (d) show the comparison between model predictions and experiments. The good agreement between the model predictions and the experiments further verifies the model. It is noted that a stiffer transition behavior can be observed for our model as compared to the test result in step W1, which is the melt process that leads to the classical one-way shape recovery. One of the reasons is

that the cPEVA we used in this work exhibits an anomalous broad melting transition (See Fig. 1B in [55]) which may not be precisely reproduced by the current phase evolution law. Additionally, the programming procedure may also affect the melting transition which has not been considered in this work. As such, in our future work, a more appropriate phase evolution law should be involved in the model to obtain more accurate modeling results.

3.5.3 Mechanism of *true* 2W-SME

As stated above, the *true* 2W-SME in the working cycle is attributed to the internal stress introduced by the programming procedure. This internal stress is able to lead the oriented crystallization and prompt the crystallization kinetics. To clearly see how the internal stress plays a role in 2W-SME, in Fig. 3-4, we plot the overall stretch λ, the internal stress $\bar{\tau}_a$, as well as the crystalline phase volume fraction α_c for the complete programming-working cycle of the sample with $1MPa$ programming stress side by side (black solid lines). In our work, we used the effective shear stress acting on the amorphous phase $\bar{\tau}_a$ to evaluate the internal stress.

During step P1 (heating), the sample begins to melt when the temperature reaches the melting temperature and leaves a crystalline volume faction of only $\alpha_{P1} = 0.1226$ at the end of the step. This part of solids do not take part in the melting and crystallization process in the subsequent programming steps, in other words, their natural configurations will not be changed. Therefore, these solids possess a single natural configuration. Starting from step P2 (loading), the internal stress keeps increasing due to the external load until step P3 (holding). In step P4 (cooling), crystallization takes place right after cooling process begins, which indicates a significant shift of melting temperature to a higher value due to the internal stress. Meanwhile, the elongation upon cooling (EUC) phenomenon can be observed. Indeed, a portion of the elongation is attributed to the viscoplastic deformation (irreversible component), however, contribution from the deformation in the reversible component is also important. This is evidenced in the fact that the internal stress, which is calculated based on the deformation of the reversible component λ_r (see Section 3.6.1), keeps increasing to a saturated value, although the external stress is maintained constant. At the first sight, it seems contradictory that albeit the effective modulus of the reversible component is increasing during cooling, the deformation increases under a constant external load. Nevertheless, if we take a close look at Eqs. 3-18, during the cooling process, the deformation of the crystalline phase is actually scaled by $1/\lambda_r(t')$, where $\lambda_r(t')$ represents the deformation immediately before crystallization and is free of stress immediately after crystallization. The stress released by this part of crystalline phase causes a stress re-distribution throughout the whole reversible component and gives rise to the further elongation upon cooling. After the external load is removed (step P5 unloading), the sample springs back a little and an $\bar{\tau}_{P5} = 0.3572MPa$ internal stress has been successfully stored in the system. At the end of step W1 (heating), the sample is partially melt, there is still a $\bar{\tau}_{W1} = 0.0835MPa$ residual stress left in the system that will lead to the elongation upon cooling without an external stress imposed on it in the following step W2 (cooling), *i.e.*, the *true* 2W-SME. As can be seen from the modeling results, the internal stress is very stable in the following working cycle (W3 and W4) and this leads to stable and repeatable performance in actuation.

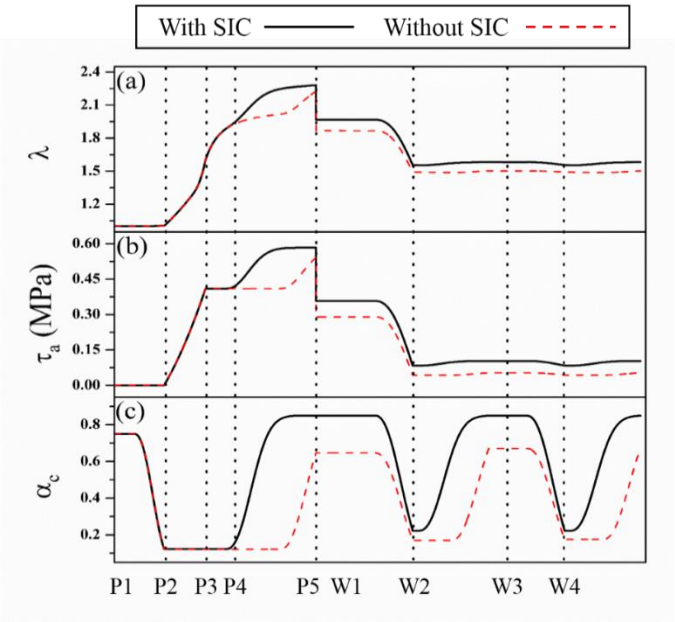

Property	With SIC	Without SIC
$\varepsilon_{W2}(\%)$	2.86	1.59
$\varepsilon_{W4}(\%)$	2.84	1.55
$\bar{\tau}_{P5}(MPa)$	0.3572	0.2895
$\bar{\tau}_{W1}(MPa)$	0.0835	0.0437
$\bar{\tau}_{W3}(MPa)$	0.0835	0.0438
α_{W2}	0.8489	0.6706
α_{W4}	0.8489	0.6723

Figure 3-4 Real-time monitoring of the internal variables evolution. (a) Overall stretch λ. (b) Internal stress (effective shear stress on amorphous phase) $\bar{\tau}_a$. (c) Crystalline volume fraction α_c. (Black solid lines: with SIC effect. Red dash lines: without SIC effect.) Inset table on the right: comparison of various properties between cases with and without SIC effect (ε_{act}: actuation strain. $\bar{\tau}_{P5}$: internal stress after programming. $\bar{\tau}_{W1}$and $\bar{\tau}_{W3}$: internal stress after heating during working cycle. α_{W2} and α_{W4}: crystalline volume fraction after cooling during working cycle).

To further prove the stress induced crystallization (SIC) effect on the crystallization kinetics and eventually on 2W-SME, we eliminated the temperature shift term (Eq. 3-15) in our model and the corresponding modeling results for the stretch λ, the internal stress $\bar{\tau}_a$, and the crystalline phase volume fraction α_c are presented in Fig. 3-4 (red dash lines). As can be seen from Fig. 3-4(c) and the table on the right, without the SIC effect, the crystallization process is significantly delayed, which ends up with lower crystalline volume fraction, lower stored internal stresses and eventually lower strain actuation during step W2.

To investigate the programming stress on the 2W-SME, we summarized the calculated actuation strains ε_{act}, the internal stresses after programming $\bar{\tau}_{P5}$ and the crystalline volume fractions after the first working cycle α_{W2} for three different programming stress (T_{P2}) cases in Table 3-2. Similar to previous studies, programming stress can enhance the 2W-SME. The reason for this is that higher programming stress results in higher internal stress, thus can enhance the crystallization process and eventually improves the 2W-SME.

Table 3-2 Comparison of different programming stress cases.

$T_{P2}(MPa)$	$\varepsilon_{act}(\%)$	$\bar{\tau}_{P5}(MPa)$	α_{W2}
0.95	2.42	0.3377	0.8422
1	2.86	0.3572	0.8489
1.05	3.41	03767	0.8491

3.5.4 Advanced two-way shape memory effect

Based on our analysis and modeling results above, we have reason to believe that the programmed sample should be able to exhibit 2W-SME even when the external load is compressive during the working cycle, as long as the internal stress introduced by the programming procedure is not completely consumed by the external compressive force. Since the reversible component is the only part that is responsible for the stress storage and 2W-SME, we only focus on the deformation under compression in this part. According to our model, the EUC phenomenon can be observed up to $-0.35MPa$ working stress case (Fig. 3-5). If we could seek a shape memory polymer that does not exhibit dramatic viscoplastic deformation and stores a sufficient amount of internal tensile stress, it can be made into an *advanced* 2W-SMP that can generate actuation even under compression.

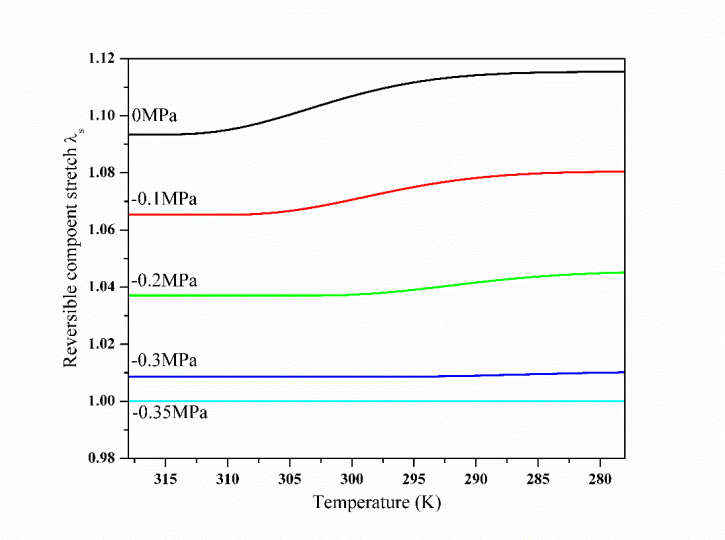

Figure 3-5 Demonstration of "*advanced* 2W-SME": reversible component stretch in the working cycle under different compressive stresses.

3.5 Conclusion

In this work, a 3D constitutive model has been developed based on the multiple natural configurations framework for the *true* 2W-SME. The model has been validated against the experimental results for the cPEVA based 2W-SMP and shown good agreement. The model proves that the internal stress is stored during the programming procedure. This internal stress contributes to 2W-SME from two aspects. First, anisotropy can be introduced to crystalline phases formed during crystallization process and second, crystallization kinetics in polymer can be greatly enhanced by deformation. Higher programming stress can lead to higher stored internal stress and ends up with better true 2W-SME performance. We predict that if a SMP does not exhibit dramatic viscoplastic deformation and can stores a sufficient amount of internal tensile stress, it can be made into an *advanced* 2W-SMP that can generate actuation even under compression.

CHAPTER 4 A TOP-DOWN MULTI-SCALE MODELING FOR ACTUATION RESPONSE OF POLYMERIC ARTIFICIAL MUSCLES

In the present work, we established a multi-scale modeling framework for the thermomechanical actuation responses of the twisted-then-coiled polymeric artificial muscles by a top-down strategy, spanning from macro-scale helical spring analysis down to molecular level chain interaction study. Comparison between modeling results and experimental results exhibited excellent agreement. The effect of the micro-, meso- and macro-scale parameters on the actuation responses of the artificial muscle was further discussed through a parametric study per the validated model. This work helps understand the physical origin behind the remarkable tensile actuation behavior of the twisted-then-coiled polymeric artificial muscles and also provides inspirations for optimal design of advanced artificial muscles made by twist-insertion procedure.

4.1 Introduction

Several studies have been conducted to explain the extraordinary thermomechanical behavior of twisted-then-coiled polymeric muscles, which facilitate future design. In recognition of the similarities between the maximum specific work during torsional actuation for a non-coiled twisted fiber and that during tensile contraction for a twisted-then-coiled spring, Haines et al. [82] pointed out that the large-stroke tensile actuation of the coiled spring arises from the torsional actuation of the twisted polymer fiber. In addition, the authors used a rough analysis and proved that the thermally triggered torsional actuation for the twisted fiber was attributed to both the contraction in axial direction and expansion in transverse direction of the precursor fiber. In addition, the relation between the coil length and the fiber twists per unit length was established from purely kinematic point of view using Love equation [213] and Van Der Heijdgen and Thompson theory [214]. Most recently, Sharafi and Li [215] developed a physics-based constitutive framework, in which the actuation response of the twisted-then-coiled spring was considered to be determined by two types of as-trained molecules, that is, helical chains and entropic chains. However, the involvement of a large number of molecular scale parameters in the constitutive framework, which are difficult to determine, makes the use of the molecular scale model of considerable challenge. Therefore, they also proposed a computationally efficient phenomenological thermomechanical constitutive model, which was largely dependent on curve fittings. Because of this, the phenomenological model is unable to pin down the underlying mechanisms controlling the muscle actuation behavior.

In summary, there is still a lack of theoretical models to elucidate the physical origin behind the remarkable tensile actuation behavior and, therefore, the correlation between the actuation performance and the intrinsic material parameters remains unclear. In the present paper, we will analyze the actuation response from macro-scale helical spring top-down to the molecular chain interaction. We will build a multi-scale modeling framework, in order to reproduce and predict the actuation behavior and evaluate the impact of various factors on the response of polymeric artificial muscles. This paper is arranged as follows. Section 4.1 introduces the background and motivations for this study. In Section 4.2, a general top-down analysis is given. This is followed by the development of a multi-scale modeling framework in Section 4.3. The model validation and

parametric study are conducted in Section 4.4. In Section 4.5, the important results and findings are summarized.

4.2 Top-down Analysis

This twisted-then-coiled artificial muscle contains hierarchical structures and it is schematically illustrated in Fig. 4-1.

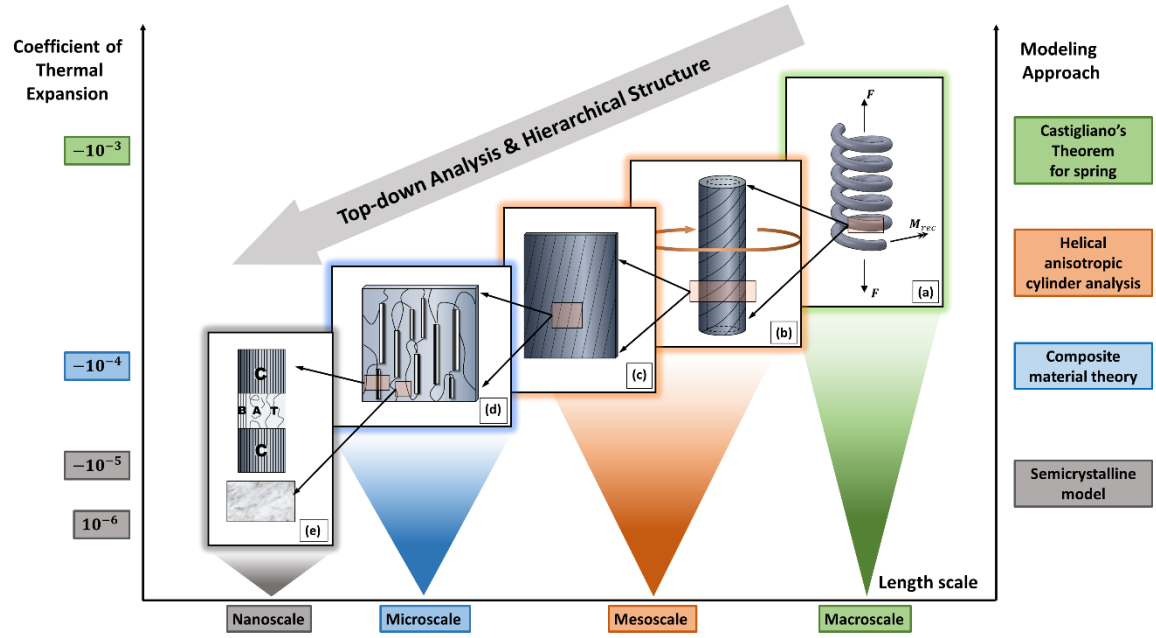

Figure 4-1 Multi-scale modeling framework: (a) Twisted then coiled spring. (b) A section of the twisted fiber. (c) Off-axis laminate, hypothetically cut and separated from the twisted fiber. (d) On-axis lamina, consisting of discontinuous aligned micro-fibrils embedded into amorphous matrix. (e) Top: crystal blocks connected in series with inter-crystalline materials. Bottom: amorphous matrix made of rubbery and glassy phases.

The coiled muscles (Fig. 4-1(a)) are able to reversibly delivery over 20% contraction upon heating and lift heavy load [216], which is an abnormal behavior that cannot be explained by the classical spring mechanism. More specifically, Eq. (4-1) is the classical relation of the axial applied load F and the displacement δ of the spring, in terms of the properties of the fiber (shear modulus G_f and diameter d_f) and geometries of the coil (mean diameter $\overline{D_c}$ and number of active coils n) [217]:

$$F = \frac{G_f d_f^4}{8\overline{D_c}^3 n}\delta \tag{4-1}$$

Based on Eq. (4-1), since the shear modulus drops as temperature increases, the coil will elongate, instead of contracting upon heating. The essential reason behind this contradiction is the twisted configuration of the fiber, as shown in Fig. 4-1(b). This highly twisted structure exhibits large torsional actuation when heated and hence generates large twisting moment when tethered at both ends. Intuitively, in a coil made of this twisted fiber, the released torque can screw the coil

segments, compete with the external applied load and eventually result in the contraction of the coil.

As suggested by Haines et al. [82], the torsional actuation is mostly attributed to both the thermal contraction in the axial direction and thermal expansion in the radial direction of the precursor fiber, which are both at least an order of magnitude smaller than that of the coiled spring (See the coefficients of thermal expansion presented in Fig. 4-1 on the left). In order to reproduce the torsional behavior of the twisted fiber, the thermomechanical properties of the twisted fiber are necessary. For an anisotropic polymer fiber, studies have shown that twisting has a significant impact on the thermomechanical properties of fibers or yarns [218-220] and a number of models have been developed to elucidate this dependence [221-224]. A commonly used approach is decomposing the twisted fiber into concentric hollow cylinders, and then each hollow cylinder is hypothetically cut and opened up into a layered structure as shown in Fig. 4-1(c). Considering the fact that most of the polymeric fibers used to make artificial muscles are semi-crystalline consisting of aligned micro-fibrils, each layer of the twisted fiber contains collimated micro-fibrils, whose orientation is determined by the position of the layer from the cylinder center axis, namely, the outermost layer has the most oriented fibrils and the innermost layer has no orientation. This configuration is very much analogous to the fiber-reinforced composite. As such, the thermomechanical properties of the off-axis laminate (Fig. 4-1(c)) and the assembly of the lamina with different angles (Fig. 4-1(b)), i.e. the twisted fiber, can be obtained once the properties of the on-axis lamina (Fig. 4-1(d)) are given based on composite material theory, together with three dimensional helical anisotropic cylinder analysis.

The analyses of the on-axis lamina properties are case dependent. Most commonly used precursor fibers are semi-crystalline fibers, such as Polyethylene and Nylon 6. In our current study, we focus on artificial muscle made of Polyethylene (PE) copolymer monofilament under the brand name of ZEBCO OMNIFLEX30LBA, due to its convenient availability. A closer observation by previous researchers [225-228] reveals that in a highly oriented Polyethylene fiber, the crystalline would form needlelike, discontinuous micro-fibrils with the long axis in the fibrils direction, and are embedded into an amorphous matrix phase (See Fig. 4-1(d)). The amorphous matrix (Bottom inset of Fig. 4-1(e)), of which the coefficient of thermal expansion (CTE) is positive (See Fig. 4-1 on the left for the CTE of the amorphous matrix), can always be regarded as a mixture of glassy phase and rubbery phase with temperature dependent volume fractions. As for the micro-fibrils (Top inset of Fig. 4-1(e)), they have been described as crystal blocks with negative CTE of the order of $-10^{-5}K^{-1}$ (denoted as part **C** in the upper inset of Fig. 4-1(e)), periodically connected in series with inter-crystalline materials, which may consist of a parallel combination of inter-crystalline bridges (denoted as part **B** in the upper inset of Fig. 4-1(e)), amorphous chains (denoted as part **A** in the upper inset of Fig. 4-1(e)), and tie molecules (denoted as part **T** in the upper inset of Fig. 4-1(e)) [229, 230].

In summary, we divided the multi-scale modeling within the continuum mechanics framework into four levels: (1) *Macro-scale model*: In this length scale, we focus on the relation between the applied load and the displacement of the spring. The polymeric fiber, of which the coiled spring is made, has a diameter of ~$1mm$, and possesses no discernable microstructural features, i.e., it is completely homogenized. (2) *Meso-scale model*: At this length scale, the twisted fiber is treated as a discretely stacked laminate, while the material within each lamina is assumed to be

homogenized and transversely isotropic. This assumption requires an appropriate thickness for the lamina. Firstly, the thickness should be small enough, so that the twisting orientation angle (θ_f) distribution within each layer is not too broad and using one averaged orientation angle to represent the corresponding ply is acceptable. Meanwhile, the thickness should also be large enough, in order to include sufficient amount of micro-fibrils within its cross-section. The crystalline micro-fibrils from the micro-scale perspective are orthotropic materials. Therefore, only when there are enough micro-fibrils in the cross-section, can we apply the homogenized and transversely isotropic assumptions to each lamina. For the polyethylene fiber we are studying, previous study has reported that the intrinsic length scale for the thickness of the micro-fibrils are of the order of $15nm$ and $\sim 200nm$ for the length [227]. Therefore, we believe that a lamina thickness of the order of ~1μm is an appropriate choice for our discretized meso-scale modeling. (3) *Micro-scale model*: In this case, the micro-structure of each lamina is taken into account. Classical continuum elasticity based on homogenization may fail at this scale due to the size effect [231]. Maranganti and Sharma [231] demonstrated that the characteristic length scale at which the size effect come into play for polymer systems ranges from $30nm$ to $150nm$, which is comparable to the intrinsic length scale reported for the crystalline micro-fibrils in the polyethylene fiber. Within the micromechanics framework, we thus treat each lamina as a two-phase composite consisting of discontinuous crystalline micro-fibrils embedded into the amorphous matrix. The two constituents are considered to be featureless in the current length scale. A parameter will be used to account for the imperfect interfacial interaction between the two constituent. (4) *Nano-scale model*: The fine structures of each component (crystalline micro-fibrils and amorphous matrix) in micro-scale model are further considered. The material at this length scale may contain a variety of topological defects and chemical impurities which may significantly alter its properties. Polyethylene, as one of the commonly used polymer, has been extensively studied. Therefore, we will directly utilize the results from existing literatures and provide inputs for the micro-scale model.

Notice that, starting from the crystal blocks, which are bridged by the twisted semi-crystalline fiber and finally to the coiled spring, the thermal contractions are magnified progressively based on different mechanisms. In the next section, we will build up a multi-scale modeling framework for each step of the foregoing analyses.

4.3 Multi-scale Modeling Framework

4.3.1 Macro-scale modeling for the twisted-then-coiled spring

Previous study [82] has suggested that the remarkable tensile actuation behavior is driven by the giant torsional actuation generated by the twisted fiber during heating. We here will quantify this mechanism based on a consistent application of Castigliano's second theorem (CST) [232]. The coordinate systems, which include global Cartesian ($\{\boldsymbol{X_c}, \boldsymbol{Y_c}, \boldsymbol{Z_c}\}$), global cylindrical ($\{\boldsymbol{r_c}, \boldsymbol{\vartheta_c}, \boldsymbol{z_c}\}$), and local cylindrical coordinate ($\{\boldsymbol{r_f}, \boldsymbol{\vartheta_f}, \boldsymbol{z_f}\}$**)**, used to analyze the helical coil, are shown in Fig. 4-2(b). Throughout the working cycle, a constant load $\boldsymbol{F} = F\boldsymbol{Z_c}$ is applied to the coil. In addition, since both ends of the twisted fiber are tethered, the untwisting tendency of the fiber is fully constrained during the working cycle, ending up with a recovered torque in the axial direction along the twisted fiber， $\boldsymbol{M}_{rec} = M_{rec}\boldsymbol{z_f}$. Notice that the direction of the recovered torque is determined by chirality of the twisted-coil: A homo-chiral coil, that is, the chirality of the

fiber twist matches that of the coil, leads to recovered torque in $\boldsymbol{z_f}$ direction, while a hetero-chiral coil results in recovered torque in $-\boldsymbol{z_f}$ direction.

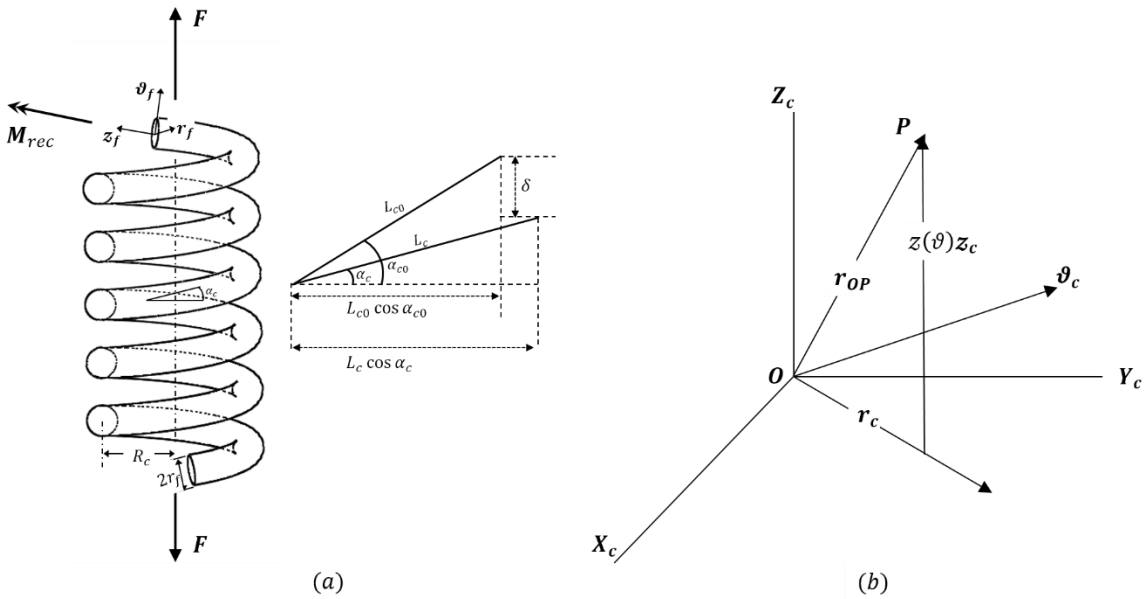

Figure 4-2 (a) Left: Coiled spring loaded with applied force F and recovered torque M_{rec}. Right: Kinematic relationship of the coiled spring. (b) The coordinate systems for the coiled spring that are used in the model. (Definitions of the notations are given in the text.)

For a given applied force $\boldsymbol{F} = F\boldsymbol{Z_c} = F\boldsymbol{z_c}$, by using the relationship between the local and global coordinates:

$$\boldsymbol{r_f} = -\boldsymbol{r_c} \tag{4-2a}$$

$$\boldsymbol{\vartheta_f} = -\sin\alpha_c\,\boldsymbol{\vartheta_c} + \cos\alpha_c\,\boldsymbol{z_c} \tag{4-2b}$$

$$\boldsymbol{z_f} = \cos\alpha_c\,\boldsymbol{\vartheta_c} + \sin\alpha_c\,\boldsymbol{z_c} \tag{4-2c}$$

where $\boldsymbol{r_f}$ is the unit vector in the coil's cross section pointing inward, $\boldsymbol{z_f}$ is the unit vector along the coil's tangent direction, and $\boldsymbol{\vartheta_f}$ is the unit vector in the plane of the fiber's cross section as dictated by the vector product $\boldsymbol{\vartheta_f} = \boldsymbol{z_f} \times \boldsymbol{r_f}$, and α_c is the pitch angle of the coil. The applied force on the slightly inclined, positively directed face at point $\boldsymbol{P}$ can be expressed in terms of the local coordinate:

$$\boldsymbol{F_{app}} = \boldsymbol{F} = F\sin\alpha_c\,\boldsymbol{z_f} + F\cos\alpha_c\,\boldsymbol{\vartheta_f} \tag{4-3}$$

The free body diagram shows that the applied force also results in torsional and bending moment at point $\boldsymbol{P}$:

$$\boldsymbol{M}^F_{app} = \boldsymbol{r}(PO) \times (-\boldsymbol{F}) = -FR\boldsymbol{\vartheta_c} = -FR\cos\alpha_c\,\boldsymbol{z_f} + FR\sin\alpha_c\,\boldsymbol{\vartheta_f} \tag{4-4}$$

The recovery torque, $\boldsymbol{M}_{rec} = M_{rec}\boldsymbol{z_f}$ is considered to be applied on top of $\boldsymbol{M}_{app}^{F}$, thus, the total applied moment at point $\boldsymbol{P}$ is:

$$\boldsymbol{M}_{app} = \boldsymbol{M}_{app}^{F} + \boldsymbol{M}_{rec} = (-FR\cos\alpha_c + M_{rec})\boldsymbol{z_f} + FR\sin\alpha_c\,\boldsymbol{\vartheta_f} \tag{4-5}$$

For convenience, we re-write Eqs. (4-3) and (4-5) as:

$$\boldsymbol{F}_{app} = F_z\boldsymbol{z_f} + F_\vartheta\boldsymbol{\vartheta_f} \tag{4-6a}$$

$$\boldsymbol{M}_{app} = M_z\boldsymbol{z_f} + M_\vartheta\boldsymbol{\vartheta_f} \tag{4-6b}$$

with the normal force $F_z = F\sin\alpha_c$, shear force $F_\vartheta = F\cos\alpha_c$, torsional moment $M_z = -FR\cos\alpha_c + M_{rec}$ and bending moment $M_\vartheta = FR\sin\alpha_c$. These components are constant along the coil. By assuming that, at each step of temperature increment, the deformations along the fiber caused by the external load are infinitesimal, the complementary energy can be expressed as [233]:

$$\begin{aligned} U^* &= \int_0^{L_c}\left(\frac{M_z^2}{2\bar{G}J} + \frac{M_\vartheta^2}{2\bar{E}I} + \frac{F_z^2}{2\bar{E}A} + \frac{F_\vartheta^2}{2\bar{G}A}\right)dl \\ &= L_c\left(\frac{M_z^2}{2\bar{G}J} + \frac{M_\vartheta^2}{2\bar{E}I} + \frac{F_z^2}{2\bar{E}A} + \frac{F_\vartheta^2}{2\bar{G}A}\right) \\ &= \frac{1}{2}\,f_{11}F^2 - 2f_{12}FM_{rec} + \frac{1}{2}f_{22}M_{rec}^2 \end{aligned} \tag{4-7}$$

where $\bar{E}$ and $\bar{G}$ are the effective moduli of the twisted fiber and

$$f_{11} = \frac{1}{2}L_c\left(\frac{1}{\bar{G}J}R^2\cos^2\alpha_c + \frac{1}{\bar{E}I}R^2\sin^2\alpha_c + \frac{1}{\bar{G}A}\cos^2\alpha_c + \frac{1}{\bar{E}A}\sin^2\alpha_c\right) \tag{4-8a}$$

$$f_{12} = L_c\frac{R\cos\alpha_c}{2\bar{G}J} \tag{4-8b}$$

$$f_{22} = L_c\frac{1}{\bar{G}J} \tag{4-8c}$$

Taking the cross-section area of the fiber $A = \frac{\pi d^2}{4}$, the second moment $I = \frac{\pi d^4}{64}$, the polar moment of that area $J = \frac{\pi d^4}{32}$ and the radius of the coil $R = \frac{D}{2} = \frac{L_c\cos\alpha_c}{n\pi}$, Eq. 4-8 becomes:

$$\begin{aligned} f_{11} = {} & \frac{8n}{\pi^3 d^4}\left(\frac{L_c}{n}\right)^3\frac{\cos^4\alpha_c}{\bar{G}} + \frac{8n}{\pi d^2}\left(\frac{L_c}{n}\right)\frac{\cos^2\alpha_c}{2\bar{G}} \\ & + \frac{8n}{\pi^3 d^4}\left(\frac{L_c}{n}\right)^3\frac{2\sin^2\alpha_c\cos^2\alpha_c}{\bar{E}} + \frac{8n}{\pi d^2}\left(\frac{L_c}{n}\right)\frac{\sin^2\alpha_c}{2\bar{E}} \end{aligned} \tag{4-9a}$$

$$f_{12} = \frac{8n}{\pi^2 d^4}\left(\frac{L_c}{n}\right)^2 \frac{\cos^2 \alpha_c}{\bar{G}} \tag{4-9b}$$

$$f_{22} = \frac{32}{\pi d^4}\frac{L_c}{\bar{G}} \tag{4-9c}$$

Then, the displacement δ of a helical spring is directly found by applying CST [234]:

$$\delta = f_{11}F - f_{12}M_{rec} \tag{4-10}$$

The displacement can also be expressed as a function of the pitch angle α_c using the kinematic relationship:

$$\delta = L_c \sin \alpha_c - L_{c0} \sin \alpha_{c0} \tag{4-11}$$

where L_{c0} and α_{c0} are the initial length of the fiber and the initial pitch angle of the coil (after loading), respectively. Using Eqs. (4-10) and (4-11), the pitch angle $\alpha_c(T)$, hence the displacement $\delta(T)$ can be expressed in terms of $d, L_c, \bar{G}, \bar{E}, M_{rec}, etc.$, on which temperature dependences will be determined using the meso-scale modeling described in the following section.

4.3.2 Meso-scale modeling for the thermomechanical behavior of the twisted fiber

- **Concentric helically anisotropic laminate**

As stated in Section 4.2, the twisted fiber is decomposed into concentric hollow cylinders, and then hypothetically cut and separated into a lamina containing collimated micro-fibrils (See Fig. 4-3).

To avoid confusion and complexity, we first clarify the symbols and notations. Referring to Fig. 4-3, the principal material axes are labeled as **1** and **2**, where **1**-axis is parallel to the micro-fibrils and **2**-axis is normal to them; $\boldsymbol{\vartheta_f}$ and $\boldsymbol{z_f}$ are principal terms of the off-axis behavior. According to the definition in classical lamination theory and the handedness of the coordinate, the off-axis angle θ_f is depicted in Fig. 4-3.

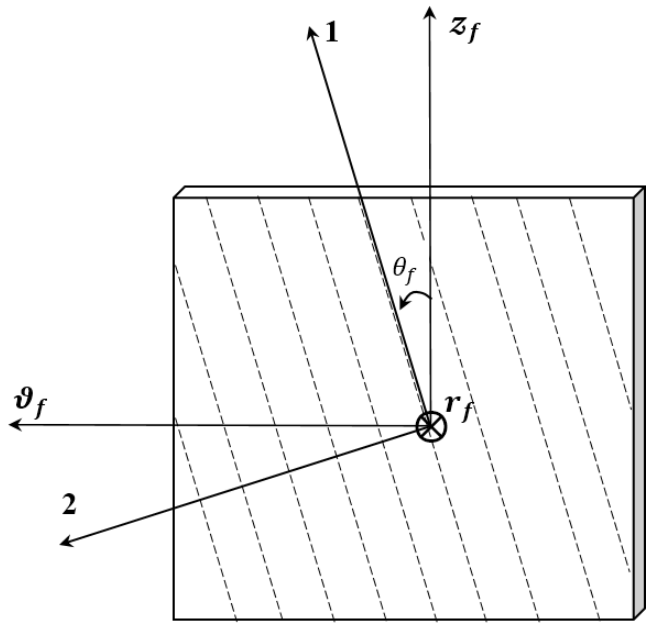

Figure 4-3 Opened-up structure of the micro-fibrils reinforced composite lamina.

Once we have obtained the on-axis transverse symmetric thermomechanical properties, i.e. the stiffness matrix $\boldsymbol{C}$ and the coefficients of thermal expansion $\alpha's$, which will be determined in the next section, we are able to evaluate the off-axis laminate using Eqs. (4-12) and (4-13).

$$\begin{cases} \bar{C}_{11} = C_{11}m^4 + 2(C_{12} + C_{16})m^2n^2 + C_{22}n^4 \\ \bar{C}_{12} = (C_{11} + C_{22} - 4C_{66})m^2n^2 + C_{12}(m^4 + n^4) \\ \bar{C}_{13} = C_{13}m^2 + C_{23}n^2 \\ \bar{C}_{16} = -C_{22}mn^3 + C_{11}m^3n - (C_{12} + 2C_{66})mn(m^2 - n^2) \\ \bar{C}_{22} = C_{11}n^4 + 2(C_{12} + 2C_{66})m^2n^2 + C_{22}m^4 \\ \bar{C}_{23} = C_{13}n^2 + C_{23}m^2 \\ \bar{C}_{26} = -C_{22}m^3n + C_{11}mn^3 + (C_{12} + 2C_{66})mn(m^2 - n^2) \\ \bar{C}_{33} = C_{33} \\ \bar{C}_{36} = (C_{13} - C_{23})mn \\ \bar{C}_{66} = (C_{11} + C_{22} - 2C_{12})m^2n^2 + C_{66}(m^2 - n^2)^2 \end{cases} \tag{4-12}$$

and

$$\begin{cases} \bar{\alpha}_z = \alpha_1 m^2 + \alpha_2 n^2 \\ \bar{\alpha}_\theta = \alpha_1 n^2 + \alpha_2 m^2 \\ \bar{\alpha}_r = \alpha_3 = \alpha_2 \\ \bar{\alpha}_{z\theta} = 2(\alpha_1 - \alpha_2)mn \end{cases} \tag{4-13}$$

where $m = \cos\theta_f$, and $n = \sin\theta_f$. Notice that the appearance of a coupling term $\alpha_{z\theta}$ in Eq. (4-13), indicates that a reversible thermal shear strain will be generated during heating or cooling. In other words, the torsional behavior of the twisted fiber can be explained intuitively from the composite material point of view.

To obtain displacements $\{u, v, w\}$ and stress components $\{\sigma_z, \sigma_\theta, \sigma_r, \sigma_{z\theta}\}$ for each layer we assume that radial deformation and shearing twist are axisymmetric, and axial extension is uniform across the cross-section, the displacements are thus shown to be functions of the radial and axial coordinates (See Fig. 4-4):

$$u = u(r) \qquad v = v_0 rz \qquad w = w_0 z \tag{4-14}$$

The corresponding strain components are:

$$\varepsilon_r = \frac{du}{dr} \qquad \varepsilon_\theta = \frac{u}{r} \qquad \varepsilon_z = w_0 \qquad \varepsilon_{z\theta} = v_0 r \qquad \varepsilon_{r\theta} = \varepsilon_{rz} = 0 \tag{4-15}$$

By assuming infinitesimal deformation of the material, the constitutive relation for a material with helical anisotropy for the four non-zero stress and strain components is:

$$\begin{bmatrix} \sigma_z \\ \sigma_\theta \\ \sigma_r \\ \sigma_{z\theta} \end{bmatrix} = \begin{bmatrix} \bar{C}_{11} & \bar{C}_{12} & \bar{C}_{13} & \bar{C}_{16} \\ \bar{C}_{12} & \bar{C}_{22} & \bar{C}_{23} & \bar{C}_{26} \\ \bar{C}_{13} & \bar{C}_{23} & \bar{C}_{33} & \bar{C}_{36} \\ \bar{C}_{16} & \bar{C}_{26} & \bar{C}_{36} & \bar{C}_{66} \end{bmatrix} \begin{bmatrix} \varepsilon_z - \alpha_z \Delta T \\ \varepsilon_\theta - \alpha_\theta \Delta T \\ \varepsilon_r - \alpha_r \Delta T \\ \varepsilon_{z\theta} - \alpha_{z\theta} \Delta T \end{bmatrix} \tag{4-16}$$

The equilibrium equation that needs to be satisfied is:

$$\frac{d\sigma_r}{dr} + \frac{\sigma_r - \sigma_\theta}{r} = 0 \tag{4-17}$$

Substituting Eqs. (4-14), (4-15) and (4-16) into the governing equation (4-17) leads to the radial displacement u. Without going to further derivation details, we here present the solution for u:

$$\begin{aligned} u = {} & C_1 r^\mu + C_2 r^{-\mu} + \frac{(\bar{C}_{26} - 2\bar{C}_{36})}{(4\bar{C}_{33} - \bar{C}_{22})} v_0 r^2 \\ & + \frac{(\bar{C}_{12} - \bar{C}_{13})}{(\bar{C}_{33} - \bar{C}_{22})} w_0 r + \frac{(\bar{C}_{13} - \bar{C}_{12})}{(\bar{C}_{33} - \bar{C}_{22})} \alpha_z \Delta T r + \frac{(\bar{C}_{23} - \bar{C}_{22})}{(\bar{C}_{33} - \bar{C}_{22})} \alpha_\theta \Delta T r \\ & + \frac{(\bar{C}_{33} - \bar{C}_{23})}{(\bar{C}_{33} - \bar{C}_{22})} \alpha_r \Delta T r + \frac{(\bar{C}_{36} - \bar{C}_{26})}{(\bar{C}_{33} - \bar{C}_{22})} \alpha_{z\theta} \Delta T r \end{aligned} \tag{4-18}$$

where $\mu = \sqrt{\frac{\bar{C}_{22}}{\bar{C}_{33}}}$, and the undetermined coefficients C_1 and C_2 will be determined by the continuity and boundary conditions as shown in the next section. The stress components can then be obtained by taking Eq. (4-18) back into Eqs. (4-14), (4-15) and (4-16):

$$\begin{aligned} \sigma_z = {} & C_1 r^{\mu-1} (\bar{C}_{12} + \mu \bar{C}_{13}) + C_2 r^{-\mu-1} (\bar{C}_{12} - \mu \bar{C}_{13}) \\ & + w_0 \left[\bar{C}_{11} + \frac{(\bar{C}_{12} + \bar{C}_{13})(\bar{C}_{12} - \bar{C}_{13})}{(\bar{C}_{33} - \bar{C}_{22})} \right] \end{aligned}$$

$$+v_0 r\left[\bar{C}_{16}+\frac{(\bar{C}_{12}+2\bar{C}_{13})(\bar{C}_{26}-2\bar{C}_{36})}{(4\bar{C}_{33}-\bar{C}_{22})}\right]$$
$$+\alpha_z \Delta T\left[-\bar{C}_{11}+\frac{(\bar{C}_{12}+\bar{C}_{13})(\bar{C}_{13}-\bar{C}_{12})}{(\bar{C}_{33}-\bar{C}_{22})}\right]$$
$$+\alpha_\theta \Delta T\left[-\bar{C}_{12}+\frac{(\bar{C}_{12}+\bar{C}_{13})(\bar{C}_{23}-\bar{C}_{22})}{(\bar{C}_{33}-\bar{C}_{22})}\right]$$
$$+\alpha_r \Delta T\left[-\bar{C}_{13}+\frac{(\bar{C}_{12}+\bar{C}_{13})(\bar{C}_{33}-\bar{C}_{23})}{(\bar{C}_{33}-\bar{C}_{22})}\right]$$
$$+\alpha_{z\theta} \Delta T\left[-\bar{C}_{16}+\frac{(\bar{C}_{12}+\bar{C}_{13})(\bar{C}_{36}-\bar{C}_{26})}{(\bar{C}_{33}-\bar{C}_{22})}\right] \quad \text{(4-19a)}$$

$$\sigma_\theta = C_1 r^{\mu-1}(\bar{C}_{22}+\mu\bar{C}_{23})+C_2 r^{-\mu-1}(\bar{C}_{22}-\mu\bar{C}_{23})$$
$$+w_0\left[\bar{C}_{12}+\frac{(\bar{C}_{22}+\bar{C}_{23})(\bar{C}_{12}-\bar{C}_{13})}{(\bar{C}_{33}-\bar{C}_{22})}\right]$$
$$+v_0 r\left[\bar{C}_{26}+\frac{(\bar{C}_{22}+2\bar{C}_{23})(\bar{C}_{26}-2\bar{C}_{36})}{(4\bar{C}_{33}-\bar{C}_{22})}\right]$$
$$+\alpha_z \Delta T\left[-\bar{C}_{12}+\frac{(\bar{C}_{22}+\bar{C}_{23})(\bar{C}_{13}-\bar{C}_{12})}{(\bar{C}_{33}-\bar{C}_{22})}\right]$$
$$+\alpha_\theta \Delta T\left[-\bar{C}_{22}+\frac{(\bar{C}_{22}+\bar{C}_{23})(\bar{C}_{23}-\bar{C}_{22})}{(\bar{C}_{33}-\bar{C}_{22})}\right]$$
$$+\alpha_r \Delta T\left[-\bar{C}_{23}+\frac{(\bar{C}_{22}+\bar{C}_{23})(\bar{C}_{33}-\bar{C}_{23})}{(\bar{C}_{33}-\bar{C}_{22})}\right]$$
$$+\alpha_{z\theta} \Delta T\left[-\bar{C}_{26}+\frac{(\bar{C}_{22}+\bar{C}_{23})(\bar{C}_{36}-\bar{C}_{26})}{(\bar{C}_{33}-\bar{C}_{22})}\right] \quad \text{(4-19b)}$$

$$\sigma_r = C_1 r^{\mu-1}(\bar{C}_{23}+\mu\bar{C}_{33})+C_2 r^{-\mu-1}(\bar{C}_{23}-\mu\bar{C}_{33})$$
$$+w_0\left[\bar{C}_{13}+\frac{(\bar{C}_{23}+\bar{C}_{33})(\bar{C}_{12}-\bar{C}_{13})}{(\bar{C}_{33}-\bar{C}_{22})}\right]$$
$$+v_0 r\left[\bar{C}_{36}+\frac{(\bar{C}_{23}+2\bar{C}_{33})(\bar{C}_{26}-2\bar{C}_{36})}{(4\bar{C}_{33}-\bar{C}_{22})}\right]$$
$$+\alpha_z \Delta T\left[-\bar{C}_{13}+\frac{(\bar{C}_{23}+\bar{C}_{33})(\bar{C}_{13}-\bar{C}_{12})}{(\bar{C}_{33}-\bar{C}_{22})}\right]$$
$$+\alpha_\theta \Delta T\left[-\bar{C}_{23}+\frac{(\bar{C}_{23}+\bar{C}_{33})(\bar{C}_{23}-\bar{C}_{22})}{(\bar{C}_{33}-\bar{C}_{22})}\right]$$
$$+\alpha_r \Delta T\left[-\bar{C}_{33}+\frac{(\bar{C}_{23}+\bar{C}_{33})(\bar{C}_{33}-\bar{C}_{23})}{(\bar{C}_{33}-\bar{C}_{22})}\right]$$
$$+\alpha_{z\theta} \Delta T\left[-\bar{C}_{36}+\frac{(\bar{C}_{23}+\bar{C}_{33})(\bar{C}_{36}-\bar{C}_{26})}{(\bar{C}_{33}-\bar{C}_{22})}\right] \quad \text{(4-19c)}$$

$$\sigma_{\theta z} = C_1 r^{\mu-1}(\bar{C}_{26} + \mu\bar{C}_{26}) + C_2 r^{-\mu-1}(\bar{C}_{26} - \mu\bar{C}_{26})$$
$$+w_0\left[\bar{C}_{16} + \frac{(\bar{C}_{26} + \bar{C}_{36})(\bar{C}_{12} - \bar{C}_{13})}{(\bar{C}_{33} - \bar{C}_{22})}\right]$$
$$+v_0 r\left[\bar{C}_{66} + \frac{(\bar{C}_{26} + 2\bar{C}_{36})(\bar{C}_{26} - 2\bar{C}_{36})}{(4\bar{C}_{33} - \bar{C}_{22})}\right]$$
$$+\alpha_z \Delta T\left[-\bar{C}_{16} + \frac{(\bar{C}_{26} + \bar{C}_{36})(\bar{C}_{13} - \bar{C}_{12})}{(\bar{C}_{33} - \bar{C}_{22})}\right]$$
$$+\alpha_\theta \Delta T\left[-\bar{C}_{26} + \frac{(\bar{C}_{26} + \bar{C}_{36})(\bar{C}_{23} - \bar{C}_{22})}{(\bar{C}_{33} - \bar{C}_{22})}\right]$$
$$+\alpha_r \Delta T\left[-\bar{C}_{36} + \frac{(\bar{C}_{26} + \bar{C}_{36})(\bar{C}_{33} - \bar{C}_{23})}{(\bar{C}_{33} - \bar{C}_{22})}\right]$$
$$+\alpha_{z\theta} \Delta T\left[-\bar{C}_{66} + \frac{(\bar{C}_{26} + \bar{C}_{36})(\bar{C}_{36} - \bar{C}_{26})}{(\bar{C}_{33} - \bar{C}_{22})}\right] \quad \text{(4-19d)}$$

In the next sub-section, we will assemble all the layers and determine the effective properties for the twisted fiber.

- **Multi-layer analysis**

Suppose the cylinder consists of N layers of hollow cylinders. In order to clarify the position of each layer, we hereafter put a superscript 'k' to each component, for example, σ_z^k, u^k and θ_f^k. The inner most layer has an inner radius of r^0 and outer most layer has an outer radius of r^N (See Fig. 4-4(b)). r^0 is taken to be a number very small, for example $10^{-10}mm$, in order to simulate a solid cylinder and meanwhile to avoid singularity. Then, the outer radius of the k^{th} layer becomes $r^k = r^0 + k\frac{r_f - r^0}{N}$, where $r_f = r^N$, is the radius of the fiber. Also, the tangent of the helix angle is assumed to vary linearly with radial position, reaching its maximum at the outer layer of the cylinder, that is, at the k^{th} layer $\theta_f^k(r) = \arctan\frac{r^k}{r_f}\tan\alpha_f$, where α_f is the helical angle at the surface of the fiber.

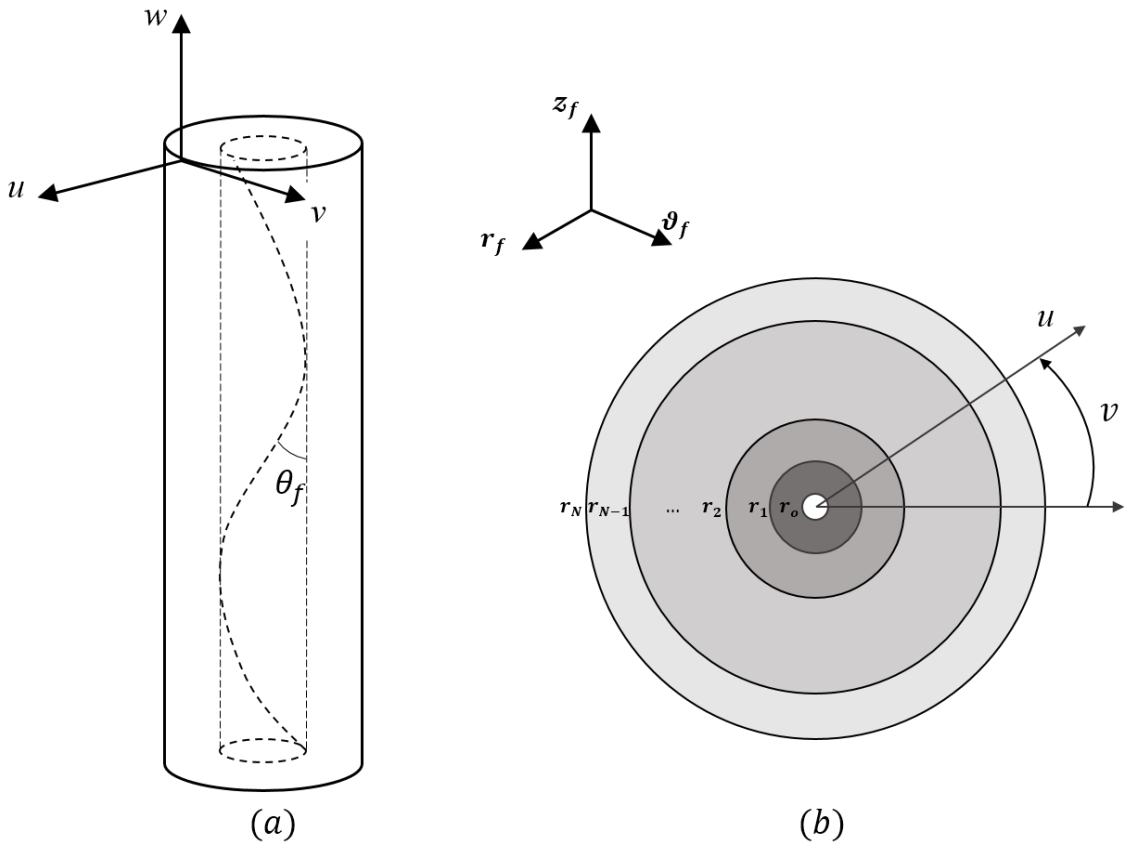

Figure 4-4 Multi-layer analysis

The continuity and boundary conditions then require:

$$\begin{cases} \sigma_r^1(r_0) = 0 \\ \begin{cases} \sigma_r^1(r_1) = \sigma_r^2(r_1) \\ u^1(r_1) = u^2(r_1) \end{cases} \\ \cdots \\ \begin{cases} \sigma_r^{k-1}(r_1) = \sigma_r^k(r_1) \\ u^{k-1}(r_1) = u^k(r_1) \end{cases} \\ \cdots \\ \sigma_r^N(r_N) = 0 \end{cases} \tag{4-20}$$

Using these $2N$ boundary conditions, the $2N$ undetermined coefficients C_1^k and C_2^k (See Section 4.6.1) in each layer can be determined, and hence the stress and strain distributions on the cross section of the twisted fiber can be obtained.

The determination of the effective thermomechanical properties that is needed for the coil analysis, i.e. $\overline{E_z}$, $\overline{G_{z\theta}}$, $\overline{\alpha_z}$, $\overline{\alpha_\theta}$, and $\overline{\alpha_{z\theta}}$, is accomplished by using the method of relaxation that has been described in the work by Pipes and Hubert [222]. Generally speaking, at a certain condition $(v_0, w_0, \Delta T)$, the resultant torque τ and force f can be expressed using the influence coefficients:

$$\begin{bmatrix} A & B \\ C & D \end{bmatrix} \begin{bmatrix} v_0 \\ w_0 \end{bmatrix} = \begin{bmatrix} \tau \\ f \end{bmatrix} \tag{4-21}$$

where,

$$\tau = 2\int_{r^0}^{r_f} \sigma_{\theta z}\, \pi r^2 dr \qquad f = 2\int_{r_0}^{r_f} \sigma_z\, \pi r dr \tag{4-22}$$

and

$$\begin{cases} A = \tau(v_0 = 1, w_0 = 0, \Delta T = 0) \\ B = \tau(v_0 = 0, w_0 = 1, \Delta T = 0) \\ C = f(v_0 = 1, w_0 = 0, \Delta T = 0) \\ D = f(v_0 = 0, w_0 = 1, \Delta T = 0) \end{cases} \tag{4-23}$$

The effective mechanical properties are then straightforward:

$$\begin{cases} \overline{E_z} = \frac{f(v_0 = -\frac{B}{A} w_0, w_0, \Delta T = 0)}{\pi r_f^2 w_0} \\ \overline{G_{z\theta}} = \frac{2\tau(v_0, w_0 = -\frac{C}{D} v_0, \Delta T = 0)}{\pi r_f^4 v_0} \end{cases} \tag{4-24}$$

For the effective thermal expansion, we first set the strain components v_0 and w_0 to be zero, and the thermal torque τ_T and force f_T are determined for a given temperature increment ΔT. Notice that τ_T is the recovered torque increment in the temperature step ΔT, the total recovered torque at a certain temperature is the accumulation of each temperature step:

$$M_{rec} = \int_{T_0}^{T} \tau_T\, dT \tag{4-25}$$

Next, the corresponding thermal strain components are determined using:

$$\begin{bmatrix} A & B \\ C & D \end{bmatrix} \begin{bmatrix} v_{0T} \\ w_{0T} \end{bmatrix} = \begin{bmatrix} -\tau_T \\ -f_T \end{bmatrix} \tag{4-26}$$

Finally,

$$\begin{cases} \overline{\alpha_z} = \frac{w_{0T}}{\Delta T} \\ \overline{\alpha_\theta} = \frac{u_0}{\Delta T} \\ \overline{\alpha_{z\theta}} = \frac{v_0 R}{\Delta T} \end{cases} \tag{4-27}$$

where, $u_0 = u(r_f)$.

4.3.3 Nano- and Micro-scale modeling for the semi-crystalline polyethylene fiber

The microscopic structures for the semi-crystalline polyethylene fiber have been described in Section 4.2 and are depicted in Fig. 4-5. Fig. 4-5(a) presents the phenomenological representation for the aforementioned repeated structure unit in a crystalline micro-fibrils: A crystal block **C** is connected in series with **S** (which is a collective representation of bridges (**b**) and amorphous molecules (**a**)) and tie molecules (**T**). In the following statement, the properties of the crystal block are defined as X^C, likewise, properties of crystalline bridges, amorphous molecules, component **S** and tie molecules are defined as X^b, X^a, X^S, and X^T, respectively. Regarding the micro-fibrils, and the amorphous phase, the properties are designated as X^f and X^m, respectively. (X could be moduli, CTEs, and volume fractions, etc.)

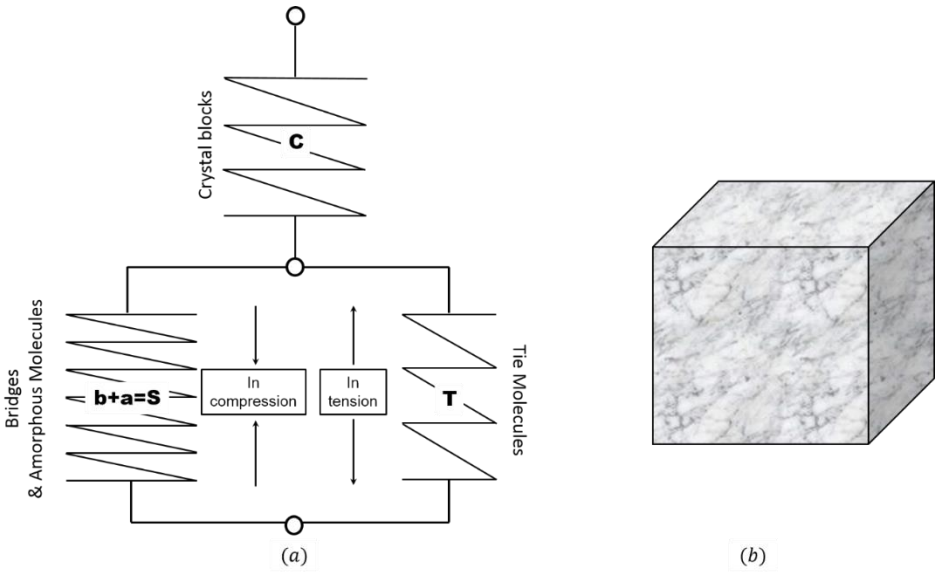

Figure 4-5 Phenomenological representation for (a) crystalline micro-fibrils and (b) amorphous matrix.

For the block crystals, both theoretical calculations [223, 235-239] and experimental measurements [226-228, 240-242] have been performed to evaluate their elastic moduli C_{ij}^c. We here assume that within the working cycle, these elastic moduli are temperature independent. This can be justified by the fact that the melting temperature of the fiber is 220ºC (See Fig. 4-7), which is well above the highest working temperature (80ºC) for the muscle. To account for the weakening effect of the inter-crystalline materials on the mechanical performance of the micro-fibril in the axial direction, we simply introduce a scale factor λ to the modulus in the axial direction and leave the transverse direction almost unchanged:

$$E_1^f = \frac{C_{11}^c}{\lambda} \tag{4-28a}$$

$$E_2^f = \frac{C_{22}^c + C_{33}^c}{2} \tag{4-28b}$$

$$G_{12}^f = C_{66}^c \tag{4-28c}$$

Although the inter-crystalline materials do not show special effect on the mechanical properties, they play decisive roles in amplifying the negative thermal expansion capability of the crystal

blocks. Take polyethylene as an example, it is well known that the coefficient of thermal expansion (CTE) for the crystalline block and bridge is of the order of $-1 \times 10^{-5} K^{-1}$ [243, 244], and is positive for the amorphous domains [245]. However, the whole material may exhibit a CTE of the order of $-1 \times 10^{-4} K^{-1}$(in axial direction) after drawing [229, 230]. Therefore, the large negative CTE of the polymer fiber does not origin from the intrinsic material properties of each components, it is essentially attributed to the "internal strain" between the crystalline bridges and the tie molecules. More specifically, the natural length of the bridge is longer than that of the tie molecule. When they are in parallel, the bridges will be compressed and the tie molecule will be tensioned (See Fig. 4-5(a)). In addition, the tie molecules obey entropic elasticity while the elasticity for the bridge is almost constant. With a suitable volume fraction ratio between the two components, the overall material can exhibit large amount of contraction upon heating. As a matter of fact, this phenomenon is found to be common in essence with the shape memory effect: they are both related to the residual internal strain or stored strain induced by drawing or programming process. In Choy et al. [230], the authors have performed a quantitative treatment and proved this effect. Without going into further details, the CTE in the axial direction for the micro-fibril can be expressed as:

$$\alpha_{\parallel}^{f} = x^{C}\alpha_{\parallel}^{C} + (1 - x^{C})\alpha_{\parallel}^{S} - (1 - x^{C})\frac{d\eta}{dT} \tag{4-29}$$

where $\alpha_{\parallel}^{C}$ and $\alpha_{\parallel}^{S}$ are the CTEs of the crystal block **C** and component **S** (See Fig. 4-5(a)), respectively; $\eta = \frac{tE_1^T}{bE_1^C} \propto T$ and t, b and x^C are the volume fraction of the tie molecules, bridges and block crystals *within* the micro-fibrils.

Fig. 4-5(b) shows a well-accepted phenomenological model of an amorphous phase. The amorphous phase is always treated as a mixture of glassy phase and rubbery phase, of which volume fractions are temperature dependent. In other words, a glassy phase may evolve into rubbery phase upon heating. This phase transition does not take place in all glassy phases at once, however, starts from the domains with higher energy and evolves gradually until the transition is fully accomplished [246]. To address this behavior, we adopt the phase evolution law introduced by Guo et al. [116] to describe the temperature dependence of the glassy phase volume fraction within the amorphous matrix:

$$x_g^m(T) = \int_{T_0}^{T} \frac{1}{S\sqrt{2\pi}} e^{-\frac{(T-T_g)^2}{2S^2}} dT \tag{4-30}$$

where S is a constant and T_g represents the glass transition temperature.

By assuming that the amorphous phase is isotropic and with uniform stress distribution throughout the material, the thermomechanical properties are given by:

$$G_{12}^m = \frac{1}{x_g^m \frac{1}{G_g^m} + (1 - x_g^m)\frac{1}{G_r^m}} \tag{4-31a}$$

$$E_1^m = E_2^m = 2G_{12}^m(1 + \nu_{12}^m) \tag{4-31b}$$

$$\alpha_{\parallel}^{m} = \alpha_{\perp}^{m} = x_g^m \alpha_g^m + (1 - x_g^m)\alpha_r^m \tag{4-31c}$$

where x_g^m is the volume fraction of the glassy domain *within* the amorphous phase.

Having obtained the thermomechanical properties for the crystalline micro-fibrils and the amorphous matrix, the on-axis thermomechanical properties that are needed for Eqs. (4-12) and (4-13) can be obtained by noticing the resemblance of the current configuration to the short fiber reinforced composite (See Fig. 4-1(d)). According to the shear lag theory first developed by Cox [247], the effective axial Young's modulus E_1 of a composite containing a discontinuous reinforcing phase of length, l^f, radius, r^f, Young's modulus, E_1^f, volume fraction, V^f, and matrix phase of Young's modulus E_1^m, shear modulus G_{12}^m, is:

$$E_1 = V^f K E_1^f \left(1 - \left(\frac{\tanh(x)}{x}\right)\right) + (1 - V^f)E_1^m \tag{4-32a}$$

$$x = \frac{l^f}{r^f}\left(\frac{G_{12}^m}{E_1^f \ln(2\pi/\sqrt{3}V^f)}\right)^{\frac{1}{2}} \tag{4-32b}$$

with the knowledge that the load transfer between the crystalline micro-fibrils and the amorphous matrix is less than perfect, a constant K is included in the Cox analysis, which is a measurement of the reinforcing efficiency [221, 222].

The transverse Young's Modulus E_2 and in-plane shear modulus G_{12} can be obtained by the handy equations developed by Halpin and Tsai [216, 248]:

$$\frac{P}{P^m} = \frac{1+\xi\eta V^f}{1-\eta V^f} \tag{4-33a}$$

$$\eta = \frac{\frac{P^f}{P^m}-1}{\frac{P^f}{P^m}+\xi} \tag{4-33b}$$

here, P^f is the micro-fibrils property, P^m is the matrix property and ξ is a measurement of the reinforcement geometry, which depends on loading conditions. The values of ξ for E_2 and G_{12} are 0.5 and 1, respectively.

As for the CTEs, by assuming the simple "rule of mixtures", we have:

$$\alpha = V^f a^f + (1 - V^f)\alpha^m \tag{4-34}$$

4.4 Model Validation and Prediction

4.4.1 Parameter identification

The parameters for the multi-scale modeling were determined through various thermomechanical testing, values in the existing literatures, and appropriate curve fittings.

- **Polymeric artificial muscle preparation**

The fabrication of artificial muscles follows the same procedure as in Haines et al. [82], which takes two consecutive steps: twist insertion and coiling. The detailed fabrication procedures can be found in the work by Zhang and Li [87]. After the fabrication, the geometries of the precursor fiber and twisted fiber were measured using a SEM imaging system (Quanta^{TM} 3D FEG field-emission electron microscope) and those of the coiled spring were measured using an optical high resolution CCD camera (Sony XCD-CR90) (See Fig. 4-6). The sample codes, the fabrication descriptions, and the geometrical parameters for different samples that will be used in the modeling are summarized in Table 4-1.

Table 4-1 Summary of samples.

Sample code	Fabrication description	Geometrical parameters
Sample 0	Precursor fiber, polyethylene copolymer.	$d_0 = 0.58mm$
Sample 1T	Twist the fiber under 13.36MPa load until coil nucleation, then anneal the twisted fiber at 85℃ for 90 min.	$d_1 = 0.78mm$ $\alpha_f = 35°$
Sample 2TC	Twist the fiber under 13.36MPa load until coil nucleation, wrap the twisted fiber around a mandrel, then anneal the coiled muscle at 85℃ for 90 min.	$D_c = 2.11mm$ $\alpha_c = 10°$ $n = 8$

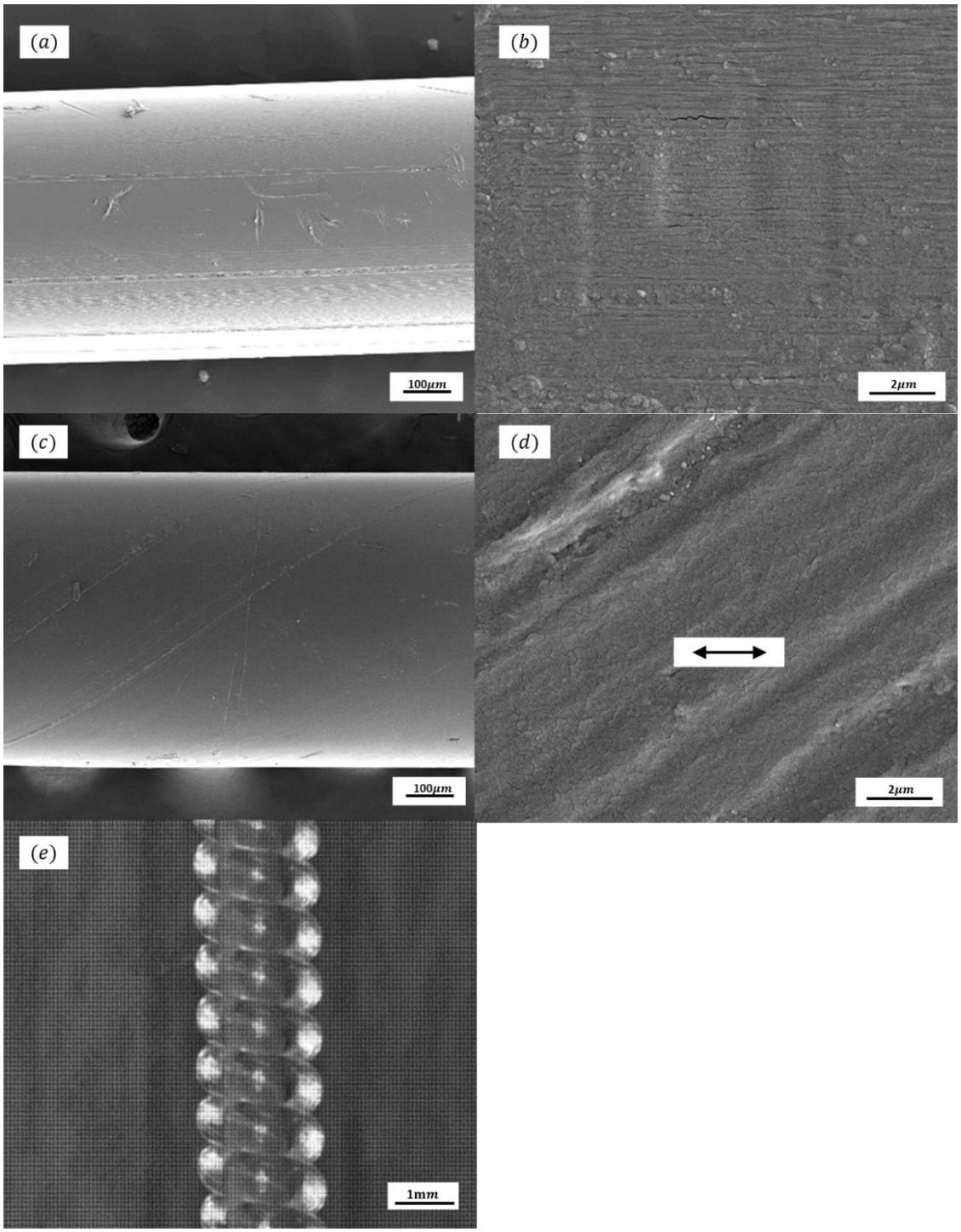

Figure 4-6. (a) and (b) SEM images of the precursor fiber. (c) and (d) SEM images of the twisted fiber. (e) CCD image of the coiled spring.

- **Thermomechanical characterizations**

To investigate the morphologies of the fibers and provide experimental evidence for our model, the SEM observation were conducted on both Sample 0 and Sample 1T. As suggested by previous

studies [220], the high strength and stiffness of polymer fibers are mostly attributed to their highly oriented crystalline morphologies. This is confirmed by the image in Fig. 4-6(b). Although we are not able to accurately measure the volume fraction V^f and aspect ratio l_f/r_f of the micro-fibrils in our samples (in Eq. 4-26), values of 0.75 and 15, respectively, are believed to be appropriate as suggested by previous studies [225, 227, 228]. In addition, it is clear from Fig. 4-6(d) that after the twisting and heat-setting procedures, the micro-fibrils form off-axis configuration as described in our model.

Differential scanning calorimetry (PerkinElmer DSC 4000, USA) was used to investigate the thermal properties of the fishing lines. Samples were cooled from 30°C to -70°C at 10°C/min and heated from -70°C to 240°C, also at 10°C/min. Then, this thermal cycle was repeated. The first cycle DSC results for both Sample 0 and Sample 1T are presented in Fig. 4-7, together with the second cycle DSC results for both samples as a comparison. The results again indicate that the morphology of the fiber consists of two phases: (I) Soft amorphous phase, represented by the broad glass transition region starts from around 20°C and ends around 60°C. (II) Hard crystalline phase, represented by the melting peak at 220°C. No significant change can be observed between Sample 0 and Sample 1T, indicates that the twisting procedure does not interrupt the morphology of the fiber very much and a working cycle between the room temperature (25°C) and 80°C is appropriate for this fishing line. For the second cycle DSC curve, multiple and less perfect melting peaks can be observed, an indication of the less oriented crystalline structure in the raw material compared with the highly oriented fishing line in the first cycle (the first cycle has erased the working history of the fiber and thus both samples show the same DSC curve in the second cycle). The glass transition temperature used in our model is chosen to be $T_g = 30℃$.

A TA Instrument Dynamic Mechanical Analyzer (Q800) was used to perform a strain controlled dynamic temperature scan at a frequency of 1 Hz. A 0.5% oscillating strain was applied to Sample 0 and Sample 1T and the temperature was scanned from 25°C to 80°C at 1°C/min. The temperature dependence of the storage modulus of Sample 0 is presented in Fig. 8 and this result is used to identify the parameters in Eqs. (4-25)-(4-27). The elastic moduli for the crystal blocks are obtained from the stiffness constants of orthorhombic polyethylene crystal calculated by Tashiro et al. [239] and those of amorphous matrix are approximated using the experimental results by Boyd [249] and Xiong et al. [250]; the rest of the parameters in micro-scale modeling, *i.e.* λ, K and S (in Eqs. (4-25)-(4-27)) can be varied and determined by fitting into the experimental results (See Fig. 4-8 upper lines). In addition to that, as evidenced by Sample 1T in Fig. 4-8, the axial modulus has been decreased after twisting due to disorientation.

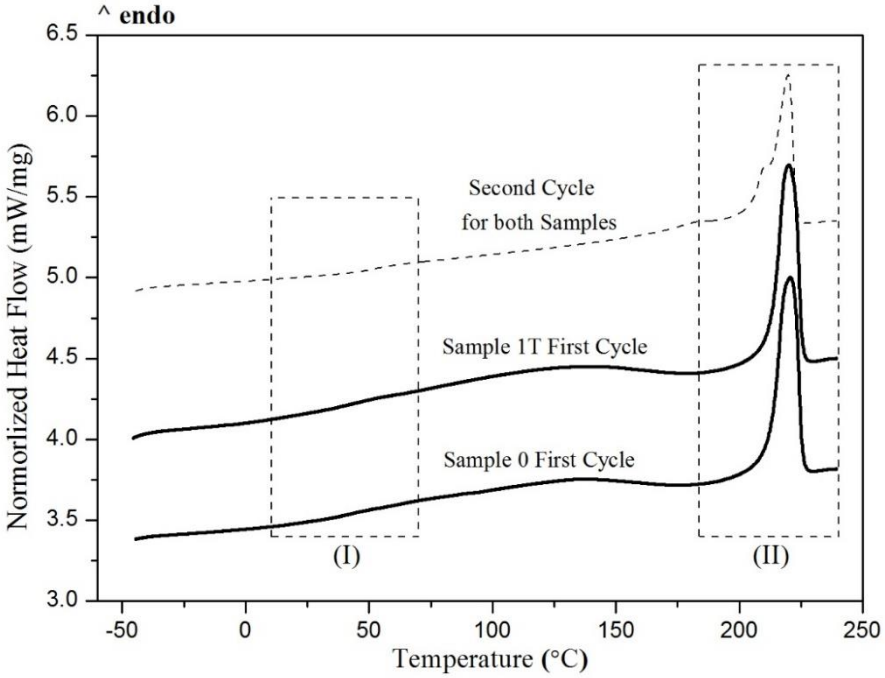

Figure 4-7 DSC results for Sample 0 and Sample 1T.

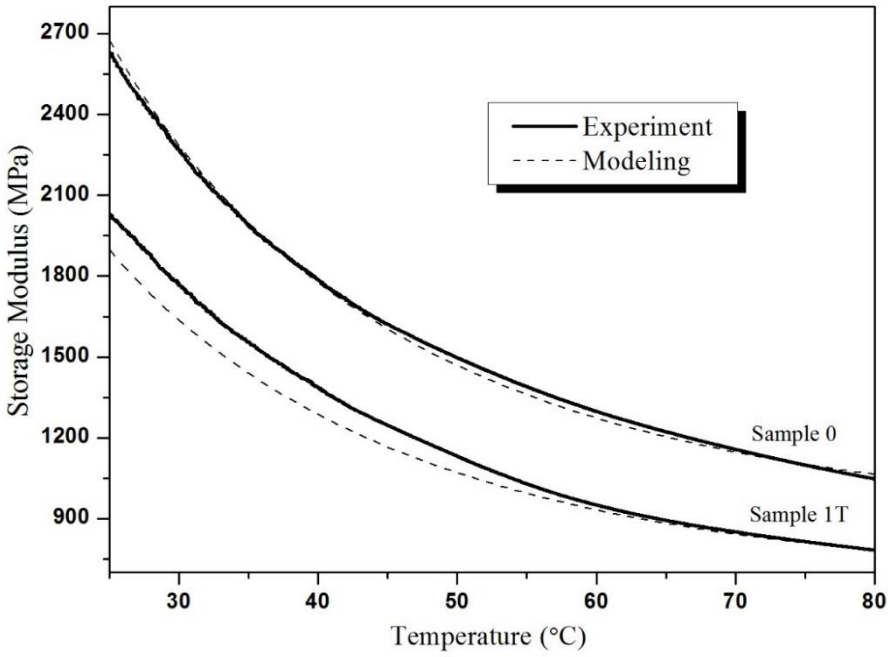

Figure 4-8 Temperature dependences of axial moduli for both Sample 0 and Sample 1T (Solid lines: DMA experiment results. Dash lines: modeling results).

A temperature scan test under constant static force was also conducted on Sample 0 in order to measure the coefficient of axial thermal expansion (α_1). In our study, α_1 is assumed to be linear temperature dependent, and accordingly, the displacement is a quadratic function in terms of temperature (See Fig. 9(a)). The coefficient of transverse thermal expansion (α_2) is not easy to measure, so we extract the experimental results for a similar material from Choy et al. [230]. Likewise, α_2 is simulated by assuming a linear temperature dependence (Fig. 4-9(b)).

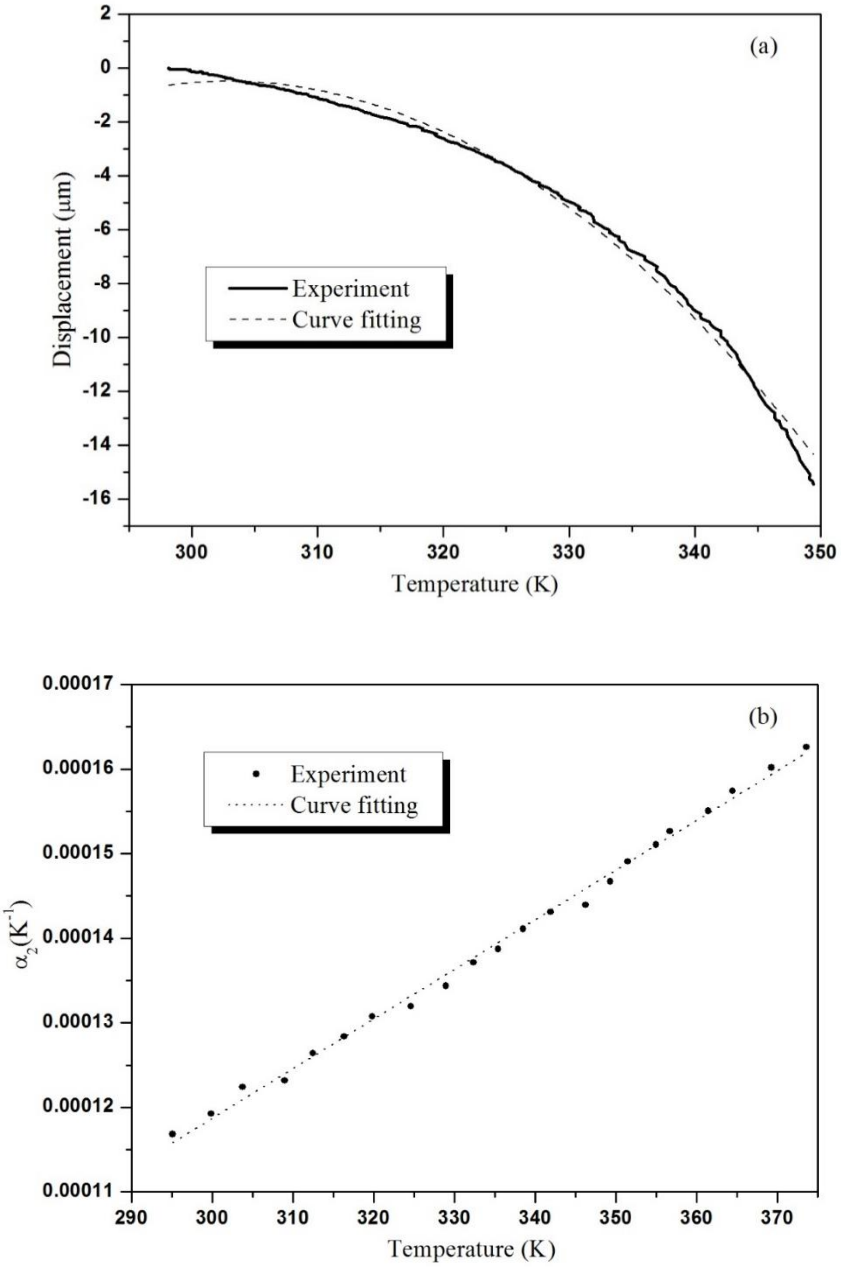

Figure 4-9 Experimental and curve fitting results for the thermal properties of the precursor fiber in axial (a) and (b) transverse directions (The experimental data were extracted from Choy et al. [230]).

- **Summary of parameters**
-

Up to now, we have completed the multi-scale modeling and determined the input parameters for the nano- and micro-, meso- and macro- scale modeling using experimental measurements, literature research and curve fitting procedures. In Table 4-2, all the parameters, together with their description and identification method, have been specified. The multi-scale model was then coded and implemented into the MATLAB program to reproduce the thermomechanical behavior of the twisted fiber and the coiled spring.

Table 4-2 Parameters used for the present multi-scale model.

Parameters	Descriptions	Values	Identification Method
Parameters for nano- and micro-scale modeling			
$C_{11}^{C}(MPa)$	Stiffness of the crystal block in fiber direction (Eq. 4-28(a))	300,000	[239]
λ	Scale factor to account for the weakening effect of the inter-crystalline materials to the whole micro-fibrils (Eq. 4-28(a))	3.25	Fit into DMA experimental results (Fig. 4-8 upper lines)
$E_2^f(MPa)$	Young's modulus of the micro-fibrils in transvers direction (Eq. 4-28(b))	8,000	[239]
l_f/r_f	Aspect ratio of the micro-fibrils (Eq. 4-32(a))	15	[227]
K	Measurement of the reinforcing efficiency (Eq. 4-32(a))	0.85	Fit into DMA experimental results (Fig. 8 upper lines)
V^f	Volume fraction of the crystalline micro-fibrils (Eqs. 4-32 and 4-27)	0.75	[225]
S	Constants in the phase evolution law (Eq. 4-30)	40	Fit into DMA experimental results (Fig. 4-8. upper lines)
T_g(℃)	Glass transition temperature (Eq. 4-30)	30	DSC results (Fig. 4-7)
$G_g^m(MPa)$	Shear modulus of the amorphous matrix in the glassy state (Eq. 4-31(a))	90	[249]

ν_{12}^{m}	Poisson's ratio of the amorphous matrix (Eq. 4-31(b))	0.4	[249]
Parameters for meso-scale modeling			
$\alpha_1(K^{-1})$	Axial direction CTE	$-1.35\times10^{-6}T + 4.20\times10^{-4}$	Fit into experimental results in Fig. 9(a)
$\alpha_2(K^{-1})$	Transverse direction CTE	$5.78\times10^{-7}T - 5.75\times10^{-5}$	[230]
ν_{12}	Poisson's ratio	0.465	Measurement
ν_{23}	Poisson's ratio	0.45	[226]
$r^0(mm)$	Radius for the inner most hollow cylinder	10^{-10}	Suitable for simulation of solid cylinder
$r^N(mm)$	Radius for the outer most hollow cylinder	0.39	Measurement
Parameters for macro-scale modeling			
n	Number of active coils	8	Measurement
$D(mm)$	Outer diameter of the coil	2.11	Measurement
$\alpha_c(°)$	Pitch angle	10	Measurement

The simulation flowchart using the MATLAB program is summarized below in Fig. 4-10.

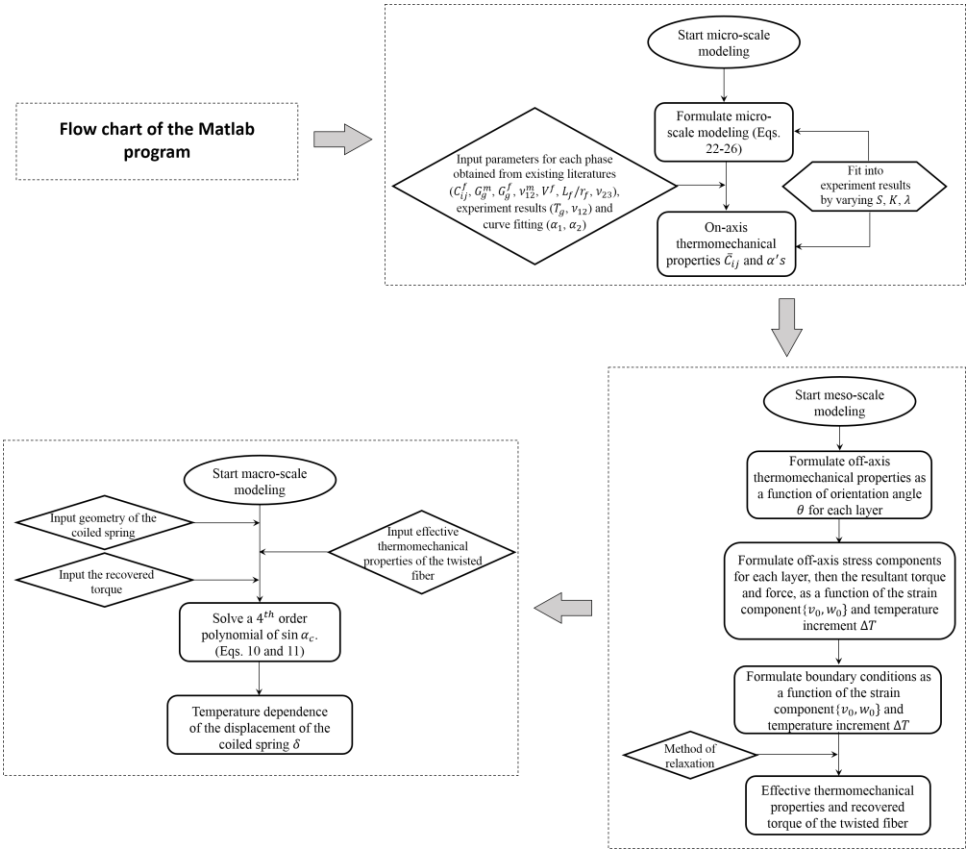

Figure 4-10 Flow chart of the Matlab program for the multi-scale modeling.

4.4.2 Comparison with experimental results

- **Axial modulus of Sample 1T**

The elastic modulus of the twisted fiber is reproduced using the meso-scale model and is presented in Fig. 4-8 (bottom dash line), together with the experiment results (bottom solid line). The modeling result exhibits good agreement with the experiment result. The small deviation of the modeling result from the experimental result at the beginning of the test is most likely attributed to the choice of the transverse elastic properties, which are not able to be obtained experimentally at this time.

- **Torsional actuation of Sample 1T**

We used a torque sensor (Mark-10 MR50-50Z Plug & Test Universal Torque Sensor, with a resolution of 0.02ozF-in) to measure the torque generated by Sample 1T fixed at both ends. Fig. 4-11 shows that our meso-scale model successfully captures the torsional actuation trend of the twisted fiber, which is essential to the tensile actuation behavior of the coiled spring.

- **Tensile actuation of Sample 2TC**

Finally, the tensile actuation of Sample 2TC is measured using DMA by applying a constant force of 1.5N to the coiled spring, and heating and cooling the temperature between 25°C and 80°C at 10°C/min. Fig. 4-12 proves the ability of the macro-scale model in reproducing the trend of the coiled spring (muscle).

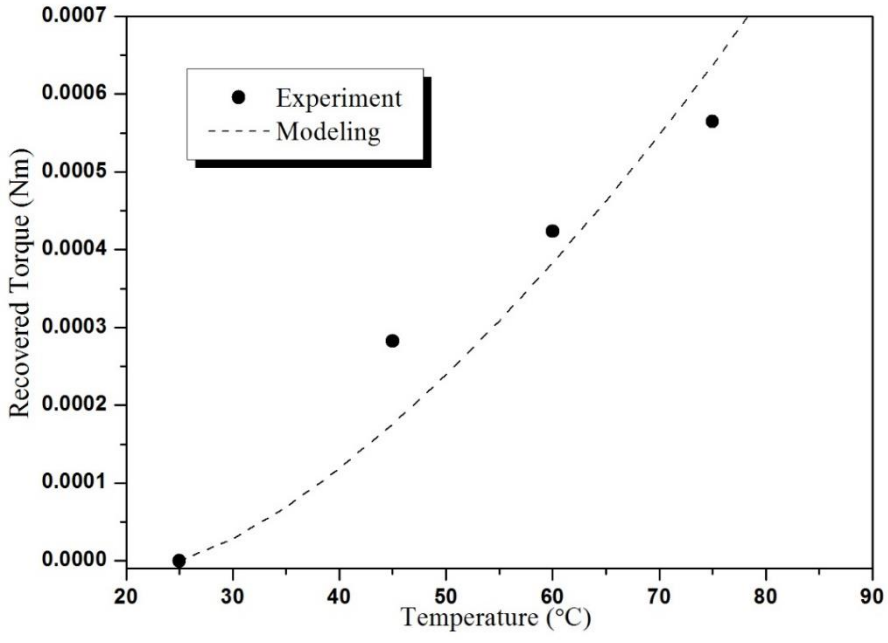

Figure 4-11 Experiment and modeling results of the recovered torque as a function of temperature.

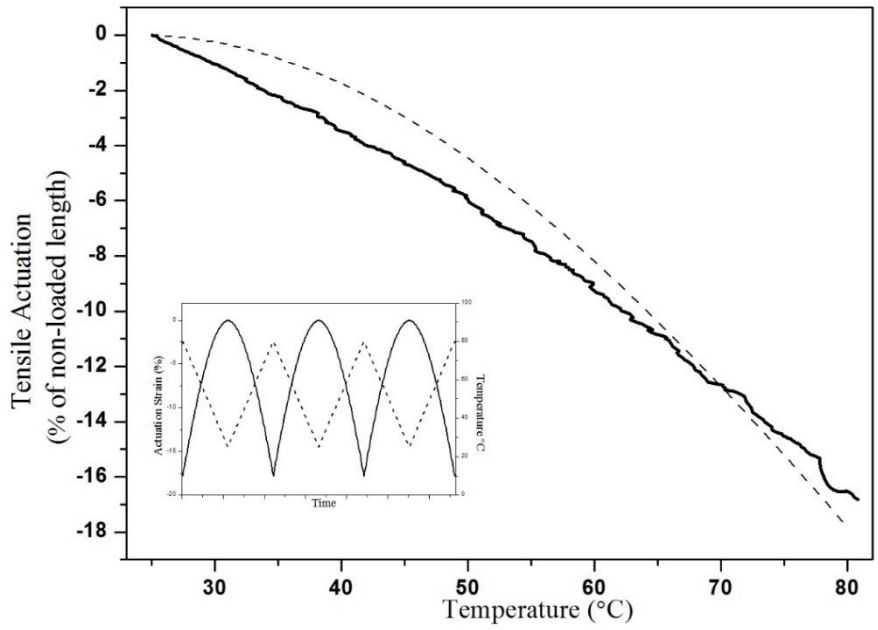

Figure 4-12 Experiment and modeling results of the tensile actuation of the coiled spring (solid line: test results; dashed line: modeling results). The inset shows the simulation results of multiple actuation cycles (solid line: calculated results of strain actuation; dashed line: temperature).

4.4.3 Prediction and Discussion

To further demonstrate the prediction ability of our model, we here performed a series of parametric studies, aiming to investigate how the parameters at different scales affect the thermomechanical properties of the fiber, the torsional actuation response of the twisted fiber and eventually, the tensile actuation response of the coiled spring.

- **Effect of micro-scale parameters on thermomechanical properties of the precursor fiber**

Fig. 4-13(a) exhibits the effect of crystalline micro-fibril volume fraction (V^f) on the axial modulus of the precursor fiber. As expected, higher V^f increases the Young's modulus of the precursor fiber in axial direction. Likewise, the Young's modulus in the transverse direction and the shear modulus can also be increased by increasing V^f (Not shown in the figure for brevity).

One of the most efficient methods to enhance the mechanical properties of the as-fabricated polymeric fibers is by highly stretching the fiber. During this procedure, the crystalline lamellae in the micro-fibrils are oriented along the draw direction and end up with crystalline micro-fibrils with higher aspect ratios (l_f/r_f). In Fig. 4-13(b), we illustrate that higher aspect ratio of the micro-fibrils leads to higher axial modulus. It has also been experimentally demonstrated that the drawing procedure can produce higher thermal anisotropy, that is, higher thermal contraction in the axial

direction and higher thermal expansion in the transverse direction [230]. In the following subsection, we will show how the changes in thermomechanical properties of the precursor fiber affect the behavior of the twisted fiber.

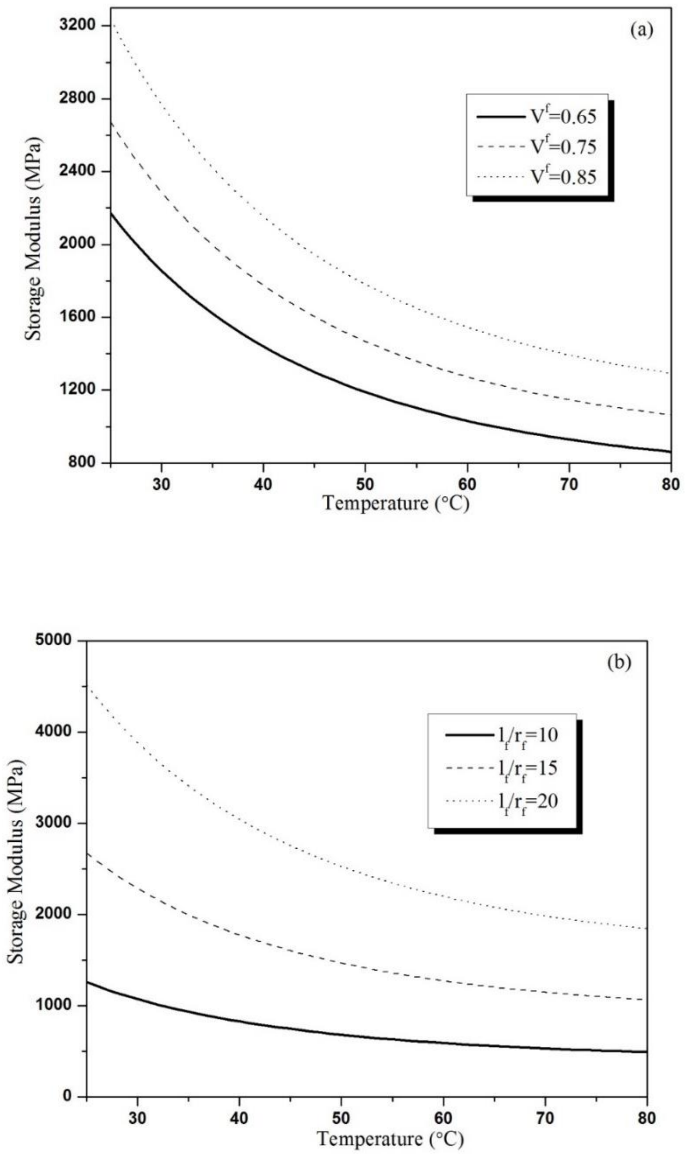

Figure 4-13 Axial Young's modulus of the precursor fibers with different (a) crystalline micro-fibrils volume fractions and (b) micro-fibril aspect ratios.

- **Effect of meso-scale parameters on torsional actuation response of the twisted fiber**

In Fig. 4-14(a), we compare the torsional behavior of twisted fibers made of precursor fibers with different axial moduli, which is attributed to different micro-fibril aspect ratio. It is clear that the precursor fiber with higher micro-fibril aspect ratio has higher axial modulus (Fig. 4-13(b)),

and eventually lead to better torsional actuation performance for the twisted fiber. In addition, based on a simple helix analysis, Haines et al. [82] concluded that "both contraction of these helically configured polymer chains and fiber diameter expansion will cause fiber untwist". Therefore, it is envisioned that the larger the anisotropy between the thermal expansion in the axial and transverse direction, the higher the untwisting tendency, and hence the larger the recovered torque will be. This is proved in Fig. 4-14(b). Here we multiply the original CTE's of the twisted fiber "Anisotropy 1" by a factor of 2 and 3, resulting in twisted fiber specimens with larger anisotropies, specimen "Anisotropy 2" and specimen "Anisotropy 3", respectively. As stated above, a facile strategy to increase the thermal anisotropy is by stretching the precursor fiber [230].

According to the experimental results in Haines et al. [82], the geometrical configurations of the twisted fibers also have a large impact on the actuation behavior. In Fig. 4-14(c), the recovered torque dependence on the twisted fiber bias angle is presented. It turns out that the torque does not follow a monotonous trend with respect to bias angles; instead, it reaches its maximum around 35 °. The appearance of the maximum actuation is as a result of the various orientations in each cylindrical layer and the constraints between each layer (See Eq. 4-19d).

Predictions in Fig. 4-14 suggested that if we could find a fiber with a remarkable combination of high modulus and large thermal anisotropy, along with an appropriate fiber bias angle, which can be altered by applying different load during twisting insertion, the torsional actuation performance of the twisted fiber would be significantly improved. In the following subsection, we will show how the improvement in torsional actuation of the twisted fiber affect the manifestation of the coiled spring.

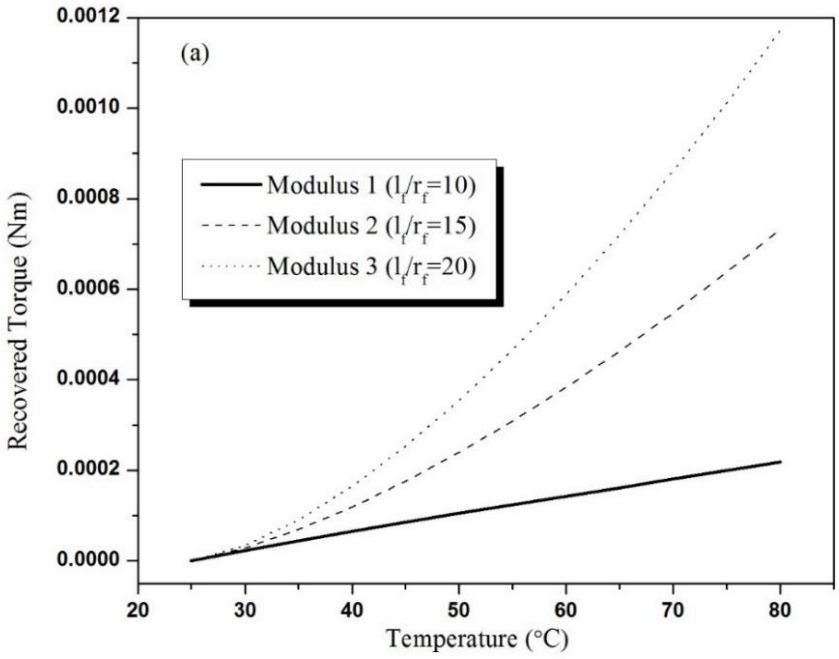

(Figure 4-14 continued)

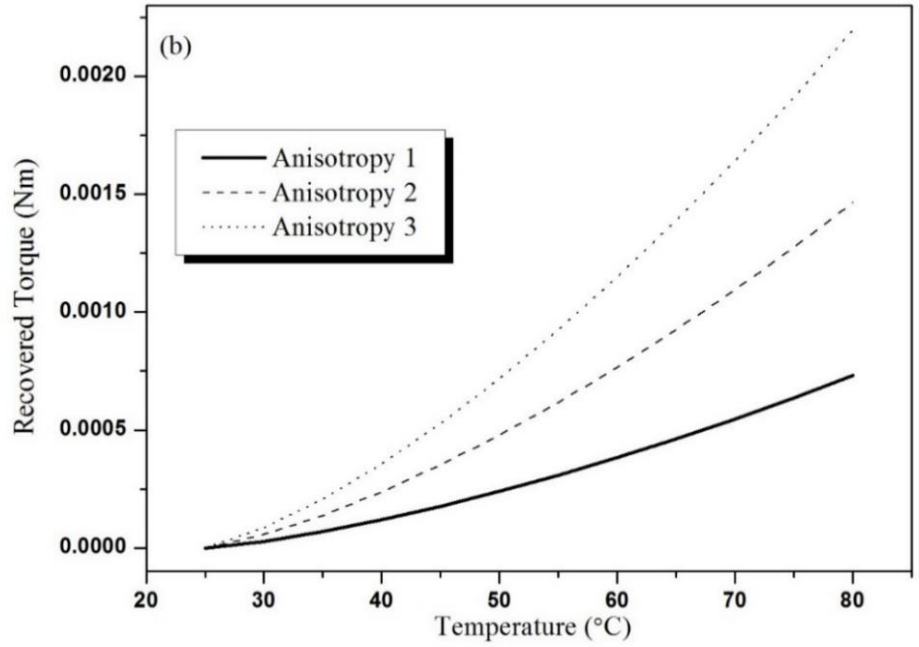

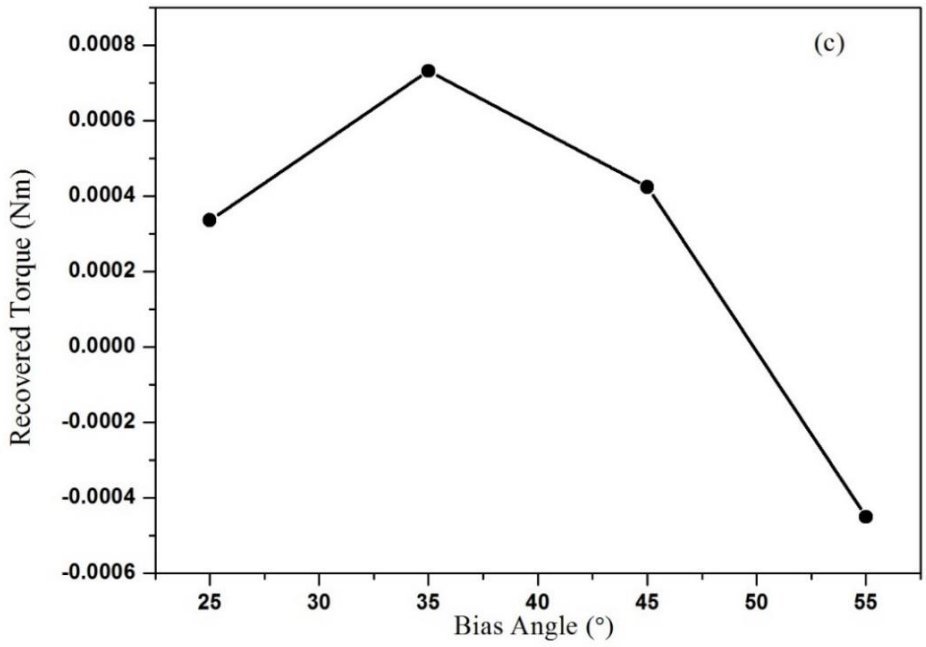

.

Figure 4-14 Recovered torque generated by the twisted fiber with different (a) axial moduli, (b) thermal anisotropies, and (c) bias angles.

- **Effect of macro-scale parameters on tensile actuation response of the coiled spring**

As has been extensively stated in the previous sections, the remarkable tensile actuation behavior of the coiled spring is driven by the torsional actuation generated by the twisted fiber during heating. This is quantitatively reflected in Eq. 4-10, where it is clear that the external applied force F is responsible for the elongation of the spring, just like in the regular spring with a stiffness of f_{11}. The recovered torque M_{rec}, however, depending on its sign, can either contribute to the total elongation (when twisting and coiling have opposite chirality and M_{rec} is negative) or compensate for the external force and responsible for contraction of the spring (when twisting and coiling have the same chirality and M_{rec} is positive). To clarify, we take the chirality of the coiled spring as the reference, i.e., the pitch angle of the coiled spring is always positive. In this way, the twisted fiber with chirality that matches that of the coiled spring has a positive fiber bias angle and this twisted-then-coiled spring is defined as homochiral system. Likewise, the twisted fiber with chirality that is opposite to that of the coiled spring has a negative fiber bias angle and the resulting coiled spring is heterochiral. In Fig. 4-15(a), the effect of the fiber bias angle, and hence the recovered torque on the tensile actuation response of the artificial muscle is presented. When the fiber bias angle increases, more recovered torque can be generated upon heating, and thus results in better tensile actuation performance in both homochiral and heterochiral cases. As expected, the maximum stroke is again reached around $\pm 35°$. Our prediction is very close to the experimental results in Fig. 4F of Haines et al. [82]. Therefore, an appropriate fiber bias angle, is an important factor to tune the tensile actuation performance. Without extensive experimental testing, our model provides an efficient numerical tool to seek the optimized fiber bias angle.

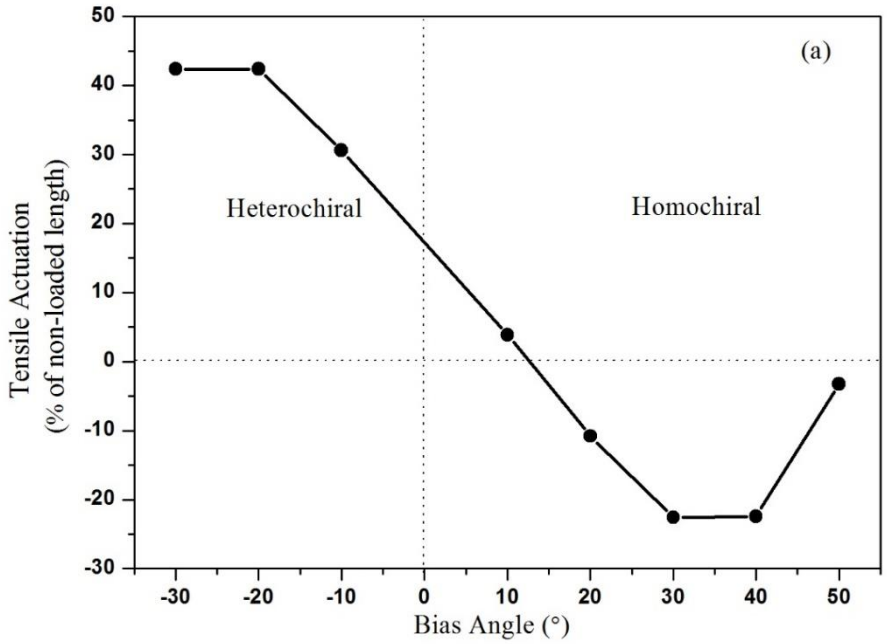

(Figure 4-15 continued)

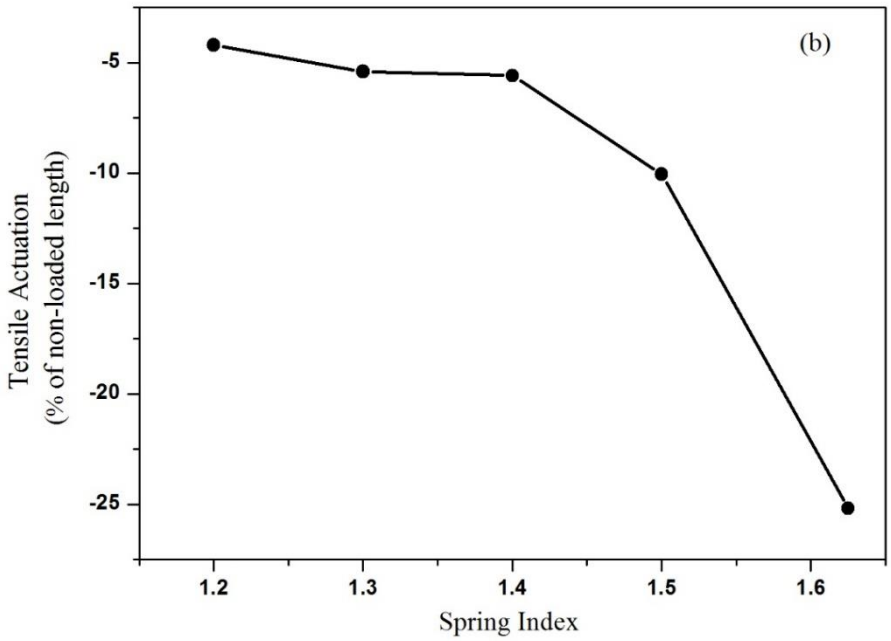

Figure 4-15 Prediction of the tensile stroke as a function of (a) fiber bias angles and (b) spring indices.

As pointed out in the previous section, the recovered torque of the twisted fiber, and hence the tensile actuation of the coiled spring, can also be increased by enhancing the axial modulus (Fig. 4-13(b) and Fig. 4-14(a)) and the thermal anisotropy (Fig. 4-14(b)) of the precursor fiber. One of the promising candidates could be two-way shape memory polymers [15, 54-56, 58-63, 251, 252], which behave similarly to polymers with negative CTEs (i.e., heating induces contraction and cooling causes expansion). Because the two-way shape memory effect is much larger than the negative CTEs of the fishing lines, which suggests giant thermal anisotropy, it is expected that two-way shape memory polymers would have remarkable muscle behavior.

Finally, Fig. 4-15(b) exhibits the contracting stroke as a function of spring indices and shows that larger spring index leads to higher contracting stroke, which has also been proved experimentally in Haines et al. [82] and Zhang and Li [87]. Nevertheless, smaller spring index may still be used in some applications when higher actuation force is in favor over higher stroke.

4.5 Conclusion

In this paper, a multi-scale modeling framework based on a top-down analysis has been developed for the actuation response of the polymeric artificial muscles. The model was validated against the experimental results for the polyethylene copolymer fiber based muscles. The physical origin and dependence of the torsional actuation of the twisted fiber and the tensile actuation of the twisted-then-coiled spring on temperature have been elaborated and reproduced. A parametric

study was further conducted to help future design and optimization of such innovative artificial muscles. The important results of this work include:

(1) In the macro-scale model, a consistent application of Castigliano's second theorem (CST) has been used, to account for the combined effect of the axial applied force and recovered torque on the thermally triggered tensile actuation. The combined contribution of the applied force and the recovered torque is evidenced by the fact that the tensile stroke is largely dependent on fiber bias angle, because the fiber bias angle plays an important role in determining the recovered torque. Another predication from our parametric study shows that the actuation behavior of the muscle can be tuned by spring indices of the twisted-then-coiled spring. More specifically, larger index results in higher tensile stroke.

(2) In the meso-scale model, the torsional behavior of the twisted fiber was reproduced by using classical composite material theory and helical anisotropic cylinder analysis. The appearance of a coupling term $\alpha_{z\theta}$ in the off-axis properties proves that a reversible thermal shear strain will be generated during heating or cooling. In other words, the torsional behavior of the twisted fiber can be explained from the composite material point of view. Parametric study indicates that there exists an optimized fiber bias angle that maximizes the recovered torque and hence the tensile stroke.

(3) The nano- and micro-scale modeling for the precursor fiber is case dependent. In our study, due to the fact that the morphology of the semi-crystalline polyethylene copolymer fiber consists of discontinuous crystalline micro-fibrils embedded into an amorphous matrix, we make use of the classical theories in continuum mechanics to simulate the thermomechanical properties of the fiber. Parametric studies suggest that by increasing the modulus and the thermal anisotropy of the precursor fiber, the actuation performance of the artificial muscle will be greatly improved.

Some new thermally reversible polymers, such as two-way shape memory polymers, may provide remarkable actuation response.

CHAPTER 5 ARTIFICIAL MUSCLES MADE OF CHIRAL TWO-WAY SHAPE MEMORY POLYMER FIBERS

In this work, we demonstrate the unusual improvement of the tensile actuation of hierarchically chiral structured artificial muscle made of two-way shape memory polymer (2W-SMP) fiber. Experimental results show that the chemically cross-linked Poly(ethylene-co-vinyl acetate) (PEVA) 2W-SMP fibers possess an average negative coefficient of thermal expansion (NCTE) that is at least one order higher than that of the polyethylene (PE) fiber used previously. As expected, the increase in axial thermal contraction leads to increase in the recovered torque ($4.4Nmm$) of the chiral fiber and eventually in the tensile actuation of the twisted-then-coiled artificial muscle ($67.81 \pm 1.82\%$). A mechanics model based on Castigliano's second theorem (CST) is proposed and the calculated result is consistent with the experimental result (64.17% tensile stroke). The model proves the significance of the NCTE and the recovered torque on tensile actuation of the artificial muscle, and can be used as a guidance for future design.

5.1 Introduction

Structural chirality can be found in many natural materials, such as climbing plant tendrils [253], DNA [254], snail shells [255] and even the nanostructure of butterfly wings [256]. One of the merits of chirality is to endow the materials with unusual mechanical, optical, and magnetic properties. Inspired by our mother nature, researchers have introduced chirality to many man-made materials and have fabricated materials and devices with outstanding features, such as helical nanowires [257], chiral carbon nanotubes [258], etc. Recently, Haines et al. [82] have created artificial muscles with hierarchical chiral structure made of polymer fibers that can offer up to 49% tensile actuation. The giant tensile stroke, robustness, low cost and easy tuning procedure of this polymeric artificial muscle have confirmed the significance of this innovative discovery and have opened up new horizons toward the development of effective devices, for instance, morphing airplanes and vehicles [86], self-healing composite [87], robotics [89], etc.

Recently, Sharafi et al. [215] have developed a bottom-up multi-scale modeling framework to explain the remarkable actuation response of this type of artificial muscles. However, their model is very complex and needs significant curve fitting effort. Most recently, Yang et al. [259] have developed a top-down multi-scale model and elucidated the physical origin behind the remarkable tensile actuation behavior of the twisted-then-coiled artificial muscles. They have demonstrated that the anisotropic dimensional changes at the meso-scale level, i.e., reversible thermal contraction in axial direction and expansion in radial direction in the precursor (untwisted) fiber, result in an intrinsic torsion in the chiral (twisted) fiber upon heating and eventually lead to the giant tensile actuation of the helical coil in the macro-scale level. This underlying mechanism shares the same essence with the climbing tendrils [260], where the intrinsic torque is provided by the change in helical angle in the cellulose fibrils at the subcellular level. Additionally, the model suggested that the intrinsic torque of the chiral fiber, hence the tensile actuation of the helical artificial muscle, can be enhanced by increasing the thermal anisotropy of the fiber while keeping other properties unchanged. For all the precursor fibers in Haines's work [82], the axial thermal actuations of the fibers are driven by the intrinsic axial thermal contraction (negative coefficient of thermal expansion (NCTE)) of the polymer components and is limited to about 5%, which limits the maximum tensile actuation to 49%. Therefore, in order to further improve the thermal actuation

of the precursor fiber, a different driving force should be adopted. We believe that precursor fibers made of two-way shape memory polymer (2W-SMP) (contraction upon heating and expansion upon cooling, similar to polymers with NCTE) can be a promising candidate, since the reported thermal actuation of the 2W-SMPs in the existing literature is always an order higher than that of the precursor fibers used previously.

Regardless of compositions, architectures and designs, the necessary condition for two-way shape memory effect (2W-SME) is the co-existence of a stable network and a switching domain that can respond to the external stimuli [30]. The stable network, mostly constructed from chemical cross-links, can endure load and retain permanent shape upon heating. The switching domain, consisting of oriented and crystallizable molecular chains, is responsible for the reversible shape change of the SMP, driven by the non-isothermal stress-induced crystallization. 2W-SME has been demonstrated in several polymer systems, in the form of film or bulky materials [15, 16, 59-63, 66]. However, fabrication of chemically cross-linked 2W-SMP fiber is still challenging due to the resistance in chemical cross-linked polymers. Nevertheless, our group have recently fabricated chemically cross-linked Poly(ethylene-co-vinyl acetate) (PEVA) based 2W-SMP fibers that can offer reversible actuation up to ~15%.

In this study, we first describe the fabrication procedure of the 2W-SMP fiber. Then, the thermomechanical properties of the precursor and chiral 2W-SMP fibers are investigated. and the tensile actuation performance of both fibers are presented. The polymeric chiral fibers are subsequently fabricated into coiled muscles and the unusual improvement in the tensile actuation are finally demonstrated both experimentally and theoretically.

5.2 Experimental

5.2.1 Fabrication procedures

- **Fabrication of two-way shape memory polymer fibers**

Fabrication of 2W-SMP fiber takes four consecutive steps: (1) preparation of raw material; (2) melt extrusion, during which the as-prepared polymer was extruded from the single screw extruder (Labtech Engineering (Thailand)) to form fiber-shaped material; (3) post curing, in order to form chemical cross-linked semi-crystalline polymeric fibers; and (4) programming, during which the cured fiber-shaped samples were stretched to 150% strain at 75 ℃ to enhance the alignment of the molecules, so that the 2W-SME can be better introduced to the fibers. Compared to the traditional fabrication technology for the bulky or film 2W-SMP, there are two main challenges need to be overcome during the fabrication of fibrous 2W-SMP.

The first one is how to achieve uniform dispersion of cross-linkers during the preparation process. The non-uniform dispersion will result in local over-dilute or over-loading of the cross-linkers in the as-prepared polymers. As has been pointed out previously [15], the 2W-SME is susceptible to cross link density ν_c: a critical value must be reached to realize the 2W-SME. Increasing the value continuously will have negative impact on the actuation manifestation (elongation upon cooling). Also, the content of cross-linker affects the viscosity of the material. An appropriate value for viscosity is desired in order to obtain smooth fiber during melt extrusion. Unlike bulky and film materials, fibrous materials have lower tolerance to non-uniformity.

Therefore, traditional preparation method cannot meet the requirement. In this work, the uniformity of dispersion was improved by using the "solution method" and 5% (wt%) dycumyl peroxide (DP) was used as the cross-linker to form the continuous network for our 2W-SMP system. At the beginning, PEVA-terahydrofuran (THF) solution was stirred in a 70 ℃ silicon oil bath for 12 hours until homogenous solution was formed. Afterwards, an appropriate amount of DP-THF solution was dropped into it. The new mixture was then kept in a shaker at 70 ℃ until well dispersion. This mixture was poured onto a big piece of Teflon sheet. The gelation occurs very quickly and prevents further motion of small molecules. Once this physical cross-link dominated gel has been dried, a well dispersed solid solution was obtained. The solid solution was granulated into small pieces as raw material for melting extrusion processing.

The second challenge is how to maintain the fibrous shape during the post curing process. Normally, a rigid mold which is easy to be removed from the cured sample is used. However, in our case, due to the size and texture of the fibrous sample, this is not a practical method. To solve this problem, a so-called "double-layered wrap" was used. The extruded wire was first wrapped by Teflon tape which is easy to be peeled off. Then aluminum foil was wrapped on top of it to maintain the shape during the post-curing process. The wrapped wires were then placed in an oven for one hour under 160 ℃ for curing. Afterwards, the cured samples were slowly cooled down to room temperature. After peeling off the aluminum foil and the Teflon tape, the fibrous sample was ready for further processing.

- **Fabrication of artificial muscles**

The fabrication of the artificial muscles follows the same procedure as in Haines et al.'s work [82], which takes two consecutive steps: twist insertion and coiling (See Fig. 5-1 for the optical images).

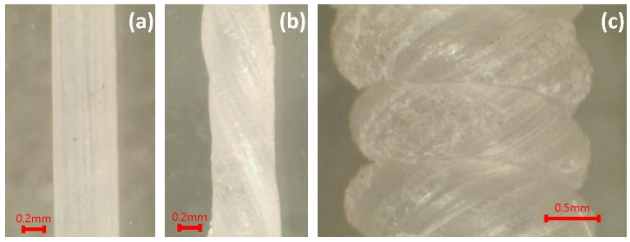

Figure 5-1 Optical images for (a) precursor fiber, (b) chiral fiber after twist insertion procedure and (c) artificial muscle with hierarchical chiral structure after twisting-then-coiling procedure.

5.2.2 Thermomechanical properties measurement for the polymer fibers

To characterize the thermomechanical properties of the fibers and provide input information for our mechanics model, we measured the temperature dependence of the axial Young's moduli E_1 of both precursor and chiral fiber using a TA Instrument Dynamic Mechanical Analyzer (DMA Q800). In the test, the samples were heated from T_{low}(20℃) to T_{high}(67℃). The choices of the temperature are based on the crystallization and melting behavior of the fiber. T_{low} should be lower than the onset of the crystallization temperature, and T_{high} should be within the broad melting range of the fiber.

For the shear moduli G_{12}, a torsional pendulum apparatus, together with a temperature controlled coil heater were used (See Fig. 5-2 for the experiment setup). In the test, one end of the fiber sample was clamped in a fixed grip and the other end was carefully centered in a slotted disk shaped pendulum and secured using a set of screws. Following the experimental and analysis procedure presented by Deteresa et al. [261], the shear modulus G_{12} of a circular cross-sectioned fiber can be expressed in terms of the fiber gauge length L_f, the fiber radius r_f, the moment of inertia of the disc I and the oscillation period τ using Eq. 5-1:

$$G_{12} = \frac{8\pi L_f I}{r_f^4 \tau^2} \tag{5-1}$$

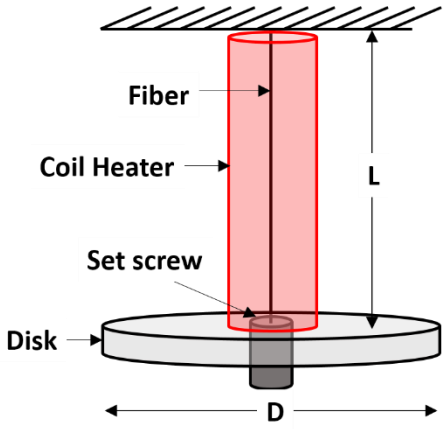

Figure.5-2 Schematic diagram of torsional pendulum apparatus. The pendulum disc diameter is 3.8cm and mass is 13.90g.

As pointed out previously, the chiral fiber can generate intrinsic torque upon heating. In this work, we used a torque sensor (Mark-10 MR50-50Z Plug & Test Universal Torque Sensor) together with the coil heater to measure the torque generated by the twisted fiber fixed at both ends. The torque generated at T_{high} was measured and the test was repeated for three times.

5.2.3 Two-way shape memory effect of polymer fibers

The DMA Q800 under force controlled mode was used to explore the two-way shape memory effect of the fibers. In the test, the samples were heated and cooled at the rate of $10℃/min$, under a constant load σ_{act} between T_{low}(20℃) and T_{high} (67℃). The actuation strain (ε_{act}) of the 2W-SMP fiber is defined as:

$$\varepsilon_{act} = \frac{L_{low}(\sigma_{act}) - L_{high}(\sigma_{act})}{L_{low}(\sigma_{act}=0)} \times 100\% \tag{5-2}$$

where L_{high} is the length of the sample at high-temperature T_{high} and L_{low} is the length at low temperature T_{low}, both with stress, σ_{act}, applied. The 2W-SME is quantified using the average negative coefficient of thermal expansion (NCTE), defined as:

$$\bar{\alpha}_{act} = \frac{\varepsilon_{act}}{T_{high} - T_{low}} \tag{5-3}$$

5.3 Experimental Results and Discussion

5.3.1 Thermomechanical properties of the polymer fibers

A summary of the thermomechanical properties of both the precursor and chiral fibers at different thermal conditions are given in Table 5-1.

Table 5-1 Experimental results for the axial Young's moduli $E_1(MPa)$ and shear moduli $G_{12}(MPa)$ of fibers at low temperature $T_{low} = 20℃$ and high temperature $T_{high} = 67℃$. (*Approximated value.)

Specimen	$E_1@T_{low}$	$E_1@T_{high}$	$G_{12}@T_{low}$	$G_{12}@T_{high}$
Precursor fiber	31.22 ± 4.01	6.49 ± 0.26	7.43 ± 0.35	4.42 ± 0.14
Twisted fiber	3.76 ± 0.83	0.75 ± 0.26	8.30 ± 0.21	4.94^*

Notice that, a decrease in axial Young's modulus E_1 can be observed after the twisting procedure. Interestingly, the fiber experiences almost the same level of degradation at low and high temperatures. In other words, the ratios of the precursor fiber modulus to the twisted fiber modulus at T_{low} and T_{high} are very close (8.30 and 8.65). The shear modulus G_{12}, on the other hand, increases after the twisting procedure. The changes in the thermomechanical properties between the precursor and twisted fibers can be understood and reproduced by the coordinate transformation in a transversely isotropic material [259]. It is worth mentioning that, for a twisted fiber, it tends to rewind or untwist upon heating. Therefore, the shear modulus of the twisted fiber at an elevated temperature can't be obtained using the current experimental apparatus. In our work, for the sake of simplicity, we estimated the value of G_{12} at T_{high} for the twisted fiber by assuming that the levels of enhancement in shear modulus at the high temperature are the same as that at the low temperature.

5.3.2 Tensile actuation behavior of polymer fibers and artificial muscles

The results for the two-way shape memory effect of the precursor fiber are presented in Fig. 5-3 (a) and in Fig. 5-3(b), the average NCTEs of the precursor and chiral fibers are presented in terms of the applied load. Fig. 5-3(b) reveals that the 2W-SME increases linearly with the applied load, mostly due to the fact that higher stress can promote extended chain crystallite growth toward a direction parallel to the stretching direction [15]. Twisting the fiber will disturb the alignment of the molecular chains. As a result, a degradation in 2W-SME can be observed in the chiral fiber. In Fig. 5-3(b), we also presented the average NCTEs of the PE fibers that we previously used to make artificial muscle [259]. Our 2W-SMP fibers possess an average NCTE that is at least one order higher than that of the PE fiber. Indeed, PE fiber has a higher melting temperature. However, in the situation where high operating temperature is not necessary or not allowed, our 2W-SMP fiber can serve as a more efficient light-weight actuator.

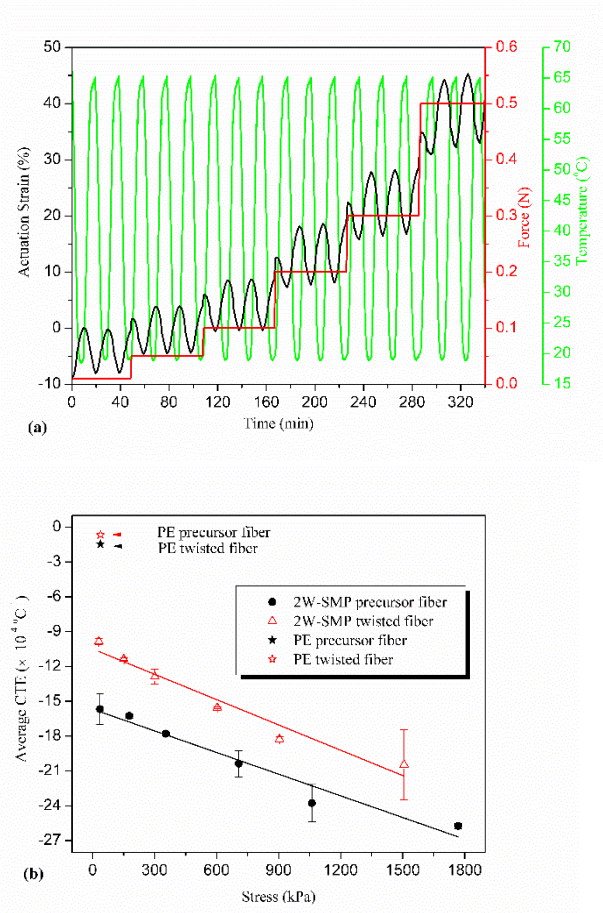

Figure 5-3 (a) 2W-SME of the precursor fiber under different load conditions. (b) Average CTEs for the precursor (solid circles) and chiral (hollow triangles) 2W-SMP fibers and PE fibers (solid and hollow stars at the upper left corner) as a function of applied load.

The torque generated by the twisted fiber at T_{high} is as high as $4.4Nmm$ (tests were repeated for three times and the results were stable), which is about an order higher than the recovered torque ($0.6Nmm$) generated at 80℃ in the twisted PE fiber we used previously [259]. This unusual improvement in the recovered torque is attributed to the improvement in the tensile actuation of the precursor fiber, and will contribute to the tensile actuation of the artificial muscle. As can be seen from Fig. 5-4, the coiled muscle can generate up to $67.81 \pm 1.82\%$ actuation strain, which corresponds to an outstanding average NCTE of $(144.27 \pm 3.87) \times 10^{-4}℃^{-1}$. We thus have reason to believe that if we could fabricate a precursor fiber with even stronger 2W-SME, the tensile stroke of the artificial muscle made of such fiber can be further increased. It is reported that cross-linked poly(ε-caprolactone) 2W-SMP can generate reversible actuation stroke up to 70% and it thus can be a promising candidate [262].

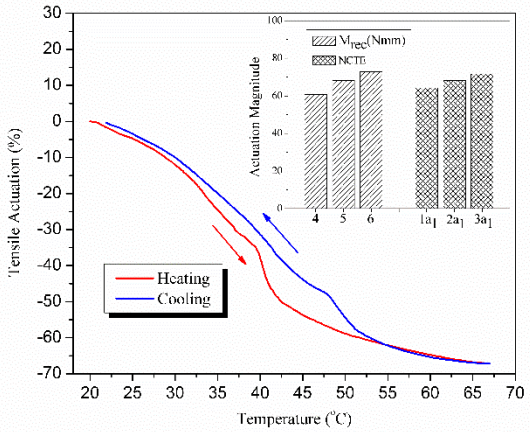

Figure 5-4 Tensile actuation of an artificial muscle actuating with a maximum load of 0.18N. The inset figure presents the predicted results using the mechanics model. Different recovered torque (4, 5 and 6 Nmm) and different NCTE values (1-, 2- and 3-fold of the NCTE for current sample) were used.

As an actuator, the specific work for this artificial muscle during contraction was $81 J/kg$, which is about twice that of the natural muscle [263], however much lower than that of the PE fiber we used previously ($520 J/kg$) [259]. The output work is mainly limited by the maximum force that can be sustained by our 2W-SMP. As can be seen from Table 5-1, the fabricated 2W-SMP fibers have relatively lower tensile moduli, as compared to PE fibers (about $2000 MPa$) [259]. Therefore, the coiled spring cannot resist much bending moment and may deform into a spring with a large pitch angle. Under this circumstance, the torsional actuation of the chiral fiber cannot be converted to the tensile actuation of the coiled muscle effectively. In addition, since melting is involved in each working cycle of the muscle actuation, the actuation force must be limited, which reduces the specific work; otherwise, viscoplastic behavior may reduce the reversibility of the muscle. Another limitation of this new type of artificial muscle is the energy conversion efficiency, which is defined as the ratio of the output mechanical energy to the input thermal energy (calculated via DSC curve). During contraction, only 0.05% of the input thermal energy was converted to mechanical work, which is lower than the PE fiber we used previously (0.3%) and those used in Haines et al.'s work [82]. The reason for this is again due to the low stiffness of the 2W-SMP, which leads to reduced mechanical work. With similar specific heat between PEVA and PE, the reduced work translates to reduced energy conversion efficiency. A possible approach to improve these performances is to add conductive reinforcement, such as carbon nanotubes (CNTs), which may increase the actuation stress and energy conversion efficiency. This will be a topic for our future studies.

5.4 Mechanics model for the artificial muscles

To further understand the working mechanism behind the hierarchical chiral structured artificial muscle, a simple mechanics model based on a consistent application of Castigliano's second theorem (CST) [232] is developed.

In Fig. 5-5(a), the coordinate systems, which include global Cartesian ($\{\boldsymbol{X_c}, \boldsymbol{Y_c}, \boldsymbol{Z_c}\}$), global cylindrical ($\{\boldsymbol{r_c}, \boldsymbol{\vartheta_c}, \boldsymbol{z_c}\}$), and local cylindrical coordinates ($\{\boldsymbol{r_f}, \boldsymbol{\vartheta_f}, \boldsymbol{z_f}\}$), and are used to analyze the hierarchical chiral artificial muscle, are presented.

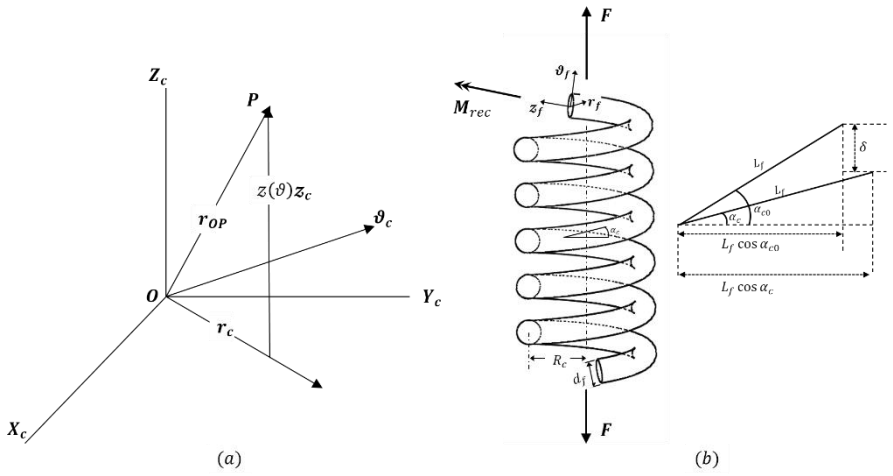

Figure 5-5 (a) The coordinate systems used to analyze the coiled spring. (b) Left scheme: free body diagram of the coiled artificial muscle, subjected to external applied force $\boldsymbol{F}$ and intrinsic recovered torque $\boldsymbol{M_{rec}}$. The chiral fiber has a diameter of d_f and a length of L_f. The coiled spring has n active coils, initial pitch angle α_{c0} (before loading) and final pitch angle of α_c (after loading). Right scheme: Kinematic relationship of the coiled muscle.

Throughout the working cycle, a constant load $\boldsymbol{F} = F\boldsymbol{Z_c}$ is applied to the coil. In addition, since both ends of the twisted fiber are tethered, a recovered torque $\boldsymbol{M_{rec}} = M_{rec}\boldsymbol{z_f}$ is acting along the axial direction in the twisted fiber. During the thermal cycle, the dimensional change in the axial direction of the fiber also contributes to the overall actuation of the coiled spring and cannot be neglected. In other words, the coiled artificial muscle is driven simultaneously by the externally applied load $\boldsymbol{F}$, the recovered torque $\boldsymbol{M_{rec}}$, along with the 2W-SME of the twisted fiber. Based on the free body diagram and the coordinate transformation between the global coordinate and the local coordinate, the external applied loads can be written as [233]:

$$\boldsymbol{F}_{app} = F_z\boldsymbol{z_f} + F_\vartheta\boldsymbol{\vartheta_f} \tag{5-4a}$$

$$\boldsymbol{M}_{app} = M_z\boldsymbol{z_f} + M_\vartheta\boldsymbol{\vartheta_f} \tag{5-4b}$$

with the normal force $F_z = F\sin\alpha_c$, shear force $F_\vartheta = F\cos\alpha_c$, torsional moment $M_z = -FR\cos\alpha_c + M_{rec}$ and bending moment $M_\vartheta = FR\sin\alpha_c$. These components are constant along the coil. By assuming that, at each step of temperature increment, the deformations along the fiber caused by the external load are infinitesimal, the complementary energy can be expressed as:

$$U^* = \int_0^{L_f}\left(\frac{M_z^2}{2\bar{G}_f J} + \frac{M_\vartheta^2}{2\bar{E}_f I} + \frac{F_z^2}{2\bar{E}_f A} + \frac{F_\vartheta^2}{2\bar{G}_f A}\right) dl$$
$$= L_f\left(\frac{M_z^2}{2\bar{G}_f J} + \frac{M_\vartheta^2}{2\bar{E}_f I} + \frac{F_z^2}{2\bar{E}_f A} + \frac{F_\vartheta^2}{2\bar{G}_f A}\right)$$

$$= \frac{1}{2} f_{11} F^2 - 2 f_{12} F M_{rec} + \frac{1}{2} f_{22} M_{rec}^2 \tag{5-5}$$

where $\bar{E}_f$ and $\bar{G}_f$ are the effective moduli of the twisted fiber. Taking the cross-section area of the fiber $A = \frac{\pi d^2}{4}$, the second moment $I = \frac{\pi d^4}{64}$, the polar moment of the area $J = \frac{\pi d^4}{32}$ and the radius of the coil $R = \frac{D}{2} = \frac{L_f \cos \alpha_c}{n\pi}$, f_{11}, f_{12} and f_{22} in Eq. 5-5 become:

$$f_{11} = \frac{8n}{\pi^3 d^4} \left(\frac{L_f}{n}\right)^3 \frac{\cos^4 \alpha_c}{\bar{G}} + \frac{8n}{\pi d^2} \left(\frac{L_f}{n}\right) \frac{\cos^2 \alpha_c}{2\bar{G}} + \frac{8n}{\pi^3 d^4} \left(\frac{L_f}{n}\right)^3 \frac{2 \sin^2 \alpha_c \cos^2 \alpha_c}{\bar{E}} + \frac{8n}{\pi d^2} \left(\frac{L_f}{n}\right) \frac{\sin^2 \alpha_c}{2\bar{E}} \tag{5-6a}$$

$$f_{12} = \frac{8n}{\pi^2 d^4} \left(\frac{L_f}{n}\right)^2 \frac{\cos^2 \alpha_c}{\bar{G}} \tag{5-6b}$$

$$f_{22} = \frac{32}{\pi d^4} \frac{L_f}{\bar{G}} \tag{5-6c}$$

Then, the displacement δ of a helical spring subjected to applied force F and recovered torque M_{rec} is directly found by applying CST [234]:

$$\delta = f_{11} F - f_{12} M_{rec} \tag{5-7}$$

The displacement can also be expressed as a function of the pitch angle α_c using the kinematic relationship:

$$\delta = L_f (\sin \alpha_c - \sin \alpha_{c0}) \tag{5-8}$$

Using Eqs. 5-7 and 5-8, the pitch angle $\alpha_c(T)$, hence the displacement $\delta(T)$ can be expressed in terms of $d, L_f, \bar{G}_f, \bar{E}_f$ and M_{rec} Here in this work, we only focus on the actuation magnitude R_{act}^{AM} within one cycle for the artificial muscle (AM). Therefore, only the values for $d, L_f, \bar{G}_f, \bar{E}_f$ and M_{rec} at T_{low} and T_{high} are needed. Notice that, in the 2W-SMP fiber, the final value for L_f at T_{high} also depends on the applied load along the fiber ($F_z = F \sin \alpha_c$). According to the experimental results in Fig. 5-3(b), we have:

$$L_f(T_{high}) = L_{f0} - \bar{\alpha}_{act}(\sigma_z) \times \Delta T \times L_{f0} \tag{5-9}$$

where $\bar{\alpha}_{act}(\sigma_z)$ depends linearly on the $\sigma_z = \frac{4F_z}{\pi d^2}$:

$$\bar{\alpha}_{act}(\sigma_z) = a_1' \sigma_z + b_1' = a_1' \frac{4F}{\pi d^2} \sin \alpha_c + b_1' \tag{5-10}$$

take Eq. 5-10 into Eq. 5-9, $L_f(T_{high})$ can be expressed as:

$$L_f(T_{high}) = \frac{a_1 \sin \alpha_c}{d^2} + b_1 \tag{5-11}$$

where $a_1 = -\frac{4F}{\pi} a_1' \times \Delta T \times L_{f0}$, $b_1 = b_1'$.

Take Eq. 5-10 back into Eq. 5-7, together with Eq. 5-8, a 7th order polynomial equation of $\sin \alpha_c$ can be obtained and finally, the actuation magnitude R_{act}^{AM} can be obtained using:

$$\varepsilon_{act}^{AM} = \frac{L_f(T_{low}) \sin \alpha_c(T_{low}) - L_f(T_{high}) \sin \alpha_c(T_{high})}{L_f(T_{low}) \sin \alpha_c(T_{low})} \tag{5-12}$$

The model was coded and implemented into the MATLAB program. The theoretical value for ε_{act}^{AM} is 64.17%, which is in good agreement with the experimental value (67.81%). A parametric study in the inset of Fig. 5-4 indicates the sensitivity to both the recovered torque and the NCTE. The study indicates that both parameters have a positive impact on the tensile actuation of the muscle. From the above analysis, it is seen that the mechanics model captures the fundamental mechanisms, and can help researchers understand the working principles of the artificial muscle and can facilitate future material design.

5.5 Conclusion

In this work, a hierarchical chiral structured artificial muscle has been fabricated using two-way shape memory polymer fiber. Experimentally, we have presented the two-way shape memory effect of the precursor and twisted (chiral) fibers that eventually leads to the improvement in the axial actuation of the coiled artificial muscle. Theoretically, a mechanics model based on Castigliano's second theorem (CST) has been proposed and the calculated result is consistent with the experimental result. The model prove the significance of the 2W-SME and the recovered torque on tensile actuation, and can be used as a guidance for future study.

It is noted that the artificial muscles still have some limitations in terms of energy efficiency, such as specific work and energy conversion efficiency. It is envisioned that, by adding conductive reinforcement such as carbon nanotubes (CNTs) into 2W-SMPs, for example grafting PEVA or poly(ε-caprolatone) (PCL, which has much higher 2W-SME than that of PEVA) chains onto the CNTs, the specific work and energy conversion efficiency may be enhanced, without the penalty of low actuation strain. This will be a topic for future studies.

CHAPTER 6SUMMARY AND FUTURE WORKS

6.1 Summary

In this dissertation, the application of smart polymers as actuators was investigated, with focuses on shape memory polymers and twisted-then-coiled artificial muscles. In Chapter 1, a brief introduction on polymeric actuators and a literature review on the shape memory polymers and artificial muscles were conducted

In Chapter 2, a temperature and rate dependent thermomechanical constitutive model based on phase evolution for the amorphous one-way shape memory polymers was developed. The model successfully provided the phase transition model with physics explanation through thermodynamic law and statistical mechanics. The model reasonably captured the shape fixity and shape recovery process, governed by clear physics. The parametric study of the model predicted that the dynamic heterogeneous domain size distribution, the external mechanical work and the heating rate had a significant effect impact on the shape memory behavior. While this work focused on amorphous SMPs, the principle and procedure can be easily extended to modeling of semi-crystalline SMPs, and even polymeric artificial muscles with similar phase transitions.

In Chapter 3, a 3D constitutive model was developed based on the multiple natural configurations framework for the *true* 2W-SME. The model has been validated against the experimental results for the cPEVA based 2W-SMP and shown good agreement. The model proved that the internal stress is stored during the programming procedure. This internal stress contributes to 2W-SME from two aspects. First, anisotropy can be introduced to crystalline phases formed during crystallization process and second, crystallization kinetics in polymer can be greatly enhanced by deformation. Higher programming stress can lead to higher stored internal stress and ends up with better *true* 2W-SME performance. We predicted that if a SMP does not exhibit dramatic viscoplastic deformation and can stores a sufficient amount of internal tensile stress, it can be made into an *advanced* 2W-SMP that can generate actuation even under compression. Finally, we believe that, if 1W-SMPs have sufficient tensile strength and enough ultimate tensile strain, they have a potential to be transformed into 2W-SMPs, as long as an anisotropic network can be built up either through a sufficient external tensile load (*quasi* 2W-SME) or through a sufficient stored internal tensile stress by tensile programming (*true* 2W-SME).

In Chapter 4, a multi-scale modeling framework based on a top-down analysis was developed for the actuation response of the polymeric artificial muscles. The model was validated against the experimental results for the polyethylene copolymer fiber based muscles. The physical origin and dependence of the torsional actuation of the twisted fiber and the tensile actuation of the twisted-then-coiled spring on temperature have been elaborated and reproduced. A parametric study was further conducted to help future design and optimization of such innovative artificial muscles.

In Chapter 5, we developed a new type of twisted-then-coiled polymeric artificial muscle using two-way shape memory polymer fibers. Experimentally, we have presented the two-way shape memory effect of the precursor and twisted (chiral) fibers that eventually leads to the improvement in the axial actuation of the coiled artificial muscle. Theoretically, a mechanics model based on Castigliano's second theorem (CST) has been proposed and the calculated result is consistent with

the experimental result. The model prove the significance of the 2W-SME and the recovered torque on tensile actuation, and can be used as a guidance for future study.

6.2 Future works

Shape memory polymers and twisted-then-coiled artificial muscles are relatively new topics in the polymeric actuator field. Much more research works are necessary to gain a thorough understanding of their working mechanism. The following recommendations are made for possible future research:

(1) According to our model for the amorphous shape memory polymers, the external mechanical work plays a significant role in shape memory behavior. Therefore, this model can be extended to the cold programmed shape memory polymers, which requires a fully understanding.

(2) According to the conclusion in the two-way shape memory polymer model, the *advanced* 2W-SMP is possible. Therefore, seeking the appropriate candidates can be one of the future works.

(3) It is noted that the artificial muscles still have some limitations in terms of energy efficiency, such as specific work and energy conversion efficiency. It is envisioned that, by adding conductive reinforcement such as carbon nanotubes (CNTs) into 2W-SMPs, for example grafting PEVA or poly(ε-caprolatone) (PCL, which has much higher 2W-SME than that of PEVA) chains onto the CNTs, the specific work and energy conversion efficiency may be enhanced, without the penalty of low actuation strain. This can be a topic for future studies.

(4) Polymeric actuators can be stimulated by various stimulus, such as heat, electric or magnetic, and humidity. Modeling of the corresponding polymeric actuators is either at the initial stage or in need of improvement, and thus can be a future topic.

REFERENCES

[1] Randhawa JS, Laflin KE, Seelam N, Gracias DH. Chemically Controlled Miniature Devices: Microchemomechanical Systems (Adv. Funct. Mater. 13/2011). *Advanced Functional Materials,* 21: (2011).

[2] Ionov L. Biomimetic Hydrogel‐Based Actuating Systems. *Advanced Functional Materials,* 23: 4555-4570, (2013).

[3] Geryak R, Tsukruk VV. Reconfigurable and actuating structures from soft materials. *Soft Matter,* 10: 1246-1263, (2014).

[4] Ionov L. Polymeric actuators. *Langmuir,* 31: 5015-5024, (2014).

[5] Mirfakhrai T, Madden JD, Baughman RH. Polymer artificial muscles. *Materials Today,* 10: 30-38, (2007).

[6] Osada Y, Okuzaki H, Hori H. A polymer gel with electrically driven motility. *Nature,* 355: 242, (1992).

[7] Liu Z, Calvert P. Multilayer hydrogels as muscle‐like actuators. *Advanced Materials,* 12: 288-291, (2000).

[8] Jager EW, Smela E, Inganäs O. Microfabricating conjugated polymer actuators. *Science,* 290: 1540-1545, (2000).

[9] Wen H, Zhang W, Weng Y, Hu Z. Photomechanical bending of linear azobenzene polymer. *RSC Advances,* 4: 11776-11781, (2014).

[10] Zhang Y, Ionov L. Actuating Porous Polyimide Films. *ACS applied materials & interfaces,* 6: 10072-10077, (2014).

[11] Stuart MAC, Huck WT, Genzer J, Müller M, Ober C, Stamm M, Sukhorukov GB, Szleifer I, Tsukruk VV, Urban M. Emerging applications of stimuli-responsive polymer materials. *Nature Materials,* 9: 101-113, (2010).

[12] Bozlar M, Punckt C, Korkut S, Zhu J, Chiang Foo C, Suo Z, Aksay IA. Dielectric elastomer actuators with elastomeric electrodes. *Applied Physics Letters,* 101: 091907, (2012).

[13] Lendlein A, Kelch S. Shape‐memory polymers. *Angewandte Chemie International Edition,* 41: 2034-2057, (2002).

[14] Yu Y, Nakano M, Ikeda T. Photomechanics: directed bending of a polymer film by light. *Nature,* 425: 145-145, (2003).

[15] Chung T, Romo-Uribe A, Mather PT. Two-way reversible shape memory in a semicrystalline network. *Macromolecules,* 41: 184-192, (2008).

[16] Xie T, Li J, Zhao Q. Hidden Thermoreversible Actuation Behavior of Nafion and Its Morphological Origin. *Macromolecules,* 47: 1085-1089, (2014).

[17] Azam A, Laflin KE, Jamal M, Fernandes R, Gracias DH. Self-folding micropatterned polymeric containers. *Biomedical Microdevices,* 13: 51-58, (2011).

[18] Yoo J-W, Mitragotri S. Polymer particles that switch shape in response to a stimulus. *Proceedings of the National Academy of Sciences,* 107: 11205-11210, (2010).

[19] Singamaneni S, LeMieux MC, Lang HP, Gerber C, Lam Y, Zauscher S, Datskos PG, Lavrik NV, Jiang H, Naik RR. Bimaterial microcantilevers as a hybrid sensing platform. *Advanced Materials,* 20: 653-680, (2008).

[20] Dong L, Agarwal AK, Beebe DJ, Jiang H. Adaptive liquid microlenses activated by stimuli-responsive hydrogels. *Nature,* 442: 551-554, (2006).

[21] Hu J, Meng H, Li G, Ibekwe SI. A review of stimuli-responsive polymers for smart textile applications. *Smart Materials and Structures,* 21: 053001, (2012).

[22] Dietsch B, Tong T. A review-: Features and benefits of shape memory polymers (SMPs). *Journal of Advanced Materials,* 39: 3-12, (2007).

[23] Ratna D, Karger-Kocsis J. Recent advances in shape memory polymers and composites: a review. *Journal of Materials Science,* 43: 254-269, (2008).

[24] Leng J, Lu H, Liu Y, Huang WM, Du S. Shape-memory polymers—a class of novel smart materials. *MRS Bulletin,* 34: 848-855, (2009).

[25] Mather PT, Luo X, Rousseau IA. Shape memory polymer research. *Annual Review of Materials Research,* 39: 445-471, (2009).

[26] Huang W, Ding Z, Wang C, Wei J, Zhao Y, Purnawali H. Shape memory materials. *Materials Today,* 13: 54-61, (2010).

[27] Leng J, Lan X, Liu Y, Du S. Shape-memory polymers and their composites: stimulus methods and applications. *Progress in Materials Science,* 56: 1077-1135, (2011).

[28] Hu J, Zhu Y, Huang H, Lu J. Recent advances in shape–memory polymers: Structure, mechanism, functionality, modeling and applications. *Progress in Polymer Science,* 37: 1720-1763, (2012).

[29] Meng H, Li G. A review of stimuli-responsive shape memory polymer composites. *Polymer,* 54: 2199-2221, (2013).

[30] Zhao Q, Qi HJ, Xie T. Recent Progress in Shape Memory Polymer: New Behavior, Enabling Materials, and Mechanistic Understanding. *Progress in Polymer Science,* (2015).

[31] Behl M, Lendlein A. Shape-memory polymers. *Materials Today,* 10: 20-28, (2007).

[32] Liu C, Qin H, Mather P. Review of progress in shape-memory polymers. *Journal of Materials Chemistry,* 17: 1543-1558, (2007).

[33] Xie T. Tunable polymer multi-shape memory effect. *Nature,* 464: 267-270, (2010).

[34] Yu K, Xie T, Leng J, Ding Y, Qi HJ. Mechanisms of multi-shape memory effects and associated energy release in shape memory polymers. *Soft Matter,* 8: 5687-5695, (2012).

[35] Lendlein A, Jiang H, Jünger O, Langer R. Light-induced shape-memory polymers. *Nature,* 434: 879-882, (2005).

[36] Scott TF, Schneider AD, Cook WD, Bowman CN. Photoinduced plasticity in cross-linked polymers. *Science,* 308: 1615-1617, (2005).

[37] Buckley PR, McKinley GH, Wilson TS, Small W, Benett WJ, Bearinger JP, McElfresh MW, Maitland DJ. Inductively heated shape memory polymer for the magnetic actuation of medical devices. *Biomedical Engineering, IEEE Transactions on,* 53: 2075-2083, (2006).

[38] Schmidt AM. Electromagnetic activation of shape memory polymer networks containing magnetic nanoparticles. *Macromolecular Rapid Communications,* 27: 1168-1172, (2006).

[39] Huang W, Yang B, An L, Li C, Chan Y. Water-driven programmable polyurethane shape memory polymer: demonstration and mechanism. *Applied Physics Letters,* 86: 114105, (2005).

[40] Chae Jung Y, Hwa So H, Whan Cho J. Water‐Responsive Shape Memory Polyurethane Block Copolymer Modified with Polyhedral Oligomeric Silsesquioxane. *Journal of Macromolecular Science, Part B,* 45: 453-461, (2006).

[41] Vernon LB, Vernon HM, *Process of manufacturing articles of thermoplastic synthetic resins,* 1941, Google Patents.

[42] Hitov JJ, Rainer WC, Redding EM, Sloan AW, Stewart WD, *Polyethylene product and process,* 1964, Google Patents.

[43] Xu W, Li G. Thermoviscoplastic modeling and testing of shape memory polymer based self-healing syntactic foam programmed at glassy temperature. *Journal of Applied Mechanics,* 78: 061017, (2011).

[44] Li G, Xu W. Thermomechanical behavior of thermoset shape memory polymer programmed by cold-compression: testing and constitutive modeling. *Journal of the Mechanics and Physics of Solids,* 59: 1231-1250, (2011).

[45] Li G, Shojaei A. A viscoplastic theory of shape memory polymer fibres with application to self-healing materials. *Proceedings of the Royal Society A: Mathematical, Physical and Engineering Science,* 468: 2319-2346, (2012).

[46] Li G. Self-healing Composites: Shape Memory Polymer Based Structures, John Wiley & Sons, (2014).

[47] Li G, Nettles D. Thermomechanical characterization of a shape memory polymer based self-repairing syntactic foam. *Polymer,* 51: 755-762, (2010).

[48] Bellin I, Kelch S, Langer R, Lendlein A. Polymeric triple-shape materials. *Proceedings of the National Academy of Sciences,* 103: 18043-18047, (2006).

[49] Xie T, Xiao X, Cheng YT. Revealing triple‐shape memory effect by polymer bilayers. *Macromolecular Rapid Communications,* 30: 1823-1827, (2009).

[50] Bai Y, Jiang C, Wang Q, Wang T. Multi‐Shape‐Memory Property Study of Novel Poly (ε‐Caprolactone)/Ethyl Cellulose Polymer Networks. *Macromolecular Chemistry and Physics,* 214: 2465-2472, (2013).

[51] Chen S, Mo F, Yang Y, Stadler FJ, Chen S, Yang H, Ge Z. Development of zwitterionic polyurethanes with multi-shape memory effects and self-healing properties. *Journal of Materials Chemistry A,* 3: 2924-2933, (2015).

[52] Chen S, Mo F, Stadler FJ, Chen S, Ge Z, Zhuo H. Development of zwitterionic copolymers with multi-shape memory effects and moisture-sensitive shape memory effects. *Journal of Materials Chemistry B,* 3: 6645-6655, (2015).

[53] Hager MD, Bode S, Weber C, Schubert US. Shape memory polymers: Past, present and future developments. *Progress in Polymer Science,* (2015).

[54] Behl M, Kratz K, Noechel U, Sauter T, Lendlein A. Temperature-memory polymer actuators. *Proc. Natl. Acad. Sci. U.S.A.,* 110: 12555-12559, (2013).

[55] Behl M, Kratz K, Zotzmann J, Nöchel U, Lendlein A. Reversible Bidirectional Shape-Memory Polymers. *Advanced Materials,* 25: 4466-4469, (2013).

[56] Stroganov V, Al-Hussein M, Sommer J-U, Janke A, Zakharchenko S, Ionov L. Reversible thermosensitive biodegradable polymeric actuators based on confined crystallization. *Nano Letters,* 15: 1786-1790, (2015).

[57] Yang Q, Fan J, Li G. Artificial muscles made of chiral two-way shape memory polymer fibers. *Applied Physics Letters,* 109: 183701, (2016).

[58] Lee KM, Knight PT, Chung T, Mather PT. Polycaprolactone− POSS Chemical/Physical Double Networks. *Macromolecules,* 41: 4730-4738, (2008).

[59] Li J, Rodgers WR, Xie T. Semi-crystalline two-way shape memory elastomer. *Polymer,* 52: 5320-5325, (2011).

[60] Raquez JM, Vanderstappen S, Meyer F, Verge P, Alexandre M, Thomassin JM, Jérôme C, Dubois P. Design of Cross‐Linked Semicrystalline Poly (ε‐caprolactone)‐Based Networks with One‐Way and Two‐Way Shape‐Memory Properties through Diels–Alder Reactions. *Chemistry-A European Journal,* 17: 10135-10143, (2011).

[61] Pandini S, Passera S, Messori M, Paderni K, Toselli M, Gianoncelli A, Bontempi E, Ricco T. Two-way reversible shape memory behaviour of crosslinked poly (ε-caprolactone). *Polymer,* 53: 1915-1924, (2012).

[62] Pandini S, Baldi F, Paderni K, Messori M, Toselli M, Pilati F, Gianoncelli A, Brisotto M, Bontempi E, Ricco T. One-way and two-way shape memory behaviour of semi-crystalline networks based on sol–gel cross-linked poly (ε-caprolactone). *Polymer,* 54: 4253-4265, (2013).

[63] Pandini S, Dioni D, Paderni K, Messori M, Toselli M, Bontempi E, Riccò T. The two-way shape memory behaviour of crosslinked poly (ε-caprolactone) systems with largely varied network density. *Journal of Intelligent Material Systems and Structures,* 1045389X15591384, (2015).

[64] Ma L, Zhao J, Wang X, Chen M, Liang Y, Wang Z, Yu Z, Hedden RC. Effects of carbon black nanoparticles on two-way reversible shape memory in crosslinked polyethylene. *Polymer,* 56: 490-497, (2015).

[65] Zhou J, Turner SA, Brosnan SM, Li Q, Carrillo J-MY, Nykypanchuk D, Gang O, Ashby VS, Dobrynin AV, Sheiko SS. Shapeshifting: reversible shape memory in semicrystalline elastomers. *Macromolecules,* 47: 1768-1776, (2014).

[66] Lu L, Li G. One-way multi-shape memory effect and tunable two-way shape memory effect of ionomer poly (ethylene-co-methacrylic acid). *ACS applied materials & interfaces,* (2016).

[67] Kolesov I, Dolynchuk O, Jehnichen D, Reuter U, Stamm M, Radusch H-J. Changes of Crystal Structure and Morphology during Two-Way Shape-Memory Cycles in Cross-Linked Linear and Short-Chain Branched Polyethylenes. *Macromolecules,* 48: 4438-4450, (2015).

[68] Dolynchuk O, Kolesov I, Radusch HJ. Thermodynamic description and modeling of two‐way shape‐memory effect in crosslinked semicrystalline polymers. *Polymers for Advanced Technologies,* 25: 1307-1314, (2014).

[69] Gaylord R. A theory of the stress‐induced crystallization of crosslinked polymeric networks. *Journal of Polymer Science: Polymer Physics Edition,* 14: 1827-1837, (1976).

[70] Meng Y, Jiang J, Anthamatten M. Shape Actuation via Internal Stress-Induced Crystallization of Dual-Cure Networks. *ACS Macro Letters,* 4: 115-118, (2015).

[71] Zhang Q, Bharti V, Zhao X. Giant electrostriction and relaxor ferroelectric behavior in electron-irradiated poly (vinylidene fluoride-trifluoroethylene) copolymer. *Science,* 280: 2101-2104, (1998).

[72] Pelrine R, Kornbluh RD, Pei Q, Stanford S, Oh S, Eckerle J, Full RJ, Rosenthal MA, Meijer K. Dielectric elastomer artificial muscle actuators: toward biomimetic motion. in *SPIE's 9th Annual International Symposium on Smart Structures and Materials*. 2002. International Society for Optics and Photonics.

[73] Ohm C, Brehmer M, Zentel R. Liquid crystalline elastomers as actuators and sensors. *Advanced Materials,* 22: 3366-3387, (2010).

[74] Chou C-P, Hannaford B. Measurement and modeling of McKibben pneumatic artificial muscles. *Robotics and Automation, IEEE Transactions on,* 12: 90-102, (1996).

[75] Daerden F, Lefeber D. Pneumatic artificial muscles: actuators for robotics and automation. *European journal of mechanical and environmental engineering,* 47: 11-21, (2002).

[76] Baughman R. Conducting polymer artificial muscles. *Synthetic Metals,* 78: 339-353, (1996).

[77] Shahinpoor M, Bar-Cohen Y, Simpson J, Smith J. Ionic polymer-metal composites (IPMCs) as biomimetic sensors, actuators and artificial muscles-a review. *Smart Materials and Structures,* 7: R15, (1998).

[78] Lima MD, Li N, De Andrade MJ, Fang S, Oh J, Spinks GM, Kozlov ME, Haines CS, Suh D, Foroughi J. Electrically, chemically, and photonically powered torsional and tensile actuation of hybrid carbon nanotube yarn muscles. *Science,* 338: 928-932, (2012).

[79] Wayman C. Some applications of shape-memory alloys. *JOM Journal of the Minerals Metals and Materials Society,* 32: 129-137, (1980).

[80] Madden JD, Vandesteeg N, Anquetil P, Madden PG, Takshi A, Pytel RZ, Lafontaine SR, Wieringa P, Hunter IW. Artificial muscle technology: physical principles and naval prospects. *Oceanic Engineering, IEEE Journal of,* 29: 706-728, (2004).

[81] Mirvakili SM, Pazukha A, Sikkema W, Sinclair CW, Spinks GM, Baughman RH, Madden JD. Niobium nanowire yarns and their application as artificial muscles. *Advanced Functional Materials,* 23: 4311-4316, (2013).

[82] Haines CS, Lima MD, Li N, Spinks GM, Foroughi J, Madden JD, Kim SH, Fang S, de Andrade MJ, Göktepe F. Artificial muscles from fishing line and sewing thread. *Science,* 343: 868-872, (2014).

[83] Aziz S, Naficy S, Foroughi J, Brown HR, Spinks GM. Characterisation of torsional actuation in highly twisted yarns and fibres. *Polymer Testing,* 46: 88-97, (2015).

[84] Cherubini A, Moretti G, Vertechy R, Fontana M. Experimental characterization of thermally-activated artificial muscles based on coiled nylon fishing lines. *AIP Advances,* 5: 067158, (2015).

[85] Moretti G, Cherubini A, Vertechy R, Fontana M. Experimental characterization of a new class of polymeric-wire coiled transducers. in *SPIE Smart Structures and Materials+Nondestructive Evaluation and Health Monitoring*. 2015. International Society for Optics and Photonics.

[86] McEvoy M, Correll N. Materials that couple sensing, actuation, computation, and communication. *Science,* 347: 1261689, (2015).

[87] Zhang P, Li G. Healing-on-demand composites based on polymer artificial muscle. *Polymer,* 64: 29-38, (2015).

[88] Zhang P, Li G. Fishing line artificial muscle reinforced composite for impact mitigation and on-demand damage healing. *Journal of Composite Materials,* 50: 4235-4249, (2016).

[89] Yip MC, Niemeyer G. High-performance robotic muscles from conductive nylon sewing thread. in *Robotics and Automation (ICRA), 2015 IEEE International Conference on*. 2015. IEEE.

[90] Foroughi J, Spinks GM, Wallace GG, Oh J, Kozlov ME, Fang S, Mirfakhrai T, Madden JD, Shin MK, Kim SJ. Torsional carbon nanotube artificial muscles. *Science,* 334: 494-497, (2011).

[91] Buckley C, Prisacariu C, Caraculacu A. Novel triol-crosslinked polyurethanes and their thermorheological characterization as shape-memory materials. *Polymer,* 48: 1388-1396, (2007).

[92] Lin J, Chen L. Shape‐memorized crosslinked ester‐type polyurethane and its mechanical viscoelastic model. *Journal of Applied Polymer Science,* 73: 1305-1319, (1999).

[93] Tobushi H, Hashimoto T, Hayashi S, Yamada E. Thermomechanical constitutive modeling in shape memory polymer of polyurethane series. *Journal of Intelligent Material Systems and Structures,* 8: 711-718, (1997).

[94] Tobushi H, Okumura K, Hayashi S, Ito N. Thermomechanical constitutive model of shape memory polymer. *Mechanics of Materials,* 33: 545-554, (2001).

[95] Balogun O, Mo C. Shape memory polymers: three-dimensional isotropic modeling. *Smart Materials and Structures,* 23: 045008, (2014).

[96] Ghosh P, Srinivasa A. Development of a finite strain two-network model for shape memory polymers using QR decomposition. *International Journal of Engineering Science,* 81: 177-191, (2014).

[97] Diani J, Liu Y, Gall K. Finite strain 3D thermoviscoelastic constitutive model for shape memory polymers. *Polymer Engineering & Science,* 46: 486-492, (2006).

[98] Nguyen TD, Jerry Qi H, Castro F, Long KN. A thermoviscoelastic model for amorphous shape memory polymers: incorporating structural and stress relaxation. *Journal of the Mechanics and Physics of Solids,* 56: 2792-2814, (2008).

[99] Chen X, Nguyen TD. Influence of thermoviscoelastic properties and loading conditions on the recovery performance of shape memory polymers. *Mechanics of Materials,* 43: 127-138, (2011).

[100] Westbrook KK, Kao PH, Castro F, Ding Y, Qi HJ. A 3D finite deformation constitutive model for amorphous shape memory polymers: a multi-branch modeling approach for nonequilibrium relaxation processes. *Mechanics of Materials,* 43: 853-869, (2011).

[101] Diani J, Gilormini P, Frédy C, Rousseau I. Predicting thermal shape memory of crosslinked polymer networks from linear viscoelasticity. *International Journal of Solids and Structures,* 49: 793-799, (2012).

[102] Ge Q, Yu K, Ding Y, Qi HJ. Prediction of temperature-dependent free recovery behaviors of amorphous shape memory polymers. *Soft Matter,* 8: 11098-11105, (2012).

[103] Xiao R, Choi J, Lakhera N, Yakacki CM, Frick CP, Nguyen TD. Modeling the glass transition of amorphous networks for shape-memory behavior. *Journal of the Mechanics and Physics of Solids,* 61: 1612-1635, (2013).

[104] Ge Q, Luo X, Iversen CB, Mather PT, Dunn ML, Qi HJ. Mechanisms of triple-shape polymeric composites due to dual thermal transitions. *Soft Matter,* 9: 2212-2223, (2013).

[105] Ge Q, Luo X, Iversen CB, Nejad HB, Mather PT, Dunn ML, Qi HJ. A finite deformation thermomechanical constitutive model for triple shape polymeric composites based on dual thermal transitions. *International Journal of Solids and Structures,* 51: 2777-2790, (2014).

[106] Yu K, Ge Q, Qi HJ. Reduced time as a unified parameter determining fixity and free recovery of shape memory polymers. *Nature communications,* 5: (2014).

[107] Diani J, Gall K. Molecular dynamics simulations of the shape-memory behaviour of polyisoprene. *Smart Materials and Structures,* 16: 1575, (2007).

[108] Zhang C, Hu J, Chen S, Ji F. Theoretical study of hydrogen bonding interactions on MDI-based polyurethane. *Journal of Molecular Modeling,* 16: 1391-1399, (2010).

[109] Shojaei A, Li G. Viscoplasticity analysis of semicrystalline polymers: a multiscale approach within micromechanics framework. *International Journal of Plasticity,* 42: 31-49, (2013).

[110] Shojaei A, Li G. Thermomechanical constitutive modelling of shape memory polymer including continuum functional and mechanical damage effects. *Proceedings of the Royal Society A: Mathematical, Physical and Engineering Science,* 470: 20140199, (2014).

[111] Liu Y, Gall K, Dunn ML, Greenberg AR, Diani J. Thermomechanics of shape memory polymers: uniaxial experiments and constitutive modeling. *International Journal of Plasticity,* 22: 279-313, (2006).

[112] Baghani M, Naghdabadi R, Arghavani J, Sohrabpour S. A thermodynamically-consistent 3D constitutive model for shape memory polymers. *International Journal of Plasticity,* 35: 13-30, (2012).

[113] Chen Y-C, Lagoudas DC. A constitutive theory for shape memory polymers. Part I: Large deformations. *Journal of the Mechanics and Physics of Solids,* 56: 1752-1765, (2008).

[114] Chen Y-C, Lagoudas DC. A constitutive theory for shape memory polymers. Part II: a linearized model for small deformations. *Journal of the Mechanics and Physics of Solids,* 56: 1766-1778, (2008).

[115] Gilormini P, Diani J. On modeling shape memory polymers as thermoelastic two-phase composite materials. *Comptes Rendus Mécanique,* 340: 338-348, (2012).

[116] Guo X, Liu L, Zhou B, Liu Y, Leng J. Constitutive model for shape memory polymer based on the viscoelasticity and phase transition theories. *Journal of Intelligent Material Systems and Structures,* 1045389X15571380, (2015).

[117] Kafka V. Shape memory polymers: a mesoscale model of the internal mechanism leading to the SM phenomena. *International Journal of Plasticity,* 24: 1533-1548, (2008).

[118] Kazakevičiūtė-Makovska R, Steeb H, Aydin AÖ. On the evolution law for the frozen fraction in linear theories of shape memory polymers. *Archive of Applied Mechanics,* 82: 1103-1115, (2012).

[119] Kim JH, Kang TJ, Yu W-R. Thermo-mechanical constitutive modeling of shape memory polyurethanes using a phenomenological approach. *International Journal of Plasticity,* 26: 204-218, (2010).

[120] Long KN, Dunn ML, Qi HJ. Mechanics of soft active materials with phase evolution. *International Journal of Plasticity,* 26: 603-616, (2010).

[121] Pieczyska E, Maj M, Kowalczyk-Gajewska K, Staszczak M, Gradys A, Majewski M, Cristea M, Tobushi H, Hayashi S. Thermomechanical properties of polyurethane shape memory polymer–experiment and modelling. *Smart Materials and Structures,* 24: 045043, (2015).

[122] Qi HJ, Nguyen TD, Castro F, Yakacki CM, Shandas R. Finite deformation thermo-mechanical behavior of thermally induced shape memory polymers. *Journal of the Mechanics and Physics of Solids,* 56: 1730-1751, (2008).

[123] Reese S, Böl M, Christ D. Finite element-based multi-phase modelling of shape memory polymer stents. *Computer Methods in Applied Mechanics and Engineering,* 199: 1276-1286, (2010).

[124] Scalet G, Auricchio F, Bonetti E, Castellani L, Ferri D, Pachera M, Scavello F. An experimental, theoretical and numerical investigation of shape memory polymers. *International Journal of Plasticity,* 67: 127-147, (2015).

[125] Volk BL, Lagoudas DC, Maitland DJ. Characterizing and modeling the free recovery and constrained recovery behavior of a polyurethane shape memory polymer. *Smart Materials and Structures,* 20: 094004, (2011).

[126] Wang Z, Li D, Xiong Z, Chang R. Modeling thermomechanical behaviors of shape memory polymer. *Journal of Applied Polymer Science,* 113: 651-656, (2009).

[127] Xu W, Li G. Constitutive modeling of shape memory polymer based self-healing syntactic foam. *International Journal of Solids and Structures,* 47: 1306-1316, (2010).

[128] Auricchio F, Reali A, Stefanelli U. A three-dimensional model describing stress-induced solid phase transformation with permanent inelasticity. *International Journal of Plasticity,* 23: 207-226, (2007).

[129] Dachkovski S, Böhm M. Finite thermoplasticity with phase changes based on isomorphisms. *International Journal of Plasticity,* 20: 323-334, (2004).

[130] Hassan T, Taleb L, Krishna S. Influence of non-proportional loading on ratcheting responses and simulations by two recent cyclic plasticity models. *International Journal of Plasticity,* 24: 1863-1889, (2008).

[131] Levitas VI, Ozsoy IB. Micromechanical modeling of stress-induced phase transformations. Part 1. Thermodynamics and kinetics of coupled interface propagation and reorientation. *International Journal of Plasticity,* 25: 239-280, (2009).

[132] Levitas VI, Ozsoy IB. Micromechanical modeling of stress-induced phase transformations. Part 2. Computational algorithms and examples. *International Journal of Plasticity,* 25: 546-583, (2009).

[133] Moumni Z, Zaki W, Nguyen QS. Theoretical and numerical modeling of solid–solid phase change: application to the description of the thermomechanical behavior of shape memory alloys. *International Journal of Plasticity,* 24: 614-645, (2008).

[134] Müller C, Bruhns O. A thermodynamic finite-strain model for pseudoelastic shape memory alloys. *International Journal of Plasticity,* 22: 1658-1682, (2006).

[135] Popov P, Lagoudas DC. A 3-D constitutive model for shape memory alloys incorporating pseudoelasticity and detwinning of self-accommodated martensite. *International Journal of Plasticity,* 23: 1679-1720, (2007).

[136] Reese S, Christ D. Finite deformation pseudo-elasticity of shape memory alloys–constitutive modelling and finite element implementation. *International Journal of Plasticity,* 24: 455-482, (2008).

[137] Thamburaja P, Ekambaram R. Coupled thermo-mechanical modelling of bulk-metallic glasses: theory, finite-element simulations and experimental verification. *Journal of the Mechanics and Physics of Solids,* 55: 1236-1273, (2007).

[138] Thamburaja P, Nikabdullah N. A macroscopic constitutive model for shape-memory alloys: theory and finite-element simulations. *Computer Methods in Applied Mechanics and Engineering,* 198: 1074-1086, (2009).

[139] Wang X, Xu B, Yue Z. Micromechanical modelling of the effect of plastic deformation on the mechanical behaviour in pseudoelastic shape memory alloys. *International Journal of Plasticity,* 24: 1307-1332, (2008).

[140] Hill R. A self-consistent mechanics of composite materials. *Journal of the Mechanics and Physics of Solids,* 13: 213-222, (1965).

[141] Hori M, Nemat-Nasser S. Double-inclusion model and overall moduli of multi-phase composites. *Mechanics of Materials,* 14: 189-206, (1993).

[142] Hu G, Weng G. Some reflections on the Mori-Tanaka and Ponte Castaneda-Willis methods with randomly oriented ellipsoidal inclusions. *Acta Mechanica,* 140: 31-40, (2000).

[143] Ju J, Chen T. Effective elastic moduli of two-phase composites containing randomly dispersed spherical inhomogeneities. *Acta Mechanica,* 103: 123-144, (1994).

[144] Li L, Wang T. A unified approach to predict overall properties of composite materials. *Materials Characterization,* 54: 49-62, (2005).

[145] Mori T, Tanaka K. Average stress in matrix and average elastic energy of materials with misfitting inclusions. *Acta Metallurgica,* 21: 571-574, (1973).

[146] Peng X, Hu N, Zheng H, Fukunaga H. Evaluation of mechanical properties of particulate composites with a combined self-consistent and Mori–Tanaka approach. *Mechanics of Materials,* 41: 1288-1297, (2009).

[147] Westbrook KK, Parakh V, Chung T, Mather PT, Wan LC, Dunn ML, Qi HJ. Constitutive modeling of shape memory effects in semicrystalline polymers with stretch induced crystallization. *Journal of Engineering Materials and Technology*, 132: 041010, (2010).

[148] Long KN, Scott TF, Qi HJ, Bowman CN, Dunn ML. Photomechanics of light-activated polymers. *Journal of the Mechanics and Physics of Solids,* 57: 1103-1121, (2009).

[149] Debenedetti PG. Metastable liquids: concepts and principles, Princeton University Press, (1996).

[150] Glotzer SC. Spatially heterogeneous dynamics in liquids: insights from simulation. *Journal of Non-Crystalline Solids*, 274: 342-355, (2000).

[151] Kauzmann W. The Nature of the Glassy State and the Behavior of Liquids at Low Temperatures. *Chemical Reviews,* 43: 219-256, (1948).

[152] Fulcher GS. Analysis of recent measurements of the viscosity of glasses. *Journal of the American Ceramic Society,* 8: 339-355, (1925).

[153] Tammann G, Hesse W. The dependence of viscosity upon the temperature of supercooled liquids. *Z. Anorg. Allg. Chem,* 156: 245-257, (1926).

[154] Vogel H. The law of viscosity change with temperature. *Physikalische Zeitschrift,* 22: 645-646, (1921).

[155] Adam G, Gibbs JH. On the temperature dependence of cooperative relaxation properties in glass‐forming liquids. *The Journal of Chemical Physics,* 43: 139-146, (1965).

[156] Gibbs JH, DiMarzio EA. Nature of the glass transition and the glassy state. *The Journal of Chemical Physics,* 28: 373-383, (1958).

[157] Wales D. Energy Landscapes. , Cambridge University Press, Cambridge, (2003).

[158] Sasai M. Energy landscape picture of supercooled liquids: Application of a generalized random energy model. *The Journal of Chemical Physics,* 118: 10651-10662, (2003).

[159] Andersen HC. Molecular dynamics studies of heterogeneous dynamics and dynamic crossover in supercooled atomic liquids. *Proceedings of the National Academy of Sciences of the United States of America,* 102: 6686-6691, (2005).

[160] Ediger MD. Spatially heterogeneous dynamics in supercooled liquids. *Annual Review of Physical Chemistry,* 51: 99-128, (2000).

[161] Richert R. Heterogeneous dynamics in liquids: fluctuations in space and time. *Journal of Physics: Condensed Matter,* 14: R703, (2002).

[162] Liu S, Jiao W, Sun B, Wang W. A quasi-phase perspective on flow units of glass transition and plastic flow in metallic glasses. *Journal of Non-Crystalline Solids,* 376: 76-80, (2013).

[163] Gupta PK, Mauro JC. The laboratory glass transition. *The Journal of Chemical Physics,* 126: 224504, (2007).

[164] Bauer T, Lunkenheimer P, Loidl A. Cooperativity and the freezing of molecular motion at the glass transition. *Physical Review Letters,* 111: 225702, (2013).

[165] Gainaru C, Kastner S, Mayr F, Lunkenheimer P, Schildmann S, Weber H, Hiller W, Loidl A, Böhmer R. Hydrogen-bond equilibria and lifetimes in a monohydroxy alcohol. *Physical Review Letters,* 107: 118304, (2011).

[166] Kudlik A, Benkhof S, Blochowicz T, Tschirwitz C, Rössler E. The dielectric response of simple organic glass formers. *Journal of Molecular Structure,* 479: 201-218, (1999).

[167] Lunkenheimer P, Kastner S, Köhler M, Loidl A. Temperature development of glassy α-relaxation dynamics determined by broadband dielectric spectroscopy. *Physical Review E,* 81: 051504, (2010).

[168] Eyring H. Viscosity, plasticity, and diffusion as examples of absolute reaction rates. *The Journal of Chemical Physics,* 4: 283-291, (1936).

[169] Patashinski A. Stress-induced glass transitions. *International Journal of Engineering Science,* 83: 95-98, (2014).

[170] Tobolsky A, Eyring H. Mechanical properties of polymeric materials. *The Journal of Chemical Physics,* 11: 125-134, (1943).

[171] Zhou Z, Chudnovsky A, Bosnyak C, Sehanobish K. Cold‐drawing (necking) behavior of polycarbonate as a double glass transition. *Polymer Engineering & Science,* 35: 304-309, (1995).

[172] Derrida B. Random-energy model: Limit of a family of disordered models. *Physical Review Letters,* 45: 79, (1980).

[173] Porter D. Group interaction modelling of polymer properties, CRC Press, (1995).

[174] Sharafi S, Li G. A multiscale approach for modeling actuation response of polymeric artificial muscles. *Soft Matter,* (2015).

[175] Zwanzig R. Nonequilibrium statistical mechanics, Oxford University Press, (2001).

[176] Weng G. Some elastic properties of reinforced solids, with special reference to isotropic ones containing spherical inclusions. *International Journal of Engineering Science,* 22: 845-856, (1984).

[177] Levin V. Thermal expansion coefficients of heterogeneous materials. *Mekhanika Tverdogo Tela,* 2: 88-94, (1967).

[178] Rosen BW, Hashin Z. Effective thermal expansion coefficients and specific heats of composite materials. *International Journal of Engineering Science,* 8: 157-173, (1970).

[179] Ivens J, Urbanus M, De Smet C. Shape recovery in a thermoset shape memory polymer and its fabric-reinforced composites. *Status: published,* (2011).

[180] Yang Q, Li G. Spider-silk-like shape memory polymer fiber for vibration damping *Smart Materials and Structures,* 23: 105032, (2014).

[181] Arrieta JS, Diani J, Gilormini P. Cyclic and monotonic testing of free and constrained recovery properties of a chemically crosslinked acrylate. *Journal of Applied Polymer Science,* 131: (2014).

[182] Vyazovkin S, Sbirrazzuoli N, Dranca I. Variation in activation energy of the glass transition for polymers of different dynamic fragility. *Macromolecular Chemistry and Physics,* 207: 1126-1130, (2006).

[183] Castro F, Westbrook KK, Long KN, Shandas R, Qi HJ. Effects of thermal rates on the thermomechanical behaviors of amorphous shape memory polymers. *Mechanics of Time-Dependent Materials,* 14: 219-241, (2010).

[184] Li G, Uppu N. Shape memory polymer based self-healing syntactic foam: 3-D confined thermomechanical characterization. *Composites Science and Technology,* 70: 1419-1427, (2010).

[185] Mess éL, P ézolet M, Prud'homme R. Molecular relaxation study of polystyrene: influence of temperature, draw rate and molecular weight. *Polymer,* 42: 563-575, (2001).

[186] Nguyen T, Yakacki CM, Brahmbhatt PD, Chambers ML. Modeling the relaxation mechanisms of amorphous shape memory polymers. *Advanced Materials,* 22: 3411-3423, (2010).

[187] Strobl GR. The Physics of Polymers: Concepts for Understanding Their Structures and Behavior, Springer Science & Business Media, (2007).

[188] Wang A, Li G. Stress memory of a thermoset shape memory polymer. *Journal of Applied Polymer Science,* 132: (2015).

[189] Nettles D. Thermechanical Charaterization of A Shape Memory Polymer Based Syntactioc Foam. M.S. Thesis, Louisiana State University (2009).

[190] Comyn J, in *Handbook of Adhesives and Sealants*, P Cognard, Editor. 2006, Elsevier: Amsterdam, The Netherlands. p. 34.

[191] Wu S, *Surface and Interfacial Tensions of Polymers, Oligomers, Plasticizers, and Organic Pigments,* in *Polymer Handbook* J. Brandrup and EH Immergut, Editors. 1989, Wiley-Interscience,: New York, NY. p. 414-426.

[192] Paluch M. Dielectric and mechanical relaxation in epoxy systems with molecules of differing topology. *Journal of Physics: Condensed Matter,* 12: 9511, (2000).

[193] Schönhals A. Dielectric spectroscopy onthe dynamics of amorphous polymeric systems. *Application note Dielectrics,* 1: (1998).

[194] Reinsberg S, Qiu X, Wilhelm M, Spiess HW, Ediger M. Length scale of dynamic heterogeneity in supercooled glycerol near Tg. *The Journal of Chemical Physics,* 114: 7299-7302, (2001).

[195] Shell MS, Debenedetti PG, Stillinger FH. Dynamic heterogeneity and non-Gaussian behaviour in a model supercooled liquid. *Journal of Physics: Condensed Matter,* 17: S4035, (2005).

[196] Li G, Lee-Sullivan P, Thring R. Determination of activation energy for glass transition of an epoxy adhesive using dynamic mechanical analysis. *Journal of Thermal Analysis and Calorimetry*, 60: 377-390, (2000).

[197] Chaboche J, Kanouté P, Roos A. On the capabilities of mean-field approaches for the description of plasticity in metal matrix composites. *International Journal of Plasticity*, 21: 1409-1434, (2005).

[198] Thirtha V, Lehman R, Nosker T. Morphological effects on glass transition behavior in selected immiscible blends of amorphous and semicrystalline polymers. *Polymer,* 47: 5392-5401, (2006).

[199] Hall R, Rao I, Qi H. Thermodynamics and thermal decomposition for shape memory effects with crystallization based on dissipation and logarithmic strain. *Mechanics of Time-Dependent Materials,* 18: 437-452, (2014).

[200] Rajagopal K, Srinivasa A. On the inelastic behavior of solids—Part 1: Twinning. *International Journal of Plasticity,* 11: 653-678, (1995).

[201] Rajagopal K, Srinivasa A. Mechanics of the inelastic behavior of materials—Part 1, theoretical underpinnings. *International Journal of Plasticity,* 14: 945-967, (1998).

[202] Rajagopal K, Srinivasa A. On the thermomechanics of shape memory wires. *Zeitschrift für angewandte Mathematik und Physik ZAMP,* 50: 459-496, (1999).

[203] Barot G, Rao I. Constitutive modeling of the mechanics associated with crystallizable shape memory polymers. *Zeitschrift für angewandte Mathematik und Physik ZAMP,* 57: 652-681, (2006).

[204] Barot G, Rao I, Rajagopal K. A thermodynamic framework for the modeling of crystallizable shape memory polymers. *International Journal of Engineering Science,* 46: 325-351, (2008).

[205] Moon S, Rao I, Chester S. Triple Shape Memory Polymers: Constitutive Modeling and Numerical Simulation. *Journal of Applied Mechanics,* 83: 071008, (2016).

[206] Flory PJ. Thermodynamics of crystallization in high polymers. I. Crystallization induced by stretching. *The Journal of Chemical Physics,* 15: 397-408, (1947).

[207] Ogden R. Large deformation isotropic elasticity-on the correlation of theory and experiment for incompressible rubberlike solids. in *Proceedings of the Royal Society of London A: Mathematical, Physical and Engineering Sciences*. 1972. The Royal Society.

[208] Treloar LRG. The physics of rubber elasticity, Oxford University Press, USA, (1975).

[209] Mark JE. Interpretation of polymer properties in terms of chain conformations and spatial configurations. *Accounts of Chemical Research,* 12: 49-55, (1979).

[210] Rao I, Rajagopal K. Phenomenological modelling of polymer crystallization using the notion of multiple natural configurations. *Interfaces and free boundaries,* 2: 73-94, (2000).

[211] Guo J, Narh KA. Simplified model of stress‐induced crystallization kinetics of polymers. *Advances in Polymer Technology,* 21: 214-222, (2002).

[212] Lee B, Parks D, Ahzi S. Micromechanical modeling of large plastic deformation and texture evolution in semi-crystalline polymers. *Journal of the Mechanics and Physics of Solids,* 41: 1651-1687, (1993).

[213] Love A. A Treatise on the Mathematical theory of Elasticity, Dover Publication, New York, (1944).

[214] Van der Heijden G, Thompson J. Helical and localised buckling in twisted rods: a unified analysis of the symmetric case. *Nonlinear Dyn.*, 21: 71-99, (2000).

[215] Sharafi S, Li G. A multiscale approach for modeling actuation response of polymeric artificial muscles. *Soft Matter*, 11: 3833-3843, (2015).

[216] Halpin JC, *Effects of Environmental Factors on Composite Materials*, 1969, DTIC Document.

[217] Shigley JE, Mischke CR, Budynas RG. Mechanical engineering design, 7th ed., McGraw-Hill, New York, (2004).

[218] Ma H, Li Y, Wang D. Investigations of fiber twist on the mechanical properties of sisal fiber yarns and their composites. *J. Reinf. Plast. Compos.*, (2014). DOI: 10.1177/0731684413520187.

[219] MILITKÝ J, KOVAČIČ V. TWIST LEVEL INFLUENCE ON THE DYNAMIC MECHANICAL CHARACTERISTICS OF POLYAMIDE FILAMENT. *PROCEEDINGS OF HIGHER EDUCATION INSTITUTIONS*, 55, (2011).

[220] Sze GM, Spruiell JE, White JL. The influence of drawing, twisting, heat setting, and untwisting on the structure and mechanical properties of melt‐spun high‐density polyethylene fiber. *Journal of Applied Polymer Science*, 20: 1823-1847, (1976).

[221] Pipes RB, Hubert P. Helical carbon nanotube arrays: mechanical properties. *Composites Science and Technology*, 62: 419-428, (2002).

[222] Pipes RB, Hubert P. Helical carbon nanotube arrays: thermal expansion. *Composites Science and Technology*, 63: 1571-1579, (2003).

[223] Suhai S. Ab initio calculation of polyethylene deformation including electron correlation effects. *Journal of Polymer Science Part B: Polymer Physics*, 21: 1341-1346, (1983).

[224] Zhao Z-L, Zhao H-P, Wang J-S, Zhang Z, Feng X-Q. Mechanical properties of carbon nanotube ropes with hierarchical helical structures. *J. Mech. Phys. Solids*, 71: 64-83, (2014).

[225] Barham P, Arridge R. A fiber composite model of highly oriented polyethylene. *Journal of Polymer Science Part B: Polymer Physics*, 15: 1177-1188, (1977).

[226] Choy C, Leung W. Elastic moduli of ultradrawn polyethylene. *J. Polym. Sci., Polym. Phy. Ed.*, 23: 1759-1780, (1985).

[227] Grubb DT, Prasad K. High-modulus polyethylene fiber structure as shown by x-ray diffraction. *Macromolecules*, 25: 4575-4582, (1992).

[228] Kip BJ, Van Eijk MC, Meier RJ. Molecular deformation of high‐modulus polyethylene fibers studied by micro‐raman spectroscopy. *Journal of Polymer Science Part B: Polymer Physics,* 29: 99-108, (1991).

[229] Baughman RH. Negative thermal expansion in crystalline linear polymers. *Journal of Chemical Physics,* 58: 2976-2983, (1973).

[230] Choy C, Chen F, Young K. Negative thermal expansion in oriented crystalline polymers. *Journal of Polymer Science Part B: Polymer Physics,* 19: 335-352, (1981).

[231] Maranganti R, Sharma P. Length scales at which classical elasticity breaks down for various materials. *Physical Review Letters,* 98: 195504, (2007).

[232] Dym CL. Consistent derivations of spring rates for helical springs. *Journal of Mechanical Design,* 131: 071004, (2009).

[233] Clive D, Shames I. Solid Mechanics: A Variational Approach, McGraw-Hill, New York, (1973).

[234] Dym CL. Structural modeling and analysis, Cambridge University Press, New York, (1997).

[235] He T. An estimate of the strength of polymers. *Polym.,* 27: 253-255, (1986).

[236] Klei HE, Stewart JJ. Calculation of polymer elastic moduli using semiempirical methods. *International Journal of Quantum Chemistry,* 30: 529-540, (1986).

[237] Odajima A, Maeda T. Calculation of the elastic constants and the lattice energy of the polyethylene crystal. in *J. Polym. Sci., Part C: Polym. Sym.* 1967. Wiley Online Library.

[238] Pechhold W, Blasenbrey S. Molekülbewegung in Polymeren. *Colloid Polym. Sci.,* 241: 955-976, (1970).

[239] Tashiro K, Kobayashi M, Tadokoro H. Calculation of three-dimensional elastic constants of polymer crystals. 2. Application to orthorhombic polyethylene and poly (vinyl alcohol). *Macromolecules,* 11: 914-918, (1978).

[240] Chan O, Chen F, Choy C, Ward I. The elastic constants of extruded polypropylene and polyethylene terephthalate. *Journal of Physics D: Applied Physics,* 11: 617, (1978).

[241] Holliday L, White J. The stiffness of polymers in relation to their structure. *Pure and Applied Chemistry,* 26: 545-582, (1971).

[242] Rider J, Watkinson K. Ultrasonic measurements of the elastic stiffness constants of oriented polyethylene. *Polym.,* 19: 645-653, (1978).

[243] Davis G, Eby R, Colson J. Thermal expansion of polyethylene unit cell: effect of lamella thickness. *Journal of Applied Physics,* 41: 4316-4326, (1970).

[244] Kobayashi Y, Keller A. The temperature coefficient of the c lattice parameter of polyethylene; an example of thermal shrinkage along the chain direction. *Polym.,* 11: 114-117, (1970).

[245] Choy C, Chen F, Ong E. Anistropic thermal expansion of oriented crystalline polymers. *Polym.,* 20: 1191-1198, (1979).

[246] Yang Q, Li G. Temperature and rate dependent thermomechanical modeling of shape memory polymers with physics based phase evolution law. *International Journal of Plasticity,* 80: 168-186, (2016).

[247] Cox H. The elasticity and strength of paper and other fibrous materials. *Br. J. Appl. Phys.,* 3: 72, (1952).

[248] Halpin JC, Kardos J. The Halpin-Tsai equations: a review. *Polymer Engineering and Science,* 16: 344-352, (1976).

[249] Boyd RH. The modulus of the amorphous component in polyethylenes. *Polymer Engineering and Science,* 19: 1010-1016, (1979).

[250] Xiong B, Lame O, Chenal J-M, Rochas C, Seguela R, Vigier G. Amorphous Phase Modulus and Micro–Macro Scale Relationship in Polyethylene via in Situ SAXS and WAXS. *Macromolecules,* 48: 2149-2160, (2015).

[251] Chen S, Hu J, Zhuo H, Zhu Y. Two-way shape memory effect in polymer laminates. *Materials Letters,* 62: 4088-4090, (2008).

[252] Hong SJ, Yu W-R, Youk JH. Two-way shape memory behavior of shape memory polyurethanes with a bias load. *Smart Materials and Structures,* 19: 035022, (2010).

[253] Darwin C. On the movements and habits of climbing plants, John Murray, London, (1865).

[254] Gore J, Bryant Z, Nöllmann M, Le MU, Cozzarelli NR, Bustamante C. DNA overwinds when stretched. *Nature,* 442: 836-839, (2006).

[255] Grande C, Patel NH. Nodal signalling is involved in left–right asymmetry in snails. *Nature,* 457: 1007-1011, (2009).

[256] Saranathan V, Osuji CO, Mochrie SG, Noh H, Narayanan S, Sandy A, Dufresne ER, Prum RO. Structure, function, and self-assembly of single network gyroid (I4132) photonic crystals in butterfly wing scales. *Proceedings of the National Academy of Sciences,* 107: 11676-11681, (2010).

[257] Kong XY, Wang ZL. Spontaneous polarization-induced nanohelixes, nanosprings, and nanorings of piezoelectric nanobelts. *Nano Letters,* 3: 1625-1631, (2003).

[258] Wu A, Nie X, Hudspeth M, Chen W, Chou T-W, Lashmore D, Schauer M, Towle E, Rioux J. Carbon nanotube fibers as torsion sensors. *Applied Physics Letters,* 100: 201908, (2012).

[259] Yang Q, Li G. A top-down multi-scale modeling for actuation response of polymeric artificial muscles. *Journal of the Mechanics and Physics of Solids,* 92: 237-259, (2016).

[260] Wang J-S, Wang G, Feng X-Q, Kitamura T, Kang Y-L, Yu S-W, Qin Q-H. Hierarchical chirality transfer in the growth of Towel Gourd tendrils. *Scientific reports,* 3: (2013).

[261] Deteresa S, Allen S, Farris R, Porter R. Compressive and torsional behaviour of Kevlar 49 fibre. *Journal of Materials Science,* 19: 57-72, (1984).

[262] Huang M, Dong X, Wang L, Zhao J, Liu G, Wang D. Two-way shape memory property and its structural origin of cross-linked poly (ε-caprolactone). *RSC Advances,* 4: 55483-55494, (2014).

[263] Madden JD, Vandesteeg NA, Anquetil PA, Madden PG, Takshi A, Pytel RZ, Lafontaine SR, Wieringa PA, Hunter IW. Artificial muscle technology: physical principles and naval prospects. *IEEE Journal of oceanic engineering,* 29: 706-728, (2004).

APPENDIX A: COPYRIGHT PERMISSION FOR CHAPTER 2

ELSEVIER LICENSE
TERMS AND CONDITIONS

Feb 22, 2017

This Agreement between Qianxi Yang ("You") and Elsevier ("Elsevier") consists of your license details and the terms and conditions provided by Elsevier and Copyright Clearance Center.

License Number	4054260853644
License date	
Licensed Content Publisher	Elsevier
Licensed Content Publication	International Journal of Plasticity
Licensed Content Title	Temperature and rate dependent thermomechanical modeling of shape memory polymers with physics based phase evolution law
Licensed Content Author	Qianxi Yang,Guoqiang Li
Licensed Content Date	May 2016
Licensed Content Volume	80
Licensed Content Issue	n/a
Licensed Content Pages	19
Start Page	168
End Page	186
Type of Use	reuse in a thesis/dissertation
Portion	full article
Format	both print and electronic
Are you the author of this Elsevier article?	Yes
Will you be translating?	No
Order reference number	
Title of your thesis/dissertation	Thermomechanical Modeling of Polymeric Actuators
Expected completion date	Apr 2017
Estimated size (number of pages)	130
Elsevier VAT number	GB 494 6272 12
Requestor Location	Qianxi Yang 3261 Patrick F. Taylor Hall BATON ROUGE, LA 70803 United States Attn: Qianxi Yang
Publisher Tax ID	98-0397604
Total	0.00 USD
Terms and Conditions	

INTRODUCTION

1. The publisher for this copyrighted material is Elsevier. By clicking "accept" in connection with completing this licensing transaction, you agree that the following terms and conditions apply to this transaction (along with the Billing and Payment terms and conditions established by Copyright Clearance Center, Inc. ("CCC"), at the time that you opened your Rightslink account and that are available at any time at http://myaccount.copyright.com).

GENERAL TERMS

2. Elsevier hereby grants you permission to reproduce the aforementioned material subject to the terms and conditions indicated.

3. Acknowledgement: If any part of the material to be used (for example, figures) has appeared in our publication with credit or acknowledgement to another source, permission must also be sought from that source. If such permission is not obtained then that material may not be included in your publication/copies. Suitable acknowledgement to the source must be made, either as a footnote or in a reference list at the end of your publication, as follows:

"Reprinted from Publication title, Vol /edition number, Author(s), Title of article / title of chapter, Pages No., Copyright (Year), with permission from Elsevier [OR APPLICABLE SOCIETY COPYRIGHT OWNER]." Also Lancet special credit - "Reprinted from The Lancet, Vol. number, Author(s), Title of article, Pages No., Copyright (Year), with permission from Elsevier."

4. Reproduction of this material is confined to the purpose and/or media for which permission is hereby given.

5. Altering/Modifying Material: Not Permitted. However figures and illustrations may be altered/adapted minimally to serve your work. Any other abbreviations, additions, deletions and/or any other alterations shall be made only with prior written authorization of Elsevier Ltd. (Please contact Elsevier at permissions@elsevier.com). No modifications can be made to any Lancet figures/tables and they must be reproduced in full.

6. If the permission fee for the requested use of our material is waived in this instance, please be advised that your future requests for Elsevier materials may attract a fee.

7. Reservation of Rights: Publisher reserves all rights not specifically granted in the combination of (i) the license details provided by you and accepted in the course of this licensing transaction, (ii) these terms and conditions and (iii) CCC's Billing and Payment terms and conditions.

8. License Contingent Upon Payment: While you may exercise the rights licensed immediately upon issuance of the license at the end of the licensing process for the transaction, provided that you have disclosed complete and accurate details of your proposed use, no license is finally effective unless and until full payment is received from you (either by publisher or by CCC) as provided in CCC's Billing and Payment terms and conditions. If full payment is not received on a timely basis, then any license preliminarily granted shall be deemed automatically revoked and shall be void as if never granted. Further, in the event that you breach any of these terms and conditions or any of CCC's Billing and Payment terms and conditions, the license is automatically revoked and shall be void as if never granted. Use of materials as described in a revoked license, as well as any use of the materials beyond the scope of an unrevoked license, may constitute copyright infringement and publisher

reserves the right to take any and all action to protect its copyright in the materials.
9. Warranties: Publisher makes no representations or warranties with respect to the licensed material.
10. Indemnity: You hereby indemnify and agree to hold harmless publisher and CCC, and their respective officers, directors, employees and agents, from and against any and all claims arising out of your use of the licensed material other than as specifically authorized pursuant to this license.
11. No Transfer of License: This license is personal to you and may not be sublicensed, assigned, or transferred by you to any other person without publisher's written permission.
12. No Amendment Except in Writing: This license may not be amended except in a writing signed by both parties (or, in the case of publisher, by CCC on publisher's behalf).
13. Objection to Contrary Terms: Publisher hereby objects to any terms contained in any purchase order, acknowledgment, check endorsement or other writing prepared by you, which terms are inconsistent with these terms and conditions or CCC's Billing and Payment terms and conditions. These terms and conditions, together with CCC's Billing and Payment terms and conditions (which are incorporated herein), comprise the entire agreement between you and publisher (and CCC) concerning this licensing transaction. In the event of any conflict between your obligations established by these terms and conditions and those established by CCC's Billing and Payment terms and conditions, these terms and conditions shall control.
14. Revocation: Elsevier or Copyright Clearance Center may deny the permissions described in this License at their sole discretion, for any reason or no reason, with a full refund payable to you. Notice of such denial will be made using the contact information provided by you. Failure to receive such notice will not alter or invalidate the denial. In no event will Elsevier or Copyright Clearance Center be responsible or liable for any costs, expenses or damage incurred by you as a result of a denial of your permission request, other than a refund of the amount(s) paid by you to Elsevier and/or Copyright Clearance Center for denied permissions.

LIMITED LICENSE

The following terms and conditions apply only to specific license types:
15. **Translation**: This permission is granted for non-exclusive world **English** rights only unless your license was granted for translation rights. If you licensed translation rights you may only translate this content into the languages you requested. A professional translator must perform all translations and reproduce the content word for word preserving the integrity of the article.
16. **Posting licensed content on any Website**: The following terms and conditions apply as follows: Licensing material from an Elsevier journal: All content posted to the web site must maintain the copyright information line on the bottom of each image; A hyper-text must be included to the Homepage of the journal from which you are licensing at http://www.sciencedirect.com/science/journal/xxxxx or the Elsevier homepage for books at http://www.elsevier.com; Central Storage: This license does not include permission for a scanned version of the material to be stored in a central repository such as that provided by Heron/XanEdu.

Licensing material from an Elsevier book: A hyper-text link must be included to the Elsevier homepage at http://www.elsevier.com . All content posted to the web site must maintain the copyright information line on the bottom of each image.

Posting licensed content on Electronic reserve: In addition to the above the following clauses are applicable: The web site must be password-protected and made available only to bona fide students registered on a relevant course. This permission is granted for 1 year only. You may obtain a new license for future website posting.

17. **For journal authors:** the following clauses are applicable in addition to the above:

Preprints:

A preprint is an author's own write-up of research results and analysis, it has not been peer-reviewed, nor has it had any other value added to it by a publisher (such as formatting, copyright, technical enhancement etc.).

Authors can share their preprints anywhere at any time. Preprints should not be added to or enhanced in any way in order to appear more like, or to substitute for, the final versions of articles however authors can update their preprints on arXiv or RePEc with their Accepted Author Manuscript (see below).

If accepted for publication, we encourage authors to link from the preprint to their formal publication via its DOI. Millions of researchers have access to the formal publications on ScienceDirect, and so links will help users to find, access, cite and use the best available version.

Please note that Cell Press, The Lancet and some society-owned have different preprint policies. Information on these policies is available on the journal homepage.

Accepted Author Manuscripts: An accepted author manuscript is the manuscript of an article that has been accepted for publication and which typically includes author-incorporated changes suggested during submission, peer review and editor-author communications.

Authors can share their accepted author manuscript:

- immediately
  - via their non-commercial person homepage or blog
  - by updating a preprint in arXiv or RePEc with the accepted manuscript
  - via their research institute or institutional repository for internal institutional uses or as part of an invitation-only research collaboration work-group
  - directly by providing copies to their students or to research collaborators for their personal use
  - for private scholarly sharing as part of an invitation-only work group on commercial sites with which Elsevier has an agreement
- after the embargo period
  - via non-commercial hosting platforms such as their institutional repository
  - via commercial sites with which Elsevier has an agreement

In all cases accepted manuscripts should:

- link to the formal publication via its DOI
- bear a CC-BY-NC-ND license - this is easy to do
- if aggregated with other manuscripts, for example in a repository or other site, be shared in alignment with our hosting policy not be added to or enhanced in any way to appear more like, or to substitute for, the published journal article.

Published journal article (JPA): A published journal article (PJA) is the definitive final record of published research that appears or will appear in the journal and embodies all value-adding publishing activities including peer review co-ordination, copy-editing, formatting, (if relevant) pagination and online enrichment.
Policies for sharing publishing journal articles differ for subscription and gold open access articles:
Subscription Articles: If you are an author, please share a link to your article rather than the full-text. Millions of researchers have access to the formal publications on ScienceDirect, and so links will help your users to find, access, cite, and use the best available version.
Theses and dissertations which contain embedded PJAs as part of the formal submission can be posted publicly by the awarding institution with DOI links back to the formal publications on ScienceDirect.
If you are affiliated with a library that subscribes to ScienceDirect you have additional private sharing rights for others' research accessed under that agreement. This includes use for classroom teaching and internal training at the institution (including use in course packs and courseware programs), and inclusion of the article for grant funding purposes.
Gold Open Access Articles: May be shared according to the author-selected end-user license and should contain a CrossMark logo, the end user license, and a DOI link to the formal publication on ScienceDirect.
Please refer to Elsevier's posting policy for further information.
18. **For book authors** the following clauses are applicable in addition to the above: Authors are permitted to place a brief summary of their work online only. You are not allowed to download and post the published electronic version of your chapter, nor may you scan the printed edition to create an electronic version. **Posting to a repository:** Authors are permitted to post a summary of their chapter only in their institution's repository.
19. **Thesis/Dissertation:** If your license is for use in a thesis/dissertation your thesis may be submitted to your institution in either print or electronic form. Should your thesis be published commercially, please reapply for permission. These requirements include permission for the Library and Archives of Canada to supply single copies, on demand, of the complete thesis and include permission for Proquest/UMI to supply single copies, on demand, of the complete thesis. Should your thesis be published commercially, please reapply for permission. Theses and dissertations which contain embedded PJAs as part of the formal submission can be posted publicly by the awarding institution with DOI links back to the formal publications on ScienceDirect.

Elsevier Open Access Terms and Conditions
You can publish open access with Elsevier in hundreds of open access journals or in nearly 2000 established subscription journals that support open access publishing. Permitted third party re-use of these open access

articles is defined by the author's choice of Creative Commons user license. See our open access license policy for more information.

Terms & Conditions applicable to all Open Access articles published with Elsevier:

Any reuse of the article must not represent the author as endorsing the adaptation of the article nor should the article be modified in such a way as to damage the author's honour or reputation. If any changes have been made, such changes must be clearly indicated.

The author(s) must be appropriately credited and we ask that you include the end user license and a DOI link to the formal publication on ScienceDirect.

If any part of the material to be used (for example, figures) has appeared in our publication with credit or acknowledgement to another source it is the responsibility of the user to ensure their reuse complies with the terms and conditions determined by the rights holder.

Additional Terms & Conditions applicable to each Creative Commons user license:

CC BY: The CC-BY license allows users to copy, to create extracts, abstracts and new works from the Article, to alter and revise the Article and to make commercial use of the Article (including reuse and/or resale of the Article by commercial entities), provided the user gives appropriate credit (with a link to the formal publication through the relevant DOI), provides a link to the license, indicates if changes were made and the licensor is not represented as endorsing the use made of the work. The full details of the license are available at http://creativecommons.org/licenses/by/4.0.

CC BY NC SA: The CC BY-NC-SA license allows users to copy, to create extracts, abstracts and new works from the Article, to alter and revise the Article, provided this is not done for commercial purposes, and that the user gives appropriate credit (with a link to the formal publication through the relevant DOI), provides a link to the license, indicates if changes were made and the licensor is not represented as endorsing the use made of the work. Further, any new works must be made available on the same conditions. The full details of the license are available at http://creativecommons.org/licenses/by-nc-sa/4.0.

CC BY NC ND: The CC BY-NC-ND license allows users to copy and distribute the Article, provided this is not done for commercial purposes and further does not permit distribution of the Article if it is changed or edited in any way, and provided the user gives appropriate credit (with a link to the formal publication through the relevant DOI), provides a link to the license, and that the licensor is not represented as endorsing the use made of the work. The full details of the license are available at http://creativecommons.org/licenses/by-nc-nd/4.0. Any commercial reuse of Open Access articles published with a CC BY NC SA or CC BY NC ND license requires permission from Elsevier and will be subject to a fee.

Commercial reuse includes:

- Associating advertising with the full text of the Article
- Charging fees for document delivery or access
- Article aggregation
- Systematic distribution via e-mail lists or share buttons

Posting or linking by commercial companies for use by customers of those companies.

20. Other Conditions:

v1.9

APPENDIX B: COPYRIGHT PERMISSION FOR CHAPTER 4

ELSEVIER LICENSE
TERMS AND CONDITIONS

Feb 22, 2017

This Agreement between Qianxi Yang ("You") and Elsevier ("Elsevier") consists of your license details and the terms and conditions provided by Elsevier and Copyright Clearance Center.

License Number	4054261128973
License date	
Licensed Content Publisher	Elsevier
Licensed Content Publication	Journal of the Mechanics and Physics of Solids
Licensed Content Title	A top-down multi-scale modeling for actuation response of polymeric artificial muscles
Licensed Content Author	Qianxi Yang,Guoqiang Li
Licensed Content Date	July 2016
Licensed Content Volume	92
Licensed Content Issue	n/a
Licensed Content Pages	23
Start Page	237
End Page	259
Type of Use	reuse in a thesis/dissertation
Intended publisher of new work	other
Portion	full article
Format	both print and electronic
Are you the author of this Elsevier article?	Yes
Will you be translating?	No
Order reference number	
Title of your thesis/dissertation	Thermomechanical Modeling of Polymeric Actuators
Expected completion date	Apr 2017
Estimated size (number of pages)	130
Elsevier VAT number	GB 494 6272 12
Requestor Location	Qianxi Yang 3261 Patrick F. Taylor Hall BATON ROUGE, LA 70803 United States Attn: Qianxi Yang
Publisher Tax ID	98-0397604
Total	0.00 USD

Terms and Conditions

INTRODUCTION

1. The publisher for this copyrighted material is Elsevier. By clicking "accept" in connection with completing this licensing transaction, you agree that the following terms and conditions apply to this transaction (along with the Billing and Payment terms and conditions established by Copyright Clearance Center, Inc. ("CCC"), at the time that you opened your Rightslink account and that are available at any time at http://myaccount.copyright.com).

GENERAL TERMS

2. Elsevier hereby grants you permission to reproduce the aforementioned material subject to the terms and conditions indicated.
3. Acknowledgement: If any part of the material to be used (for example, figures) has appeared in our publication with credit or acknowledgement to another source, permission must also be sought from that source. If such permission is not obtained then that material may not be included in your publication/copies. Suitable acknowledgement to the source must be made, either as a footnote or in a reference list at the end of your publication, as follows:
"Reprinted from Publication title, Vol /edition number, Author(s), Title of article / title of chapter, Pages No., Copyright (Year), with permission from Elsevier [OR APPLICABLE SOCIETY COPYRIGHT OWNER]." Also Lancet special credit - "Reprinted from The Lancet, Vol. number, Author(s), Title of article, Pages No., Copyright (Year), with permission from Elsevier."
4. Reproduction of this material is confined to the purpose and/or media for which permission is hereby given.
5. Altering/Modifying Material: Not Permitted. However figures and illustrations may be altered/adapted minimally to serve your work. Any other abbreviations, additions, deletions and/or any other alterations shall be made only with prior written authorization of Elsevier Ltd. (Please contact Elsevier at permissions@elsevier.com). No modifications can be made to any Lancet figures/tables and they must be reproduced in full.
6. If the permission fee for the requested use of our material is waived in this instance, please be advised that your future requests for Elsevier materials may attract a fee.
7. Reservation of Rights: Publisher reserves all rights not specifically granted in the combination of (i) the license details provided by you and accepted in the course of this licensing transaction, (ii) these terms and conditions and (iii) CCC's Billing and Payment terms and conditions.
8. License Contingent Upon Payment: While you may exercise the rights licensed immediately upon issuance of the license at the end of the licensing process for the transaction, provided that you have disclosed complete and accurate details of your proposed use, no license is finally effective unless and until full payment is received from you (either by publisher or by CCC) as provided in CCC's Billing and Payment terms and conditions. If full payment is not received on a timely basis, then any license preliminarily granted shall be deemed automatically revoked and shall be void as if never granted. Further, in the event that you breach any of these terms and conditions or any of CCC's Billing and Payment terms and conditions, the license is automatically revoked and shall be void as if never granted. Use of materials as described in a revoked license, as well as any use of the materials beyond the scope of an

unrevoked license, may constitute copyright infringement and publisher reserves the right to take any and all action to protect its copyright in the materials.

9. Warranties: Publisher makes no representations or warranties with respect to the licensed material.

10. Indemnity: You hereby indemnify and agree to hold harmless publisher and CCC, and their respective officers, directors, employees and agents, from and against any and all claims arising out of your use of the licensed material other than as specifically authorized pursuant to this license.

11. No Transfer of License: This license is personal to you and may not be sublicensed, assigned, or transferred by you to any other person without publisher's written permission.

12. No Amendment Except in Writing: This license may not be amended except in a writing signed by both parties (or, in the case of publisher, by CCC on publisher's behalf).

13. Objection to Contrary Terms: Publisher hereby objects to any terms contained in any purchase order, acknowledgment, check endorsement or other writing prepared by you, which terms are inconsistent with these terms and conditions or CCC's Billing and Payment terms and conditions. These terms and conditions, together with CCC's Billing and Payment terms and conditions (which are incorporated herein), comprise the entire agreement between you and publisher (and CCC) concerning this licensing transaction. In the event of any conflict between your obligations established by these terms and conditions and those established by CCC's Billing and Payment terms and conditions, these terms and conditions shall control.

14. Revocation: Elsevier or Copyright Clearance Center may deny the permissions described in this License at their sole discretion, for any reason or no reason, with a full refund payable to you. Notice of such denial will be made using the contact information provided by you. Failure to receive such notice will not alter or invalidate the denial. In no event will Elsevier or Copyright Clearance Center be responsible or liable for any costs, expenses or damage incurred by you as a result of a denial of your permission request, other than a refund of the amount(s) paid by you to Elsevier and/or Copyright Clearance Center for denied permissions.

LIMITED LICENSE

The following terms and conditions apply only to specific license types:

15. **Translation**: This permission is granted for non-exclusive world **English** rights only unless your license was granted for translation rights. If you licensed translation rights you may only translate this content into the languages you requested. A professional translator must perform all translations and reproduce the content word for word preserving the integrity of the article.

16. **Posting licensed content on any Website**: The following terms and conditions apply as follows: Licensing material from an Elsevier journal: All content posted to the web site must maintain the copyright information line on the bottom of each image; A hyper-text must be included to the Homepage of the journal from which you are licensing at http://www.sciencedirect.com/science/journal/xxxxx or the Elsevier homepage for books at http://www.elsevier.com; Central Storage: This license does not include permission for a scanned version of the material

to be stored in a central repository such as that provided by Heron/XanEdu.
Licensing material from an Elsevier book: A hyper-text link must be included to the Elsevier homepage at http://www.elsevier.com . All content posted to the web site must maintain the copyright information line on the bottom of each image.

Posting licensed content on Electronic reserve: In addition to the above the following clauses are applicable: The web site must be password-protected and made available only to bona fide students registered on a relevant course. This permission is granted for 1 year only. You may obtain a new license for future website posting.
17. **For journal authors:** the following clauses are applicable in addition to the above:
Preprints:
A preprint is an author's own write-up of research results and analysis, it has not been peer-reviewed, nor has it had any other value added to it by a publisher (such as formatting, copyright, technical enhancement etc.).
Authors can share their preprints anywhere at any time. Preprints should not be added to or enhanced in any way in order to appear more like, or to substitute for, the final versions of articles however authors can update their preprints on arXiv or RePEc with their Accepted Author Manuscript (see below).
If accepted for publication, we encourage authors to link from the preprint to their formal publication via its DOI. Millions of researchers have access to the formal publications on ScienceDirect, and so links will help users to find, access, cite and use the best available version.
Please note that Cell Press, The Lancet and some society-owned have different preprint policies. Information on these policies is available on the journal homepage.
Accepted Author Manuscripts: An accepted author manuscript is the manuscript of an article that has been accepted for publication and which typically includes author-incorporated changes suggested during submission, peer review and editor-author communications.
Authors can share their accepted author manuscript:

- immediately
  - via their non-commercial person homepage or blog
  - by updating a preprint in arXiv or RePEc with the accepted manuscript
  - via their research institute or institutional repository for internal institutional uses or as part of an invitation-only research collaboration work-group
  - directly by providing copies to their students or to research collaborators for their personal use
  - for private scholarly sharing as part of an invitation-only work group on commercial sites with which Elsevier has an agreement
- after the embargo period
  - via non-commercial hosting platforms such as their institutional repository
  - via commercial sites with which Elsevier has an agreement

In all cases accepted manuscripts should:

- link to the formal publication via its DOI
- bear a CC-BY-NC-ND license - this is easy to do
- if aggregated with other manuscripts, for example in a repository or other site, be shared in alignment with our hosting policy not be added to or enhanced in any way to appear more like, or to substitute for, the published journal article.

Published journal article (JPA): A published journal article (PJA) is the definitive final record of published research that appears or will appear in the journal and embodies all value-adding publishing activities including peer review co-ordination, copy-editing, formatting, (if relevant) pagination and online enrichment.
Policies for sharing publishing journal articles differ for subscription and gold open access articles:
Subscription Articles: If you are an author, please share a link to your article rather than the full-text. Millions of researchers have access to the formal publications on ScienceDirect, and so links will help your users to find, access, cite, and use the best available version.
Theses and dissertations which contain embedded PJAs as part of the formal submission can be posted publicly by the awarding institution with DOI links back to the formal publications on ScienceDirect.
If you are affiliated with a library that subscribes to ScienceDirect you have additional private sharing rights for others' research accessed under that agreement. This includes use for classroom teaching and internal training at the institution (including use in course packs and courseware programs), and inclusion of the article for grant funding purposes.
Gold Open Access Articles: May be shared according to the author-selected end-user license and should contain a CrossMark logo, the end user license, and a DOI link to the formal publication on ScienceDirect.
Please refer to Elsevier's posting policy for further information.
18. **For book authors** the following clauses are applicable in addition to the above: Authors are permitted to place a brief summary of their work online only. You are not allowed to download and post the published electronic version of your chapter, nor may you scan the printed edition to create an electronic version. **Posting to a repository:** Authors are permitted to post a summary of their chapter only in their institution's repository.
19. **Thesis/Dissertation:** If your license is for use in a thesis/dissertation your thesis may be submitted to your institution in either print or electronic form. Should your thesis be published commercially, please reapply for permission. These requirements include permission for the Library and Archives of Canada to supply single copies, on demand, of the complete thesis and include permission for Proquest/UMI to supply single copies, on demand, of the complete thesis. Should your thesis be published commercially, please reapply for permission. Theses and dissertations which contain embedded PJAs as part of the formal submission can be posted publicly by the awarding institution with DOI links back to the formal publications on ScienceDirect.

Elsevier Open Access Terms and Conditions
You can publish open access with Elsevier in hundreds of open access journals or in nearly 2000 established subscription journals that support

Posting or linking by commercial companies for use by customers of those companies.

20. Other Conditions:

v1.9

APPENDIX C: COPYRIGHT PERMISSION FOR CHAPTER 5

AIP PUBLISHING LLC LICENSE
TERMS AND CONDITIONS

Feb 22, 2017

This Agreement between Qianxi Yang ("You") and AIP Publishing LLC ("AIP Publishing LLC") consists of your license details and the terms and conditions provided by AIP Publishing LLC and Copyright Clearance Center.

License Number	4054261327177
License date	
Licensed Content Publisher	AIP Publishing LLC
Licensed Content Publication	Applied Physics Letters
Licensed Content Title	Artificial muscles made of chiral two-way shape memory polymer fibers
Licensed Content Author	
Licensed Content Date	Oct 31, 2016
Licensed Content Volume	109
Licensed Content Issue	18
Type of Use	Thesis/Dissertation
Requestor type	Author (original article)
Format	Print and electronic
Portion	Excerpt (> 800 words)
Will you be translating?	No
Title of your thesis / dissertation	Thermomechanical Modeling of Polymeric Actuators
Expected completion date	Apr 2017
Estimated size (number of pages)	130
Requestor Location	Qianxi Yang 3261 Patrick F. Taylor Hall BATON ROUGE, LA 70803 United States Attn: Qianxi Yang
Billing Type	Invoice
Billing Address	Qianxi Yang 3261 Patrick F. Taylor Hall BATON ROUGE, LA 70803 United States Attn: Qianxi Yang
Total	0.00 USD
Terms and Conditions	

AIP Publishing LLC -- Terms and Conditions: Permissions Uses

AIP Publishing hereby grants to you the non-exclusive right and license to use and/or distribute the Material according to the use specified in your order, on a one-time basis, for the specified term, with a maximum distribution equal to the number that you have ordered. Any links or other content accompanying the Material are not the subject of this license.

1. You agree to include the following copyright and permission notice with the reproduction of the Material:"Reprinted from [FULL CITATION], with the permission of AIP Publishing." For an article, the credit line and permission notice must be printed on the first page of the article or book chapter. For photographs, covers, or tables, the notice may appear with the Material, in a footnote, or in the reference list.
2. If you have licensed reuse of a figure, photograph, cover, or table, it is your responsibility to ensure that the material is original to AIP Publishing and does not contain the copyright of another entity, and that the copyright notice of the figure, photograph, cover, or table does not indicate that it was reprinted by AIP Publishing, with permission, from another source. Under no circumstances does AIP Publishing purport or intend to grant permission to reuse material to which it does not hold appropriate rights.
   You may not alter or modify the Material in any manner. You may translate the Material into another language only if you have licensed translation rights. You may not use the Material for promotional purposes.
3. The foregoing license shall not take effect unless and until AIP Publishing or its agent, Copyright Clearance Center, receives the Payment in accordance with Copyright Clearance Center Billing and Payment Terms and Conditions, which are incorporated herein by reference.
4. AIP Publishing or Copyright Clearance Center may, within two business days of granting this license, revoke the license for any reason whatsoever, with a full refund payable to you. Should you violate the terms of this license at any time, AIP Publishing, or Copyright Clearance Center may revoke the license with no refund to you. Notice of such revocation will be made using the contact information provided by you. Failure to receive such notice will not nullify the revocation.
5. AIP Publishing makes no representations or warranties with respect to the Material. You agree to indemnify and hold harmless AIP Publishing, and their officers, directors, employees or agents from and against any and all claims arising out of your use of the Material other than as specifically authorized herein.
6. The permission granted herein is personal to you and is not transferable or assignable without the prior written permission of AIP Publishing. This license may not be amended except in a writing signed by the party to be charged.
7. If purchase orders, acknowledgments or check endorsements are issued on any forms containing terms and conditions which are inconsistent with these provisions, such inconsistent terms and conditions shall be of no force and effect. This document, including the CCC Billing and Payment Terms and Conditions, shall be the entire agreement between the parties relating to the subject matter hereof.

This Agreement shall be governed by and construed in accordance with the laws of the State of New York. Both parties hereby submit to the jurisdiction of the courts of New York County for purposes of resolving any disputes that may arise hereunder.

V1.1

Questions? customercare@copyright.com or +1-855-239-3415 (toll free in the US) or +1-978-646-2777.

VITA

Ms. Qianxi Yang was born in Changchun, the capital city of Jilin Province in China. She received a Bachelor of Science in Applied Physics from the University of Science and Technology of China (USTC) in June 2010. Ms. Yang started her doctoral study in the Department of Mechanical and Industrial Engineering at Louisiana State University (LSU) in August 2011. Since then, she has been working under the guidance of Dr. Guoqiang Li for the last six years as a Research Assistant. At the moment of applying final exam, she has five published and one submitted peer reviewed first-author journal papers at LSU. She expects to graduate in the Spring 2017 with the degree of Doctor of Philosophy in mechanical engineering.